

## **Distribution Agreement**

In presenting this thesis or dissertation as a partial fulfillment of the requirements for an advanced degree from Emory University, I hereby grant to Emory University and its agents the non-exclusive license to archive, make accessible, and display my thesis or dissertation in whole or in part in all forms of media, now or hereafter known, including display on the world wide web. I understand that I may select some access restrictions as part of the online submission of this thesis or dissertation. I retain all ownership rights to the copyright of the thesis or dissertation. I also retain the right to use in future works (such as articles or books) all or part of this thesis or dissertation.

Signature:

---

Noah B Jaffe

---

Date

The Big Dissertation On Small Beryllium Clusters

By

Noah B Jaffe  
Doctor of Philosophy

Chemistry

---

Michael Heaven, Ph.D.  
Advisor

---

Katherine Davis, Ph.D.  
Committee Member

---

Francesco Evangelista, Ph.D.  
Committee Member

Accepted:

---

Kimberly Jacob Arriola, Ph.D.  
Dean of the James T. Laney School of Graduate Studies

---

Date

The Big Dissertation On Small Beryllium Clusters

By

Noah B Jaffe  
B.S., Emory University, GA, 2019

Advisor: Michael Heaven, Ph.D.

An abstract of  
A dissertation submitted to the Faculty of the  
James T. Laney School of Graduate Studies of Emory University  
in partial fulfillment of the requirements for the degree of  
Doctor of Philosophy  
in Chemistry  
2024

## Abstract

### The Big Dissertation On Small Beryllium Clusters

By Noah B Jaffe

Beryllium is a deceptively simple atom. Despite its simple  $1s^2 2s^2$  electronic structure, this closed shell atom participates in a number of anomalous bonding schemes. This simple structure also leads to a surprising amount of theoretical challenge, largely due to the near degeneracy of the Be 2p orbitals with respect to the 2s orbital, which makes it a fantastic system to benchmark high level electronic structure methods. Additionally due to the element's toxicity, very little experimental data is available to compare to electronic structure calculations. In the following work, we present a series of novel studies on Beryllium containing molecules via Slow Electron Velocity-Map Imaging (SEVI) spectroscopy. These studies focus on the electronic structure of both pure beryllium clusters, and hyper-metallic beryllium monoxide clusters, neither of which have been studied by anion photoelectron spectroscopy until this point. With the exception of BeOBe, none of the species presented here have been studied by experimental methods outside of mass spectrometer studies. *Ab initio* studies of these anions reveal a wealth of knowledge, but some of these clusters still elude exact understanding even with high level theory to assist us.



The Big Dissertation On Small Beryllium Clusters

By

Noah B Jaffe  
B.S., Emory University, GA, 2019

Advisor: Michael Heaven, Ph.D.

A dissertation submitted to the Faculty of the  
James T. Laney School of Graduate Studies of Emory University  
in partial fulfillment of the requirements for the degree of  
Doctor of Philosophy  
in Chemistry  
2024

## Acknowledgments

To my advisor, Dr Michael Heaven, for accepting me into his lab as an undergraduate and helping foster my growth as a scientist through the years.

To my collaborator Dr John Stanton for being a constant point of contact and assistance with my many computational quandaries, and challenging me to take on one of the hardest puzzles of my life.

To my mentor Dr Mallory Green for her patience and help getting me up to speed in the Heaven lab, and your endless help in the world of professional academia.

To my parents and family for always giving me support through the hard and stressful times, and doing what they can to take things off my plate.

To Danielle for always listening to me and my rants and your endless emotional support.

To my friends around the world for keeping me sane and grounded through the ups and down in life.

To my comrades in Atlanta for helping show me how beautiful this city is and can be, and for striving to make it a better place.

To all of the staff in the Chemistry department who make the building run, and who's daily interactions always leave me with a smile

To the Emory admin for ensuring I have had an endless source of spite to keep me going through this PhD.

# Contents

<b>1</b>	<b>Introduction</b>	<b>1</b>
1.1	Beryllium Chemistry . . . . .	2
1.2	Anion Photoelectron Spectroscopy . . . . .	8
<b>2</b>	<b>Experimental Methods</b>	<b>15</b>
2.1	Instrumentation Overview . . . . .	16
2.2	Generation of Anions . . . . .	19
2.3	Mass : Charge Discrimination . . . . .	22
2.4	Anion Optics . . . . .	25
2.5	Velocity Map Imaging . . . . .	26
2.6	Electron Detection and Imaging . . . . .	29
2.7	Software and Processing . . . . .	30
2.7.1	Acquisition . . . . .	31
2.7.2	Pre-Processing . . . . .	34
2.7.3	Processing . . . . .	35
2.8	Spectrum Calibration . . . . .	37
2.9	Experimental Upgrades . . . . .	38
<b>3</b>	<b>A Quirky Little Guy: The Beryllium Trimer and its Anion</b>	<b>43</b>
3.1	Introduction . . . . .	45
3.2	Experimental Procedure . . . . .	46

3.3	Results and Discussion . . . . .	47
<b>4</b>	<b>Almost an Atom: The Beryllium Tetramer and its Anion</b>	<b>57</b>
4.1	Introduction . . . . .	59
4.2	Experimental Procedure . . . . .	60
4.3	Results and Discussion . . . . .	61
<b>5</b>	<b>The Youth Taker: The Beryllium Pentamer and its Anion</b>	<b>70</b>
5.1	Background and Introduction . . . . .	72
5.2	Experimental Procedure . . . . .	73
5.3	Computational Results . . . . .	74
5.4	Experimental Results . . . . .	89
5.5	Conclusions and Future Areas of Interest . . . . .	98
5.6	Be Pentamer Supplemental Info . . . . .	99
<b>6</b>	<b>All Bets Off: Multireference Problems in Hyper-metallic Beryllium Oxide Clusters</b>	<b>103</b>
6.1	Introduction and Background . . . . .	105
6.2	Computational Studies . . . . .	106
6.3	Experimental Procedure . . . . .	112
6.4	Experimental Results . . . . .	113
6.5	Conclusions and Ongoing work . . . . .	119
<b>7</b>	<b>The Broken, The Beaten, The Damned: Preliminary Works and Unsuccessful Attempts on Other Molecules</b>	<b>121</b>
7.1	Beryllium Oxides . . . . .	123
7.1.1	Be <sub>2</sub> O <sub>2</sub> . . . . .	123
7.1.2	OBeO . . . . .	123
7.2	SBeS . . . . .	124

7.3	Beryllium Nitrides . . . . .	127
7.3.1	BeN . . . . .	127
7.3.2	Be <sub>3</sub> N . . . . .	129
<b>8</b>	<b>When One Door Closes: Conclusions and Future Direction</b>	<b>132</b>
	<b>References</b>	<b>133</b>

# List of Figures

1.1	The potential energy curves of the beryllium dimer at different levels of theory with a consistent basis set[16] . . . . .	6
1.2	A schematic representation of Anion Photoelectron Spectroscopy. A laser with photon energy $h\nu$ excites an electron, detaching it with an eKE determined by the state of the neutral molecule left behind . . .	9
1.3	The basic components of a Velocity-Map Imaging detector. Charged particles light up the detector, and the spatial distribution is recorded.	11
2.1	A schematic layout of the current experimental apparatus . . . . .	16
2.2	A cutaway of the pulse valve (pink hash marks) and ablation block (light blue hash marks). The blue arrow represents gas flow into the block, the dashed red arrow represents the laser pulse into the block, and the gray cloud represents the expansion plume. . . . .	20
2.3	The basic layout of our Wiley-McLaren TOFMS. The plates are held inside a stainless steel tube (translucent grey box) with a small opening to allow ablation products to enter. . . . .	23
2.4	A diagram of the ion optics used in the second chamber. The parallel plate voltages are independently varied, and the Einzel lens is composed of three ring electrodes with a voltage applied to the center electrode. . . . .	25

2.5	A schematic of the VMI optics including the MCP and Phosphor components of the detector. . . . .	27
2.6	A flowchart showing the image acquisition software algorithm. . . . .	32
2.7	A comparison of the raw images (left column) and processed spectra (right column) with signal based discrimination (bottom) and without signal based discrimination (top). The top row shows the inclusion of all shots, while the bottom shows only shots where the photomultiplier tube registered voltages above a baseline value. . . . .	33
2.8	A sample Sulfur anion spectrum in units of Pixel (left), eBE (top right), and eKE (bottom right). . . . .	38
2.9	A CAD model of the original Even-Lavie ablation source. Motors and the source rod are not shown in this image. . . . .	39
2.10	A CAD model of the V2 EL ablation source. The left side shows a perspective view from the top front corner and the right shows a view from side-on. . . . .	40
2.11	A CAD model of the experiment after installation of the ion trap chambers. . . . .	42
3.1	Photoelectron survey spectrum of the $\text{Be}_3^-$ anion taken with detachment photon energy of $18797\text{cm}^{-1}$ (vertical polarization shown by blue double sided arrow). The strongest electronic transitions have been labeled with guidance from high-level electronic structure calculations. Inset photo shows the velocity map image produced by MEVELER software . . . . .	48
3.2	Photoelectron spectrum of $\text{Be}_3^-$ taken with a detachment photon energy of $11236\text{cm}^{-1}$ (vertical polarization shown by double sided blue arrow). Inset photo shows the velocity map image produced by MEVELER software. . . . .	49

3.3	Photoelectron spectrum of $\text{Be}_3^-$ taken with a detachment photon energy of $13605 \text{ cm}^{-1}$ (vertical polarization shown by double sided blue arrow). Inset photo shows the velocity map image produced by MEVELER software. . . . .	51
3.4	A Franck-Condon simulation for the $\text{Be}_3$ EA transition at 100K. X axis is given in $\text{cm}^{-1}$ with the 0-0 transition at zero, and intensity is normalized to 1. . . . .	53
3.5	Potential energy curves for the $\text{Be}_3$ anion and neutral molecule between $1.95\text{\AA}$ and $2.44\text{\AA}$ , computed in $0.01\text{\AA}$ steps along the symmetric stretch. The neutral ground state was computed using CCSDT and the anion states were computed using EOMEA-CCSDT. All computations were performed in CFOUR using an aug-cc-pCVTZ basis set. . . . .	54
3.6	Photoelectron spectrum of $\text{Be}_3^-$ taken with a detachment photon energy of $28169 \text{ cm}^{-1}$ (vertical polarization shown by double sided blue arrow). Inset photo shows the velocity map image produced by MEVELER software. . . . .	56
4.1	Photoelectron spectrum of $\text{Be}_4^-$ taken with a detachment photon energy of $18182\text{cm}^{-1}$ (550nm). Inset photo shows the velocity map image produced by MEVELER software, and laser polarization is given by the double headed arrow . . . . .	62
4.2	Photoelectron spectrum of $\text{Be}_4^-$ taken with a detachment photon energy of $14184\text{cm}^{-1}$ (705nm). Inset photo shows the velocity map image produced by MEVELER software, and laser polarization is given by the double headed arrow . . . . .	63



4.3	ELF contour maps along the plane of the $\text{Be}_4 \ ^1A_1$ molecule through the center of the tetrahedron bisecting it into two Be dimers (top left), the plane through two Be atom bisecting the tetrahedron (top right), and the plane through three Be atoms forming a face of the tetrahedron (bottom). (3,-3) non-nuclear attractor (NNA) and nuclear critical points are shown as brown dots, (3,-1) bond critical points (BCP) critical points in blue, (3,1) ring critical points (RCPs) in white, and (3,3) cage critical points (CCPs) in green. Image and analysis performed using Multiwfn [69, 70] . . . . .	67
4.4	ELF contour maps along the plane of the $\text{Be}_4 \ ^2A_1$ anion through the center of the tetrahedron bisecting it into two Be dimers (top left), the plane through two Be atom bisecting the tetrahedron (top right), and the plane through three Be atoms forming a face of the tetrahedron (bottom). (3,-3) non-nuclear attractor (NNA) and nuclear critical points are shown as brown dots, (3,-1) bond critical points (BCP) critical points in blue, and (3,1) ring critical points (RCPs) in white. (3,3) cage critical points (CCPs) are notably absent. Image and analysis performed using Multiwfn [69, 70] . . . . .	68
4.5	Photoelectron spectrum of $\text{Be}_4^-$ taken with a detachment photon energy of $25189 \text{ cm}^{-1}$ (397nm). The sharp cutoff just above $13500 \text{ cm}^{-1}$ is due to the edge of the detector, and the large peak is due to the electron affinity transition being partially captured. . . . .	69
5.1	ELF contour maps along the plane of the $\text{Be}_5 \ ^1A'_1$ equatorial ring (top left), two axial Be and one equatorial Be (top right), and two axial Be parallel to two equatorial Be (bottom). (3,-3) NNA and NCP critical points are shown as brown dots, while (3,-1) BCP critical points are shown in blue. Image and analysis performed using Multiwfn [69, 70]	79

5.2	Interpolated EOMEA-CCSD/cc-pCVDZ potential energy surfaces across the T90 (deg) and R1 (Å) coordinates. All other coordinates were optimized at each point in the grid. Color-mapping and Z axis shows the energy in $\text{cm}^{-1}$ . The $A_1$ state minimum is on the right side. . . . .	83
5.3	Interpolated EOMEA-CCSD/cc-pCVDZ potential energy surfaces across the T120 (deg) and R1 (Å) coordinates. All other coordinates were optimized at each point in the grid. Color-mapping and Z axis shows the energy in $\text{cm}^{-1}$ . The $A_1$ state minimum is on the right side. . . . .	84
5.4	Interpolated EOMEA-CCSD/cc-pCVDZ potential energy surfaces across the T120 (deg) and T90 (deg) coordinates. All other coordinates were optimized at each point in the grid. Color-mapping and Z axis shows the energy in $\text{cm}^{-1}$ . The $A_1$ state minimum is on the right side. . . . .	85
5.5	ELF contour maps along the plane of the $\text{Be}_5^- \ ^2A_2$ equatorial ring (top left), two axial Be and one equatorial Be (top right), and two axial Be parallel to two equatorial Be (bottom). (3,-3) NNA and NCP critical points are shown as brown dots, while (3,-1) BCP critical points are shown in blue. Image and analysis performed using Multiwfn [69, 70]	86
5.6	ELF contour maps along the plane of the $\text{Be}_5 \ ^3A_2$ equatorial ring (top left), two axial Be and one equatorial Be (top right), and two axial Be parallel to two equatorial Be (bottom left), and the plane of the 1 3 and 4 Be atoms from 5.2. (3,-3) NNA and NCP critical points are shown as brown dots, (3,-1) BCP critical points are shown in blue, and (3,1) RCPs are shown in white. Image and analysis performed using Multiwfn [69, 70] . . . . .	87

5.7	AIM analysis[71] of the $\text{Be}_5$ $1^3\text{A}_2$ state. NNAs are shown as purple dots, BCPs as orange, and RCPs as yellow. Bonding paths have been drawn between (3,-3) and (3,-1) critical points. Image and analysis performed using Multiwfn [69, 70] . . . . .	89
5.8	Photoelectron spectrum of $\text{Be}_5^-$ taken with a detachment photon energy of $18797\text{cm}^{-1}$ (532nm). Inset photo shows the velocity map image produced by MEVELER software, and laser polarization is given by the double headed arrow . . . . .	90
5.9	Photoelectron spectrum of $\text{Be}_5^-$ taken with a detachment photon energy of $15576\text{cm}^{-1}$ (642nm). Inset photo shows the velocity map image produced by MEVELER software, and laser polarization is given by the double headed arrow. Perpendicular and parallel transitions are marked by the green and red manifolds respectively. . . . .	93
5.10	Photoelectron spectrum of $\text{Be}_5^-$ taken with a detachment photon energy of $18797\text{cm}^{-1}$ (532nm). Inset photo shows the velocity map image produced by MEVELER software, and laser polarization is given by the double headed arrow. Perpendicular and parallel transitions are marked by the green and red manifolds respectively. . . . .	95
5.11	Photoelectron spectrum of $\text{Be}_5^-$ taken with a detachment photon energy of $9398.5\text{ cm}^{-1}$ (1064nm). Due to low signal the anisotropy of the associated Velocity Map is over-fit and has non-physical anisotropies. As such it has been omitted . . . . .	97
5.12	Raw EOMEA-CCSD/cc-pCVDZ potential energy surfaces across the T90 (deg) and R1 ( $\text{\AA}$ ) coordinates. All other coordinates were optimized at each point in the grid. Color-mapping and Z axis shows the energy in $\text{cm}^{-1}$ . The $\text{A}_1$ state minimum is on the right side. . . . .	100

5.13	raw EOMEA-CCSD/cc-pCVDZ potential energy surfaces across the T120 (deg) and R1 (Å) coordinates. All other coordinates were optimized at each point in the grid. Color-mapping and Z axis shows the energy in $\text{cm}^{-1}$ . The $A_1$ state minimum is on the right side. . . . .	101
5.14	raw EOMEA-CCSD/cc-pCVDZ potential energy surfaces across the T120 (deg) and T90 (deg) coordinates. All other coordinates were optimized at each point in the grid. Color-mapping and Z axis shows the energy in $\text{cm}^{-1}$ . The $A_1$ state minimum is on the right side. . . .	102
6.1	$ 3\sigma_g^2 1\pi_u^4 3\sigma_u^2\rangle$ (top) and $ 3\sigma_g^2 1\pi_u^4 4\sigma_g^2\rangle$ (bottom) orbitals. Image produced using wxMacMolPlt[97]. . . . .	108
6.2	The HOMO (bottom) and LUMO (top) orbitals of BeBeOBe. Image produced using wxMacMolPlt[97]. . . . .	109
6.3	The HOMO (top) and LUMO (bottom) orbitals of BeBeOBeBe. Image produced using wxMacMolPlt[97]. . . . .	110
6.4	Chair type $\text{Be}_5\text{O}$ geometry (left) and $\text{Be}_5\text{O}$ ring geometry (right) plotted with their respective HOMO(top) and LUMO (bottom) orbitals. Image produced using wxMacMolPlt[97]. . . . .	111
6.5	$18797 \text{ cm}^{-1}$ photodetachment spectrum of BeOBe showing a singular wide feature at approximately $9750 \text{ cm}^{-1}$ . . . . .	113
6.6	$11380 \text{ cm}^{-1}$ photodetachment spectrum of BeOBe showing several features as well as the singlet triplet split. Bands to the left of the $\tilde{X}^1\Sigma_g^+$ peak are attributed to hot bands of the $\nu_2$ bending mode in the anion. Inset image shows the velocity map image produced by MEVELER [45], and laser polarization is shown by the double headed arrow. . . .	114
6.7	$18797 \text{ cm}^{-1}$ photodetachment spectrum of $\text{Be}_3\text{O}$ . Inset image shows the velocity map image produced by MEVELER [45], and laser polarization is shown by the double headed arrow. . . . .	116

6.8	18797 $\text{cm}^{-1}$ photodetachment spectrum of $\text{Be}_4\text{O}$ . Inset image shows the velocity map image produced by MEVELER [45], and laser polarization is shown by the double headed arrow. . . . .	117
6.9	18797 $\text{cm}^{-1}$ photodetachment spectrum of $\text{Be}_5\text{O}$ . Inset image shows the velocity map image produced by MEVELER [45], and laser polarization is shown by the double headed arrow. . . . .	118
6.10	18797 $\text{cm}^{-1}$ photodetachment spectrum of $\text{Be}_6\text{O}$ . Inset image shows the velocity map image produced by MEVELER [45], and laser polarization is shown by the double headed arrow. . . . .	119
6.11	18797 $\text{cm}^{-1}$ photodetachment spectrum of $\text{Be}_7\text{O}$ . Inset image shows the velocity map image produced by MEVELER [45], and laser polarization is shown by the double headed arrow. . . . .	120
6.12	18797 $\text{cm}^{-1}$ photodetachment spectrum of $\text{Be}_8\text{O}$ . . . . .	120
7.1	A survey spectrum of $\text{Be}_2\text{O}_2$ using 18797 $\text{cm}^{-1}$ detachment photons. .	123
7.2	A survey spectrum of $\text{BeO}_2$ using 28169 $\text{cm}^{-1}$ detachment photons. .	124
7.3	A photoelectron spectrum of $\text{BeS}_2$ using 27322 $\text{cm}^{-1}$ detachment photons.	126
7.4	Potential energy cuts across the $\text{SBeS}$ singlet and triplet ground states along the bending coordinate at three levels of theory with constant bond length. Discontinuities are believed to be due to the switching of state symmetries between the ground state bent and linear conformations	130
7.5	Potential energy cuts across the $\text{SBeS}^-$ doublet ground state along the bending coordinate at three levels of theory with constant bond length. Discontinuities are believed to be due to the switching of state symmetries between the ground state bent and linear conformations .	131

# List of Tables

2.1	Average Relative Timings during a VMI recording . . . . .	18
3.1	Be <sub>3</sub> Transition Energies . . . . .	50
3.2	Bond Lengths of Be <sub>3</sub> and Be <sub>3</sub> <sup>-</sup> . . . . .	50
3.3	Be <sub>3</sub> and Be <sub>3</sub> <sup>-</sup> Harmonic Vibrations . . . . .	50
4.1	Be <sub>4</sub> and Be <sub>4</sub> <sup>-</sup> Equilibrium Bond Lengths . . . . .	65
4.2	Be <sub>4</sub> and Be <sub>4</sub> <sup>-</sup> Harmonic Frequencies . . . . .	66
5.1	Be <sub>5</sub> Computational Geometry Predictions . . . . .	75
5.2	Be <sub>5</sub> Z-Matrix . . . . .	75
5.3	Be <sub>5</sub> <sup>-</sup> X <sup>2</sup> A <sub>2</sub> Geometry Parameters . . . . .	76
5.4	Be <sub>5</sub> Ground State Wavefunction Energies . . . . .	77
5.5	Be <sub>5</sub> <sup>-</sup> Relative Energies . . . . .	80
5.6	Be <sub>5</sub> <sup>-</sup> Jahn-Teller Stabilization Energies . . . . .	81
5.7	Be <sub>5</sub> and Be <sub>5</sub> <sup>-</sup> Ground State Harmonic Frequencies . . . . .	82
5.8	Be <sub>5</sub> A <sub>2</sub> Triplet Geometries and Energies . . . . .	88
5.9	Figure 5.9 Peaks and Intensities . . . . .	99
5.10	Figure 5.10 Peaks and Intensities . . . . .	100
7.1	SBeS CCSD(T)/aug-cc-pVTZ Computation Results . . . . .	127

# Chapter 1

## Introduction

## 1.1 Beryllium Chemistry

Understanding the chemistry and electronic structure of beryllium has been a long outstanding endeavor in the scientific community. Initial studies on beryllium molecules were focused on the bonding nature of  $\text{Be}_2$ , which remained an unresolved question in the literature until relatively recently when it was found to be bound by approximately  $929.7\text{cm}^{-1}$  despite its formal bond order of zero [1–3]. Modern studies have been largely focused on the non-monotonic changes of the electronic structure of these  $\text{Be}_n$  clusters with increasing size. Specifically of interest to the scientific community are pure beryllium clusters, beryllium oxide clusters, and beryllium nanoalloys [4–12].

$\text{Be}_n$  ( $n=1,2,3,\dots$ ) clusters have properties that make them ideal candidates for the study of metallic onset in clusters. Due to beryllium’s electron count of four, relativistic and spin orbit effects in the Hamiltonian are safely ignored, and these systems are dominated by electron correlation effects. Unfortunately these correlation effects prove to be particularly intense and finicky in beryllium, lending even more importance to experimental studies of these systems. While quantitative consensus on the bonding energies of these clusters has not yet been reached, it is generally agreed that these clusters’ stability approaches the bulk stability in a very non-monotonic nature [6, 8, 9, 12, 13].

The transition from molecular to bulk metallic character, often defined as the point at which the HOMO-LUMO gap approaches  $kT$ , has remained an open question. Fortunately, within Koopman’s approximation, we can measure the HOMO-LUMO gap using anion photoelectron spectroscopy. In these experiments the HOMO-LUMO gap is approximated as the difference between the anion ground state to neutral ground state transition energy and the anion ground state to neutral first electronic excited state transition energy. In addition, the experimental electron affinity (given as the difference between the anion’s ground state energy and the neutral’s ground state



energy) acts as a valuable metric to compare against high level theory predictions.

Many of the strange bonding effects in beryllium molecules are due to the small 2s-2p energy gap in atomic beryllium. Due to this small gap, beryllium often hybridizes these orbitals. In combination with its high ionization energy and short atomic radius, beryllium participates in nominally covalent bonding much more easily than other group IIA metals. For example,  $\text{MgC}_2$  is considered to have an ionic bond represented as  $\text{Mg}^+\text{C}_2^-$ , while  $\text{BeC}_2$  described more accurately as a polar covalent bond between a Be atom and a  $\text{C}_2$  moiety [14, 15].

Although near degeneracy in atomic Be 2s-2p orbitals lends itself to interesting and anomalous bonding mechanics, it also results in a surprising amount of difficulty for electronic structure computation. While one would naively expect that the small electron count of four would lend itself to accurate computation, in reality most Be containing molecules suffer from electron correlation effects that can be difficult to accurately account for. Electron correlation generally falls into two somewhat subjectively defined categories, static and dynamic.

In static correlation, multiple electronic states mix with each other due to near degenerate energies, resulting in a wavefunction that cannot be accurately described by a single determinant. These single determinant wavefunctions are also often called ‘single reference’ wavefunctions. In cases where a single reference wavefunction is insufficient, the wavefunction must be treated as a multireference wavefunction, which is made up of a combination of multiple single reference wavefunctions where each single reference wavefunction makes up some part of the total wavefunction. While all true wavefunctions will be somewhat multireference in reality, many molecules have electronic states whose wavefunctions are strongly dominated by one single reference wavefunction, and can be treated as single reference problems. When multiple wavefunctions make up a substantial part of the total wavefunction, this assumption falls apart, and we must use a multireference method to obtain results that have any

chance at accuracy.

In dynamic correlation, the overall energy of the wavefunction is heavily dependent on electron-electron interactions, and the wavefunction becomes very sensitive to the position of electrons with respect to each other. In purely dynamically correlated systems the underlying wavefunction is reasonably well defined by a single determinant, but the positions and energies of electrons cannot be adequately recovered by simple self consistent field theory. In these cases the single reference wavefunction is acted on by some form of operator, which adds corrections to the Hartree-Fock wavefunction and results in a more accurate description of the true wavefunction.

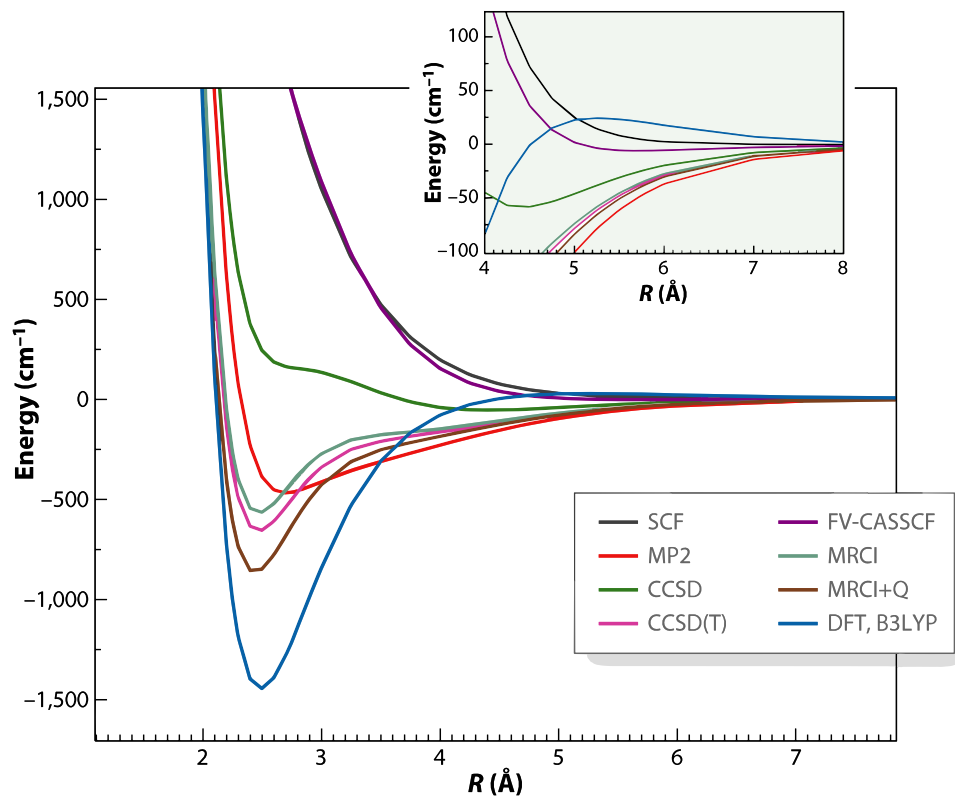
While these two categories of correlation are often described differently, the line between them is not rigorously defined, and many methods that treat one of them will also treat the other at some level. Generally, the choice of theoretical method for a given system is somewhat guided by which type of correlation the system experiences. In cases where the correlation is expected to be predominantly static, a multireference method like complete active space self consistent field (CASSCF) with corrections like multireference configuration interaction (MRCI) tend to perform better. In cases where the correlation is dominated by dynamic correlation coupled cluster (CC) methods that operate on a single reference wavefunction often produce an accurate picture. Both single and multireference methods require additional corrections to a Hartree-Fock type wavefunction that increases computational cost, and the more corrections to the wavefunction that are made the more intense this cost becomes; eventually the cost of a given computation becomes too high, either due to memory or time constraints, and becomes unfeasible to realistically perform.

Beryllium is interesting, and tricky, because neither dynamic or static correlation can be neglected in many cases. This necessitates the use of very high level theory for physically accurate predictions of Beryllium molecules, and in some cases results in wildly varying predictions depending on a given method's treatment of correlation

effects. While in a normal case a higher level of theory results in a better and more accurate answer, with beryllium this is not always the case. The prototypical example of this is the beryllium dimer,  $\text{Be}_2$ , which puzzled theoreticians for decades until it was experimentally studied in 2009 [1, 16]. The problems with these computations are quickly seen when looking at the dimer ground state potential energy curve, as seen in Figure 1.1. While one would normally expect a high level full valence CASSCF (FV-CASSCF) computation would give a reasonable result, for the dimer it incorrectly predicts a fully repulsive potential. Additionally, while Møller-Plesset 2nd Order Perturbation (MP2) is strictly worse than CC Singles Doubles (CCSD) in terms of the corrections to the SCF wave function (CCSD includes the MP2 correction and additional terms) MP2 performs better when predicting the dimer. In reality the best result of Figure 1.1 is the Multi Reference Configuration Interaction with Davidson correction (MRCI+Q), which comes closest to the experimental dissociation energy of  $D_e = 929.7 \pm 2.0\text{cm}^{-1}$  [1, 16].

It is additionally worth noting the performance of density functional theory (DFT) methods in the dimer, specifically B3LYP. In this case, the dissociation energy is massively overestimated at approximately  $1500\text{cm}^{-1}$ . This is not overly surprising, as density functional methods are non-variational, and can converge to energies lower than the true system minimum, unlike *ab initio* methods that are guaranteed to converge to the true energy strictly from above. Although B3LYP was quantitatively unsuccessful for the dimer, it and other DFT methods have been used to examine higher order clusters as well [8, 9, 11, 17]. In some cases, these values align with *ab initio* values, but due to the lack of direct experimental data to compare with, the effectiveness and accuracy of these computations remains dubious for these molecules. Even given this, because of the low cost of DFT methods compared to *ab initio* methods, there is much interest in using DFT methods to predict these clusters.

In order to effectively quantify how well these methods are performing on these




 Heaven MC, et al. 2011.  
 Annu. Rev. Phys. Chem. 62:375–93

Figure 1.1: The potential energy curves of the beryllium dimer at different levels of theory with a consistent basis set[16]

beryllium clusters, it is of paramount importance to have experimental data to compare to. Unfortunately, beryllium is a highly toxic metal, and there is a lack of experimental data currently in the literature. A majority of the existing studies on beryllium molecules consist of mass spectroscopic and matrix isolated studies. While there is some value that can be gained from these types of studies, very little information on the electronic and geometric structure of a molecule is recovered from matrix isolation and mass spectrometry. In addition to those studies, several gas phase electronic spectroscopy studies have been performed by our lab previously. Generally, electronic spectroscopy techniques provide large amounts of data that can be compared to theory. Vibrations and rotations map the shape of a potential energy

well and geometry of a molecule, and electronic transitions show the spacing between individual wells. Studying molecules in the gas phase removes external solvent effects present in liquid phase and matrix studies, and provides data that is directly comparable to computational theory predictions.

A small number of gas phase electronic spectroscopy studies of Beryllium have been performed previously, using a variety of methods. Stimulated emission pumping (SEP) on the beryllium dimer gave information that yielded its dissociation energy after many years of theoretical quandary[1], and laser induced fluorescence (LIF) studies on BeOBe confirmed a  $^1\Sigma^+$  ground state that theory had struggled with [18]. In addition to the neutral studies Be<sub>2</sub> and BeOBe have been studied via resonance enhanced multi-photon ionization (REMPI) [19] and pulsed-field ionization zero kinetic energy (PFI-ZEKE) [20] spectroscopy respectively, yielding information on the cationic ground states of these molecules. In addition to the cation studies, anion studies have been performed on a small selection of beryllium molecules. These studies were performed using Slow Electron Velocity-Map Imaging (SEVI) spectroscopy, and gave information on the electron affinity (EA) of the molecules, as well as vibrational information and symmetry information for the states involved in each transition. Previously these studies consisted of only diatomic anions; namely BeO<sup>-</sup>, BeS<sup>-</sup>, and BeF<sup>-</sup> [21–23].

Anion photoelectron spectroscopy (APES) provides a few key advantages over traditional neutral based approaches. Beginning with a charged species allows for the mass selection of a given molecule, which removes all other species from our result provided they have a different mass:charge ratio. Additionally, starting with an anion and detaching an electron allows the recovery of the neutral molecule characteristics provided the kinetic energy of the electron is recorded after photo-detachment. Additionally most atoms and molecules with stable anions have EAs that are lower in energy than visible and near UV photons, which means we can detach the excess

electron in a single photon process that is reasonably efficient rather than a multi-photon process. Finally, because the selection rules for photo-detachment are spin based rather than angular momentum based, the states and transitions we see are different than for laser absorption and radiative methods.

## 1.2 Anion Photoelectron Spectroscopy

Anion photoelectron spectroscopy (APES) techniques, like the SEVI spectroscopy used in our lab, exploit a different set of transition rules than the laser emission and absorption techniques common for use with neutral molecules. In APES, given that the energy of a photon exceeds the electron binding energy (eBE) of an electron in a given anionic state, the electron will be photodetached from the anion leaving behind a neutral molecule.



Because energy must be conserved in the system, given a photon of known energy  $h\nu$ , an electron initially bound to the neutral molecule by eBE, and the electron leaving after photodetachment with kinetic energy (eKE) we have

$$\begin{aligned} A - eBE + h\nu &= eKE + A \\ eBE &= h\nu - eKE \end{aligned} \quad (1.2)$$

where  $A - eBE$  describes the anion in terms of the neutral molecule  $A$  and electron bound by eBE, and  $eKE + A$  describes the neutral molecule and electron that leaves with kinetic energy eKE. This means that by measuring the eKE and the photon energy, we can determine the binding energy of the electron, which map the transitions  $A^- \rightarrow A$ . Additionally, because an electron is ejected from the anion, the transition selection rules for an anion to neutral transition are governed by spin changes. Specifically, the neutral molecule state after photodetachment must follow  $\Delta S = \pm 1/2$  with

respect to the anion state before photodetachment.

The transition from the anion ground state to the neutral ground state is named the electron affinity (EA). States originating in anion excited states are often termed hot bands, and we can also access neutral excited states. Additionally, this may result in rotational and vibrational transitions as well, which can be seen provided the resolution of the experiment allows. This process is shown schematically in Figure 1.2.

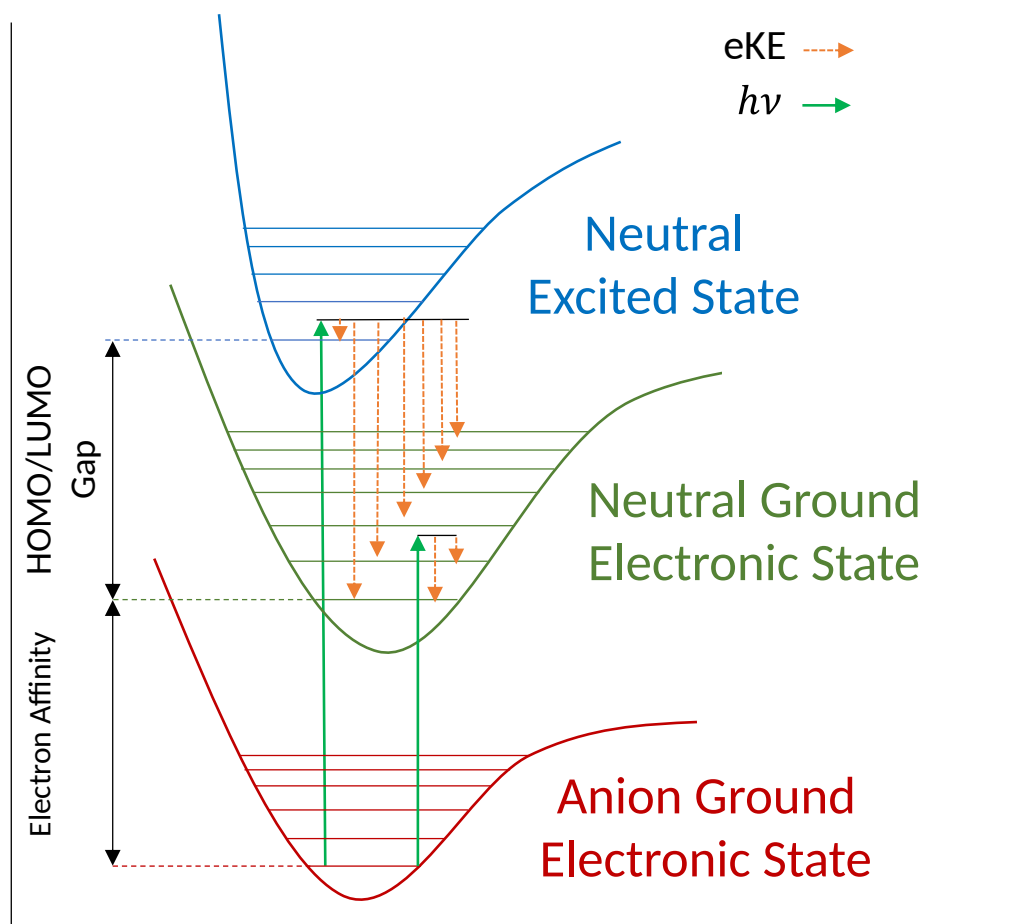


Figure 1.2: A schematic representation of Anion Photoelectron Spectroscopy. A laser with photon energy  $h\nu$  excites an electron, detaching it with an eKE determined by the state of the neutral molecule left behind

The ability to perform APES is only fundamentally restricted by the stability of an anion. Specifically, a neutral molecule must have a positive electron affinity, and we must be able to produce a photon (or multi-photon process) with more energy

than the EA of the molecule of study. Fortunately, most molecules that meet the first requirement also have EA's in the visible range, which is accessible by modern conventional lasers. While these are the only hard requirements, photodetachment processes generally have much smaller cross-sections than absorption processes, meaning that APES techniques need comparably more photon flux for the same number of detachment events to occur. This restriction due to laser power is largely overcome by using pulsed laser based techniques in modern experiments, which have substantially high photon counts during a pulse, rather than continuous wave (cw) schemes.

The first APES experiments used hemisphere electron monochromators and cw argon lasers for detachment [24, 25]. While these experiments were effective, the electron monochromators used suffered from poor collection efficiency and the cw lasers of the time were limited to very few choices of wavelength. This greatly limited the systems that could be studied. As pulsed lasing schemes came into vogue, the number of APES methods increased, and people began turning to time of flight (TOF) based methods. In field free TOF methods, the electron kinetic energy is determined by measuring the electron counts with respect to time after the electrons are flown down a field free drift region. This method has been known to produce spectra with a resolution of approximately 5meV but can have difficulty capturing large amounts of electrons because the method doesn't guide electrons toward the detector [26]. Magnetic bottle TOF (MB-TOF) anion photoelectron spectroscopy takes a hit in resolution in order to maximize the collection efficiency of electrons. Depending on the exact eKE, magnetic bottles can have resolution of anywhere from 10meV to 100meV, but have collection efficiency of 50% or more [27].

On the opposite end of the spectrum from MB-TOF methods that sacrifice resolution for faster acquisition is anion zero electron kinetic energy (aZEKE), which has incredibly high resolution on the order of  $3\text{cm}^{-1}$  in exchange for very long acquisition times[28]. In aZEKE, a tunable pulsed laser is scanned over a the spectral range of



interest, searching for transitions. Electrons of different kinetic energy are separated by electrode plates that are pulsed with a voltage, such that only slow electrons are recorded, yielding the highest resolution possible within this scheme. Unfortunately, these low electron kinetic energy detachments also tend to be the lowest efficiency, as the photodetachment cross section  $\sigma$  is governed by the Wigner threshold law

$$\sigma \propto (eKE)^{l+1/2} \quad (1.3)$$

where  $l$  is the photoelectron's angular momentum. As can be seen for low  $eKE$ , this value trends to zero rapidly for non s-wave photoelectrons where  $l = 0$ . This limits the observable transitions to those with s-wave photodetachment for this method. Additionally, the laser scanning can take considerable time to produce a spectrum over larger ranges, which is a major drawback compared to the TOF methods described earlier.

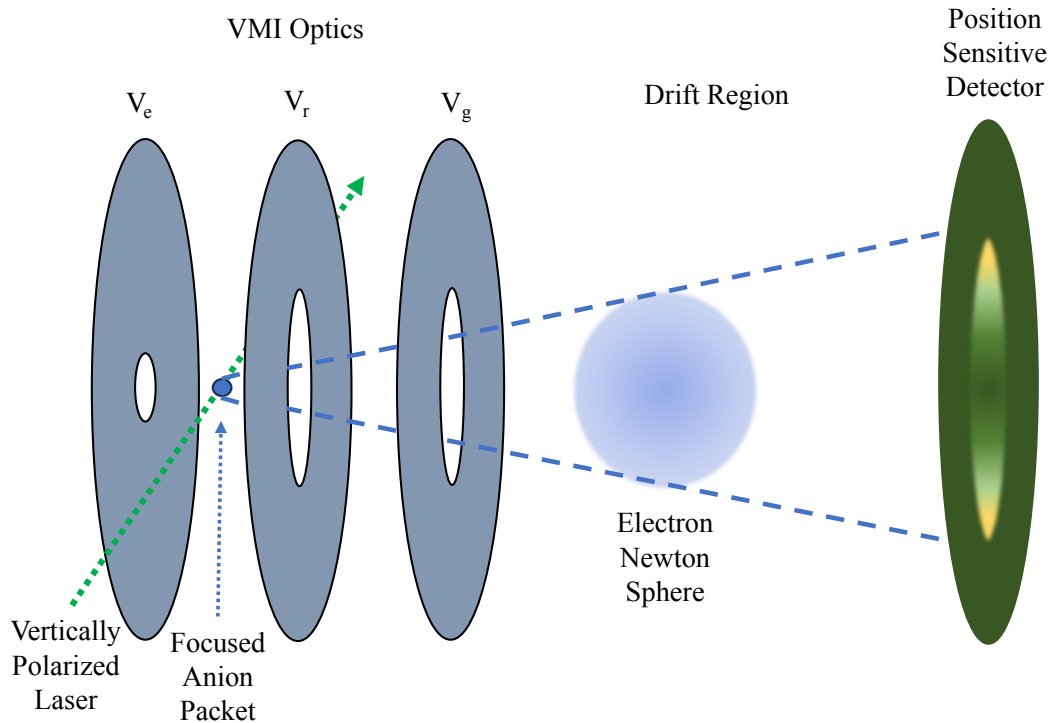


Figure 1.3: The basic components of a Velocity-Map Imaging detector. Charged particles light up the detector, and the spatial distribution is recorded.

To overcome the limitations of previous techniques, a new method was introduced. The new method, known as Velocity Map Imaging (VMI) spectroscopy, was designed by Eppink and Parker and solved the acquisition issues associated with field free TOF and MB-TOF methods [29]. The new method used three electrostatic lenses and a position sensitive detector to record electron images, as shown in Figure 1.3. When imaging electrons, the first two plates have a negative voltage applied to them, and the final plate is grounded. Mass selected anions are hit by a pulsed photodetachment laser between the first and second plates, creating photoelectrons. The imaging lenses cause the photoelectrons to remain a spatially resolved series of nested newton spheres, where each of the spheres has a radius defined by the eKE of electrons from a given transition and cylindrical symmetry about the laser polarization axis. The photoelectrons are then pushed toward a spatially resolved detector, where the spatial distribution of the electrons is recorded. These electron images appear as nested rings or crescents, where the radius of the ring is related to the electron kinetic energy by

$$\begin{aligned}
 R_i &= \alpha v_i t \\
 eKE &= \frac{m_e v_i^2}{2} \\
 eKE &= \frac{m_e (R_i / \alpha t)^2}{2}
 \end{aligned}
 \tag{1.4}$$

with  $\alpha$  being a magnification constant determined by the imaging voltages,  $R_i$  being the radius' of different electron rings in an image, and  $t$  being the flight time from photodetachment to impact on the detector. Because the electrons are accelerated by reasonably high voltages,  $t$  is treated as a constant for all electrons. The product of the electron mass  $m_e$ , the magnification parameter  $\alpha$ , and time  $t$  is generally determined experimentally by studying a known system, and fit using calibrations as discussed in Section 2.8. Because the eKE maps as  $R_i^2$ , and the detector has discrete pixels, larger radii map to more values in eKE space, and the best resolution is obtained for small

$R_i^2$ . Additionally, because the spatial distributions are recorded rather than TOF distributions, we can gain information about the photoelectron angular distribution (PAD) with respect to the laser polarization axis. The PAD for photodetachment events corresponding to a single photon transition can be approximated as

$$I(\theta, eKE) = \frac{\sigma(eKE)}{4\pi}(1 + \beta(eKE)P_2(\cos(\theta))) \quad (1.5)$$

where  $I(\theta)$  is the signal intensity,  $\sigma(eKE)$  is the eKE dependant photodetachment cross section,  $-1 \leq \beta(eKE) \leq 2$  is known as the anisotropy parameter, and  $P_2(\cos(\theta))$  is a second order Legendre polynomial. Here the angle  $\theta$  is measured with respect to the laser polarization vector. Strictly speaking changing the eKE will also impact the  $\beta$  parameter and cross section  $\sigma$ , but these changes are small across small eKE shifts above the detachment threshold for a given transition and are normally neglected in this simplified view.

Values of  $\beta$  above zero are known as parallel transitions and values below zero are referred to as perpendicular, based on if the signal is most intense parallel or perpendicular to the laser polarization direction. Additionally, a  $\beta$  value of 0 is known as an isotropic transition due to the uniform intensity at all values of  $\theta$ . Because the symmetry of the electron wave leaving the anion is determined by the molecular orbital from which it originates and the final symmetry of the molecule, the value of  $\beta$  can give insight into the symmetry of the anion and neutral states involved in a transition [30–32]. Specifically in a one electron detachment without negligible relaxation of the resultant molecule, the photoelectron must undergo an angular momentum change of  $\Delta l = \pm 1$ , due to the absorption of a photon which has an angular momentum of 1. These interfering photoelectron waves then give rise to the PAD. Note that for a molecular orbital  $l$  is often a poor quantum number, which results in PADs with  $\beta$  values other than -1, 2, and 0. This model is rather simplified

and gives a qualitative insight into the PAD and its use in small molecules; for a more rigorous treatment the reader is referred elsewhere [30, 32].

Similar to other methods in PES the resolution of VMI based methods is dependent on the electron’s kinetic energy, however the resolution of this method is ultimately limited by the detector pore size in combination with the pixel size of the recording device. This means that electrons with slightly different eKE’s will be bunched into the same pore of the multichannel plate detector, and ‘binned’ into the same pixel in the camera sensor. This gives rise to the fundamental resolution limit of the VMI method. Originally, this method used a high extractor voltage, which gave excellent range but only decent resolution, as higher extractor voltages will result in larger bins in eKE space. To help assuage this problem, slow electron velocity-map imaging (SEVI) was introduced by the Neumark group [33]. The SEVI method relies on the same physics as VMI, but uses lower extraction voltages and a longer drift region to allow the Newton spheres to expand more. This shrinks the bins in eKE space relative to regular VMI studies, effectively zooming in on the center of a regular VMI image, and allows a higher resolution at the cost of range. This new SEVI method produces spectra with slightly worse resolution than aZEKE, but acquires them orders of magnitude faster. Additionally, by increasing the extractor voltages, a SEVI spectrometer can be used to provide comparable range and resolution to regular VMI equipment. Depending on the exact experimental conditions, SEVI is capable of resolution down to only a few  $\text{cm}^{-1}$ , and as such it is our method of choice.

## Chapter 2

# Experimental Methods

## 2.1 Instrumentation Overview

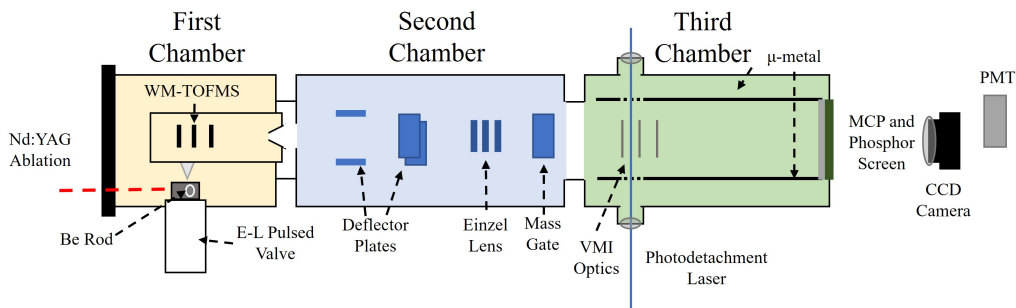


Figure 2.1: A schematic layout of the current experimental apparatus

The current experimental design of the apparatus is schematically shown in Figure 2.1, which has been slightly changed from the previously described apparatus[34, 35]. The specific design philosophy behind these upgraded parts, as well as upgrades that have been designed for future implementation, are described in more detail in Section 2.9.

Molecules are generated in the first chamber via Nd:YAG pulsed laser ablation of a metallic rod of interest, in general beryllium, while exposed to a short gas pulse generated by an Even-Lavie type valve [36]. Laser ablation, as well as optimization of source conditions are further discussed in Section 2.2. The choice of gas is dependent on the molecule of interest, but in general it is a gas mix of a small concentration (0.1% to 5%) of reactant gas(es) in a rare gas carrier. In our apparatus argon, helium, and neon have all been attempted as carriers, and argon has been found to give the strongest signal and coldest spectra in most cases. The Even-Lavie valves require a substantially higher backing pressure than the common Parker type valves often used in these experiments, and we have found that a backing pressure of approximately 1000psi yields good signal and cooling in our expansions. The expansion is directed toward a pulsed Wiley-McLaren time of flight mass spectrometer (WM-TOFMS)[37], which directs the anions present in the expansion down the flight path toward the second chamber and separates the anions in time based on their respective mass:charge

(m:z) ratios.

In the second chamber, a series of ion optics optimizes the direction of the anions as well as refines them spatially. The series of deflector plates ‘steers’ the beam so that it lands squarely in the center of the velocity map imaging (VMI) optics in the third chamber. Each set of deflector plates consists of a plate held at ground, and a plate with a positive or negative applied voltage. The first set is positioned to steer the beam in the left or right direction, and the second steers the beam up or down. Following the deflectors is an Einzel lens assembly, which focuses the beam into the photodetachment zone in the third and final chamber. Finally, before entering the third chamber, the anions pass by a mass gate consisting of a single charged plate that is rapidly switched on and off. The mass gate is set to a high voltage when anions other than the anion of interest are passing over it, knocking them into the walls of chamber two, then rapidly turned off while the ion of interest passes over it allowing it into the third chamber.

In the third chamber a series of three circular plates, referred to as the repeller, extractor, and ground respectively, with center drilled holes makes up the VMI optics. Additionally the third chamber is lined with  $\mu$  metal, which minimises the magnetic field inside the drift region of this chamber. While passing between the repeller and extractor a tunable laser fixed at a given wavelength intersects with the anion packet of interest, photodetaching electrons from the anions. These electrons leave the anion packet as a series of nested newton spheres that are cylindrically symmetrical with respect to the polarization vector of the laser, and have radii defined by the kinetic energy of the electron detached. These spheres expand along a drift region before impacting a chevron stacked set of multichannel plates (MCPs) that are backed with a short lifetime P47 phosphor screen. Each electron impacting the MCP stack generates an electron cascade through the MCP stack, which then impacts the phosphor screen causing it to glow.

Behind the third chamber, a charge coupled device (CCD) camera records every shot of the experiment and sends each image frame to a lab computer. Slightly behind and off the central axis of the CCD camera is a photomultiplier tube (PMT), which is used in the signal optimization for the experiment. Additionally, while recording data, the PMT voltage is cross referenced to ensure the maximal signal:noise ratio in a given image. The software used to record these images is discussed more thoroughly in Section 2.7.

The experiment is run at a 10Hz repetition rate, and is controlled by three delay generators. A schematic timing table which lists the relative trigger timings during a VMI recording, as well as how long each piece of the experiment remains on is shown in Table 2.1 for an average photoelectron image using our experiment. The  $\pm$  values refer to the average range of timing values rather than the uncertainty in the values, but occasionally the machine likes to be run outside these ranges. The largest impact on a given timing is normally the mass:charge ratio for the anion of interest. Because by nature a heavier anion will take longer to move through the apparatus, we generally find that the timings for heavy anions are substantially later than lighter anions.

Table 2.1: Average Relative Timings during a VMI recording

Item	Start	Duration	Type
EL Valve	$0\pm 10\mu s$	$25\mu s$	Active High
Minilite Laser (Ablation)	$85\pm 10\mu$	20ns	Active High
WMTOF	$150\pm 50\mu s$	$250\mu s$	Active High
Camera	$150\pm 50\mu s$	$220\mu s$	Active High
Mass Gate	$175\pm 50\mu s$	500ns	Active Low
Quanta-Ray Laser (Photodetachment)	$180\pm 50\mu s$	20ns	Active High
MCP	$180.05\pm 10\mu s$	30ns	Active High



## 2.2 Generation of Anions

Many methods for the generation of anions have been used in the literature ranging from pulsed discharge sources to kiln sources to laser ablation, among others[38, 39]. Unfortunately, when working with metals, the additional challenge of the bulk materials stability limits the generation methods substantially. Pulsed discharges become difficult to use due to the limited sources of volatile metallic complexes, and kiln sources require high temperatures that lead to dense low resolution spectra. In pulsed laser ablation, a short laser pulse is focused onto the surface of a sample, rapidly heating it and vaporizing a small portion of the bulk material through a multi photon absorption process. This vaporized sample comes off the surface of the sample as a hot plasma of neutral molecules, cations, anions, and free electrons. In modern pulsed ablation sources, this hot plasma is entrained in a driver gas pulse which rapidly cools the plasma through a process known as supersonic expansion which can produce molecules with rotational temperatures of 10K and vibrational temperatures of 50K or less[40]. In addition to the cold neutral molecules, cold anions and cations are also produced, albeit in lower concentrations. These conditions and the ability to use a bulk metal rod make laser ablation the optimal method of anion generation for our experiment.

A cutaway model of our laser ablation source can be seen in Figure 2.2. A rotating translating beryllium rod is placed inside of a block that has been machined from metal or 3D printed using commercially available filament, which is attached to our Even-Lavie valve [36]. When beginning our study of a given species, we generally can control the sample material, the composition and backing pressure of the gas that drives the expansion, the laser power and focus, and the manufacture method, shape, and material of the ablation block in addition to the timing between the gas pulse and the laser firing. Using these variables we can steer the ablation products toward a given species of interest to a certain degree.

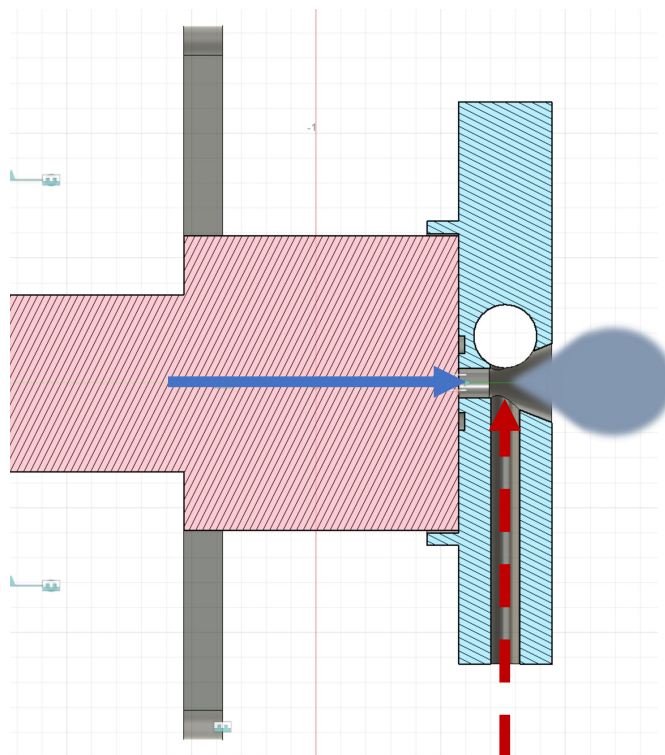


Figure 2.2: A cutaway of the pulse valve (pink hash marks) and ablation block (light blue hash marks). The blue arrow represents gas flow into the block, the dashed red arrow represents the laser pulse into the block, and the gray cloud represents the expansion plume.

In general, we have found argon gas to be the best driving gas in our expansions, producing the coldest expansions and most table signal. In addition to argon, most of our gas mixes will be seeded with one or more additional reactants to encourage the generation of our molecules of interest. In the case of pure metallic clusters like the  $\text{Be}_n^-$  ( $n=3,4,5$ ) we found that adding a few percentage of nitrogen greatly stabilized cluster formation compared to a pure rare gas expansion. We believe that this is due to the addition of rotational and vibrational modes of freedom for cooling the expansion, as opposed to purely translational collision cooling. In studies of non pure species, a reactant is added to the gas which contains the element of interest to be bound to beryllium. For example, in our study of  $\text{BeC}_2$ ,  $\text{C}_2\text{H}_2$  was added to the driver gas [14]. When choosing the reactant it is important to also consider a given elements accessibility in the molecule. It is more likely that if the element is strongly bound to

the reactant molecule it will not be liberated in the ablation process. This in some sense guides the choice of reactant molecules, as we constantly try to use molecules that weakly bind our element of interest to them. In the event that there is not a suitable gas phase reaction candidate we can also utilize an inline pressurized bomb filled with a solution phase reactant, that has the rare gas driver bubbled through it to carry small quantities of the reactant to the valve and into the expansion.

The choice of block manufacture method is decided based largely on convenience, but block material composition has also proven to have a large impact on the ablation products. For example, when using 3D printed blocks we often find substantial signal for assorted hydrocarbons which could only be generated by unintentional ablation of the block. Even given this, we often choose 3D printed blocks as the convenience outweighs the downsides. Additive manufactured blocks are able to integrate complex internal geometries more easily than machined blocks, which can be useful when attempting certain experiments, for example adding a secondary confined reaction zone downstream of the ablation zone to generate larger clusters or inject reactants. Generally, we have found that increasing the length of the gas exit channel and reducing its diameter has caused the reactions in the plume to tend toward the most strongly bound candidates. In many of our studies of more weakly bound systems we have found that a very short and wide conical exit channel, like that seen in Figure 2.2, will create the highest number of different species and improves the chances of seeing poorly bound systems. The choice of block material can also substantially influence the ablation products. A previous study in our lab on BeAl was accomplished after initially forming the diatomic using an aluminum block and Be rod [41]. As the rod rotates inside of the block, any rubbing on the block causes small amounts of the block material to transfer to the Be rod's surface. Additionally the hot plasma and reflecting laser light can cause the interior surface of the block to ablate, which may cause the block to become a reactant in the plume. In studies using a plastic block,

assorted beryllium carbides are often seen. In cases where the targeted species is a hetero-metallic complex, provided one of the elements is machinable in its bulk form, this property of the blocks can be exploited if there are very few options in the gas or solution phase.

Finally, the sample composition can be varied. While generally we use a pure Be rod in our experiments, various forms of surface chemistry can be attempted when all else fails. Experiments done previously on LiBe and LiMg used a beryllium or magnesium rod that had been rubbed with a lithium rod, depositing small amounts of lithium on the surface of the rod which formed the alkali earth-alkali molecules when ablated [42, 43]. Additionally, we previously had electroplated copper onto the surface of a beryllium rod, although generating large amounts of BeCu anions was still elusive at that time. Many commercial processes for surface chemistry also exist and may be worth exploring for particularly hard to create molecules, like attempting to nitride coat a beryllium rod to form BeN which has remained elusive in our lab to the current date.

## 2.3 Mass : Charge Discrimination

Following ablation, the plume is directed toward a small hole in a metal housing containing a Wiley-McLaren Time of Flight Mass Spectrometer (WM-TOFMS) [37]. The housing around the WM-TOFMS helps slightly isolate the radio frequency switching noise, and the small hole limits the ablation plume products entering the TOFMS to the center part of the ablation plume that is generally the coldest. Our WM-TOFMS is schematically shown in Figure 2.3. The WM-TOFMS functions using two circular charged plates and a circular grounding plate with an equal spacing between each of the plates. These plates are referred to as the extractor, repeller, and ground. The plates all feature a 25mm diameter hole in the center with a tight

## WMTOFMS Housing

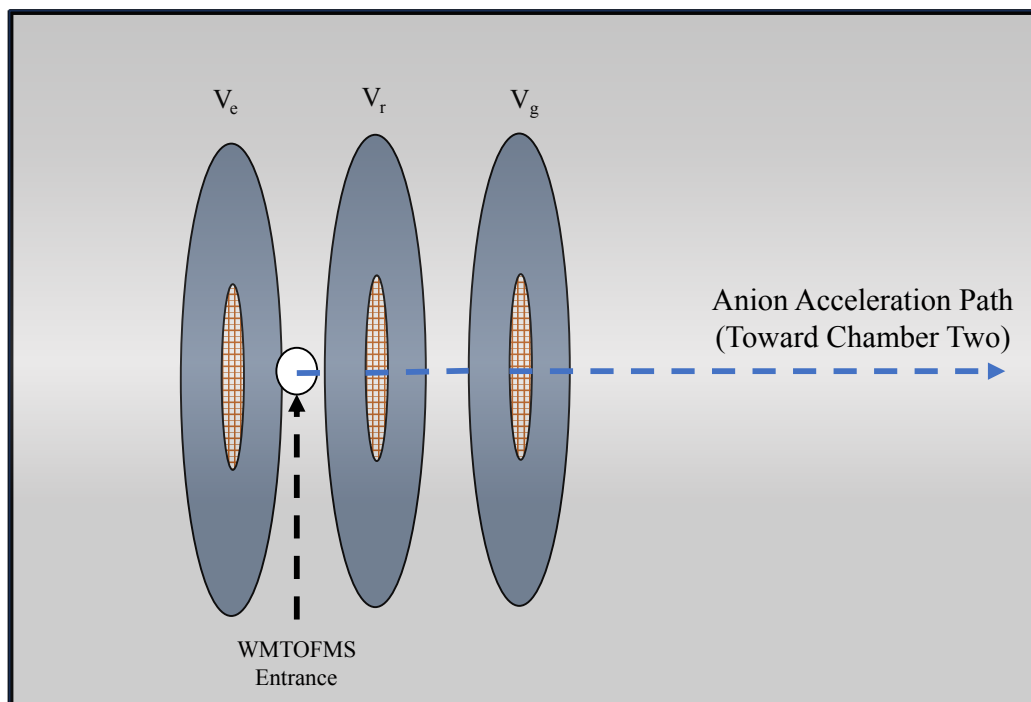


Figure 2.3: The basic layout of out Wiley-McLaren TOFMS. The plates are held inside a stainless steel tube (translucent grey box) with a small opening to allow ablation products to enter.

mesh copper grid placed over the hole. The copper mesh grid ensures a more uniform electric field over the axis of the TOFMS, while allowing the majority of the anions to be transmitted through. The extractor and repeller are pulsed with a user defined voltage in order to force the anions down the axis of the WM-TOFMS and separate the anions by mass:charge ratio. To tune the resolution and optimal mass range of the WM-TOFMS, the voltages as well as the delay between pulsing the plates can be adjusted. In a typical experiment, the repeller will be set to approximately  $-2.19\text{kV}$  and the extractor set to approximately  $-1.96\text{kV}$ , and the plates will be turned on at the same time. These voltages provide greater than 1 amu resolution for masses lower than 100 amu. Previously, the ‘on’ pulses were sent to the switching units with a slight delay (nanoseconds) between the extractor and repeller for optimal resolution, but current experiments have better results without any delay. It is possible that this

delay was due to a difference in length between the wires, and the delay in trigger pulses actually resulted in the voltages being applied to the plates at the same time, as this setting was changed after rewiring parts of the triggering circuits.

As the ablation products enter the WM-TOFMS, they fly between the the repeller and extractor plates. When the plates are turned on, the anions begin to gain kinetic energy due to the potential difference between the plates. Note that because the anions enter between the extractor and repeller, the acceleration potential they experience ( $\Delta V$ ) is not the exact potential difference between the plates. The velocity of the anions is given by

$$\begin{aligned} E_{ke} &= q\Delta V \\ \frac{mv^2}{2} &= q\Delta V \\ v &= \sqrt{\frac{2q\Delta V}{m}} \end{aligned} \tag{2.1}$$

or when referring to the travel time down the fixed distance down the instrument  $d$ , the time of flight  $t$  is found as

$$\begin{aligned} vt &= d \\ t &= d\sqrt{\frac{m}{2q\Delta V}} \end{aligned} \tag{2.2}$$

and we can quickly see that the flight time is dependent on  $\sqrt{m/q}$  of our anion of interest. Using this relationship we can map the flight times to their associated mass:charge ratio. Because the dianions ( $q = -2e$ ) are assumed to be very unstable, we use a fixed charge of  $q = -e$  for all peaks. Generally, when initially determining the mass spectrum calibration, we use masses of known strong signal anions. Often this is either a metal oxide, or an atomic anion with a high electron affinity like a halogen. To confirm the assignment of a given mass peak, a photoelectron spectra is taken, so using anions with well known anion photoelectron spectra is needed for the initial calibration curve. Using multiple peaks with known masses, a second order polynomial is fit to the timings, and this polynomial is used to predict the masses of

unknown peaks. These peaks are then assigned chemical formulas based on the mass of the peak and the elements present in the ablation plume.

## 2.4 Anion Optics

While the WM-TOFMS compresses the anion packets in the direction of travel down the flight axis, it is still necessary to use ion optics to correct for any off axis travel, as well as to focus the ions into a tight distribution radially to maximize the cross section between the anions and the photodetachment laser in the third chamber. These operations take place in the second chamber using two sets of parallel deflector plates and an Einzel lens, as shown in Figure 2.4.

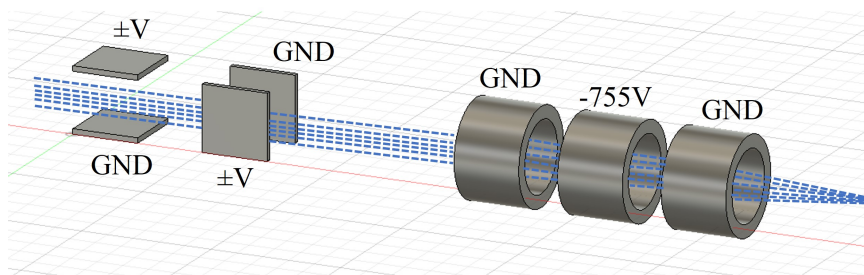


Figure 2.4: A diagram of the ion optics used in the second chamber. The parallel plate voltages are independently varied, and the Einzel lens is composed of three ring electrodes with a voltage applied to the center electrode.

The two sets of parallel plate electrodes are placed perpendicular to each other and consist of a grounded plate and a plate with an applied voltage. The voltages of each plate is varied independently by a dual polarity high voltage power supply. In average conditions, these voltages sit at approximately  $-130\text{V}$  and  $30\text{V}$  for the first and second plate set respectively. Following the parallel plate electrodes is an Einzel lens comprised of a set of three ring electrodes. The first and third electrode are held at ground, while the second has a variable voltage that has been set to  $-755\text{V}$ . The voltage of the second electrode and the kinetic energy of the ions passing through determine the focal point of the ion packet. This means that provided the TOFMS

voltages are unchanged, the Einzel lens voltage need not be changed. The optimal voltage for the Einzel lens is determined by varying the voltage slightly, then taking a SEVI image and monitoring the resolution of the resultant image. As the focal length of the Einzel lens is changed, the spatial cross section between the photodetachment laser and the anion packet changes, and the best resolution occurs when this cross section is at a minimum. Following the Einzel lens is a mass gate comprised of two more parallel plates that are not pictured in Figure 2.4. One of the plates is held at ground, and the other has a high voltage applied to it. As the anion of interest flies over the mass gate the high voltage plate is switched off rapidly, and then turned back on after the anion has passed through into the third chamber. This limits the anions in the third chamber to a single mass charge ratio during the photodetachment stage.

## 2.5 Velocity Map Imaging

The third and final chamber contains the velocity map imaging optics and detector. This chamber also is internally shielded by  $\mu$ -metal, which shields the photodetached electrons from stray magnetic fields that would distort their trajectories and the systems resolution. Anions are photodetached using vertically polarized light at a fixed wavelength from an Nd:YAG laser, Nd:YAG harmonic, optical parametric oscillator (OPO), or a dye laser. The wavelengths available in this experiment span from the near IR to UV, and the laser sources have resolutions below  $1 \text{ cm}^{-1}$ , which is substantially below the resolution of our experiment. Generally, higher laser power allows for more photodetachment, but too high of an intensity can cause electrons to be liberated from the inside of the chamber by a multi-photon photoelectron process. This problem is much more noticeable in the UV, where only two photons are needed to overcome the work function of the chamber and shielding materials, making high power UV scans infeasible. Under these conditions, the electrons liberated from the



chamber (from this point on referred to as scattered electrons) can greatly overwhelm the photoelectrons originating from the anion of interest. Because the microchannel plate (MCP) detector cannot differentiate scattered electrons from our photoelectrons of interest, the laser light entering the chamber must be carefully aligned, and in some cases it is intentionally weakened by an iris or filter to prevent excessive scatter. Generally in the visible and IR scattered electrons are negligible, with the exception of Nd:YAG fundamental and harmonic wavelengths, which produce high enough flux to cause this scattering. It is of utmost importance to ensure minimal to no scattering occurs, as it drastically increases the background noise of an image, and enough scatter can cause damage to the MCP stack.

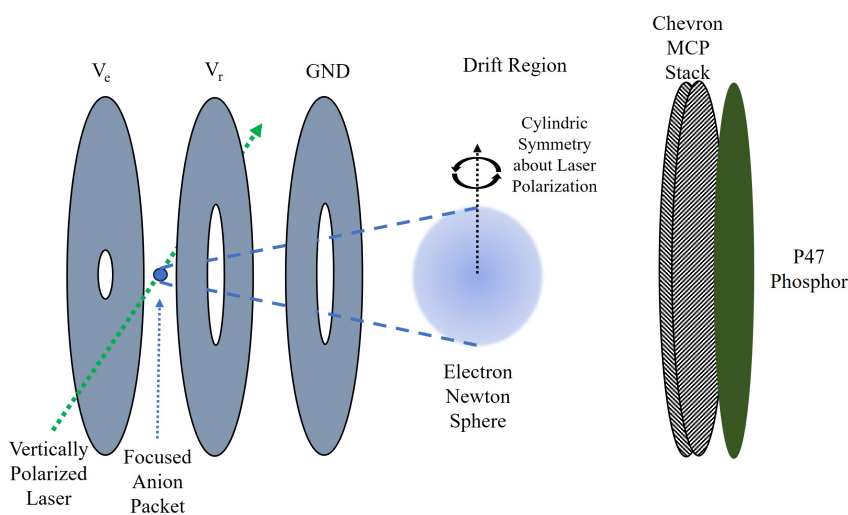


Figure 2.5: A schematic of the VMI optics including the MCP and Phosphor components of the detector.

An exact description including dimensions of the VMI spectrometer has been described previously [34, 35, 44]. The current section describes the general working principles and any changes to operating procedures. A schematic diagram of the VMI spectrometer is shown in Figure 2.5. The VMI is based on the original Eppink and Parker design, and consists of three stainless steel disk electrodes with center apertures [29]. These electrodes are referred to as the repeller, extractor, and ground,

and have a static voltage applied to them. The repeller and extractor voltages are applied as a ratio of  $1:0.726 V_e:V_r$ , which was found to be the ratio that provided the best resolution for our images. The exact voltage for optimal resolution is determined by trial and error around this ratio, using photodetachment of atomic sulfur anions which have a well studied anion photodetachment spectrum. The anion packet is photodetached between the repeller and extractor electrodes, causing the electrons to detach as nested newton spheres with radii determined by the electrons' kinetic energies and the drift time, and cylindrical symmetry about the laser polarization vector. These newton spheres impact the MCP stack, producing a two dimensional projection that is recorded by the detector. By increasing the extractor and repeller voltages, we can shorten the drift time from photodetachment to impact on the detector, which broadens the spectral range of the VMI at the cost of resolution. Similarly, we can lower the voltages to improve the resolution at the cost of spectral range.

Using higher repeller voltages to cover a larger spectral range has provided the ability to cover almost the entire visible range in a single image. Unfortunately, as you increase the spectral range, more eKEs are mapped to a single pixel on the detector, which can cause confusion in determining assignments. This necessitates using both survey conditions ( $V_e=1\text{kV}$ ,  $\text{range}\approx 10000\text{cm}^{-1}$ ) and high resolution conditions ( $V_e=300\text{V}$ ,  $\text{range}\approx 3000\text{cm}^{-1}$ ). In some cases, the extractor voltage can be turned down even further when resolution of only a few wavenumbers is needed. The resolution in eKE space maps non-linearly to the range of an image. Because the radius of the Newton sphere generated by photodetachment is determined by the square root of the eKE, the best eKE resolution occurs at lower eKE values where fewer eKE values map to the same pixel.

## 2.6 Electron Detection and Imaging

Photoelectrons travel down a field free drift region before contacting the front of our 75mm diameter chevron MCP stack, produced by PHOTONIS USA. This MCP stack creates an electron cascade that retains the spacial distribution of incoming electrons. The following P47 phosphor screen glows when hit by this electron cascade, again retaining the initial spacial distribution of the photoelectron newton sphere. Placed behind the phosphor screen is an IDS UI-2230SE-M-GL Rev. 3 CCD camera (1024 X 768), that feeds into a computer running in-house software to record the images. This software is further discussed in Section 2.7.1. In addition, a photomultiplier tube (PMT) is mounted behind and slightly off axis from the CCD camera. Both the CCD and PMT are attached to an aluminum tube, painted with low reflectivity black paint, mounted directly to the vacuum flange which holds the phosphor screen. This tube ensures the alignment of the camera and PMT with respect to the detector, and limits noise due to external light sources and reflections. The outside of this tube and the back of the final chamber are also wrapped in a blackout curtain wool material to further limit the entry of stray photons that would raise the background noise of the camera.

During the signal optimization portion of an experiment, the PMT is used to ensure that the molecular species of interest is being optimized. The time resolution of the PMT is substantially faster than the decay time of our phosphor screen (P47 decays to 10% its initial output in approximately 100ns), and the average mass peak has a perceived width of approximately 300ns. Note that because our mass spec is taken using the PMT and light from the phosphor screen, the actual time distribution from the front of the anion packet to the back is much shorter, on the order of 20ns as determined by the suitable range of photodetachment laser timings. In comparison, the CCD camera has a minimum exposure time of approximately  $47\mu\text{s}$ , which is much too coarse to resolve individual mass peaks in our WM-TOFMS.

During the electron imaging portion of our experiments, we can overcome the time resolution issues by rapidly switching the MCP voltages from low to high only during the time when photoelectrons are impacting the MCP. Because the gain in the MCP is heavily dependent on the MCP bias voltage, and the phosphor brightness is dependant on the quantity of the electrons hitting the screen, we can prevent large amounts of non-photodetachment noise from building using this type of delay gating. Additionally, because the electrons travel substantially faster than the anions that are not detached and the neutral molecules remaining after detachment, only the electrons will impact the MCP while it is highly biased if it is tightly gated in time. Once the electron signal is determined by the PMT, we begin our recording and the camera is triggered by our timing unit, and remains exposed for approximately  $47\mu\text{s}$ . During this time, any of the glowing portions of the phosphor screen are captured by the camera, and each ‘shot’ is sent to the lab computer to be recorded based on user set parameters discussed in Section 2.7.1. It is worth mentioning that the camera sensor and lens combination used forms a weak portion of the experiment, as these are poorly matched to record the short wavelength of P47 phosphor which emits at 400nm. A new camera with a higher resolution and better efficiency at this short wavelength, and a lens with high transmittance in this spectral range could improve signal by up to two times. This upgrade, while in progress, has not been completed, as it requires a revision to the software and mount for the camera.

## 2.7 Software and Processing

The software used in this experiment generally falls into three categories: acquisition, pre-processing, and processing. The acquisition and pre-processing software were written in house using LABVIEW and python respectively, while the processing is done using the MEVELER software written by Dr Bernhard Dick [45].

### 2.7.1 Acquisition

The acquisition software interfaces with the camera and the PMT, and stores each individual shot of the experiment, as well as the voltage on the PMT during each shot. The software also allows a recording of the entire WM-TOFMS at once, but due to the slow communications between the oscilloscope which normally outputs the WM-TOFMS signal and computer this feature should only be used occasionally. To overcome the slow communications, the PMT signal is monitored by a boxcar integrator and digital to analog converter (DAQ) during the imaging portion, and this voltage is used in place of the direct waveform from the PMT. The individual shots are transmitted to the computer and stored as a simple integer array the size of the camera sensor, while the PMT voltage is stored as a float (32-bit decimal value). The PMT voltage is cross referenced for each shot of the experiment, and only shots with signal higher than the user designated minimum are saved in the final image. A secondary image is simultaneously acquired without any shot to shot rejection, and can be used as a backup image in the event that there is a problem with the PMT based rejection. Additionally, both of these images are saved every few minutes (the exact time is user designated) to prevent total data loss in the event of a computer power failure, or any other issue with the signal acquisition. This software algorithm is shown in an flowchart in Figure 2.6. Due to space requirements, only these accumulated images are permanently saved, rather than individual shots which would quickly become too storage intensive to maintain. This allows the image to be ‘rolled back’ to a known good image should the signal deteriorate overtime due to things like timing drift or laser power drift increasing background scatter. In order to better record experimental settings, the software also has several data fields that record timings, voltages, reactants, and other information regarding the settings of the experiment, all of which are output to a text file at the end of a recording. All data from each image is saved to a directory, which is given a name based on the

date and time the recording began and the anion of study to provide a simple way to maintain records across several images of the same molecule.

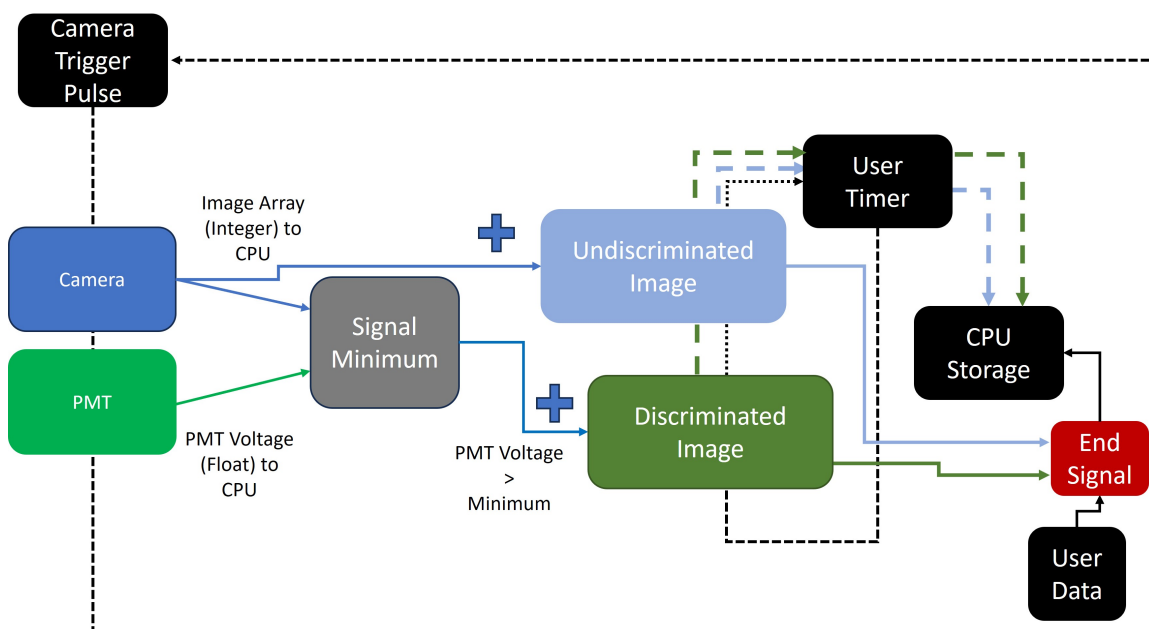


Figure 2.6: A flowchart showing the image acquisition software algorithm.

This shot rejection scheme has proven immensely valuable, and has allowed us to study molecules that we could previously not image due to high amounts of noise generated by dark currents in the camera sensor. A comparison of a signal discriminated image and a non discriminated image of the beryllium trimer anion as well as the MEVELER spectrum of both can be seen in Figure 2.7.

This scheme, while effective, can be further improved by a new revision to the software and using a higher core count computer. This new software version will be moved to Python, and be parallel rather than the current and largely sequential LABVIEW implementation. This implementation will use a thread to do the comparison, a thread to interface with the camera, a thread to write to disk, and finally a thread to compress and save each shot. Because the average shot has relatively few data points, the raw data array compresses extremely effectively to reduce the storage requirements. With every shot saved in its compressed form and the PMT voltage

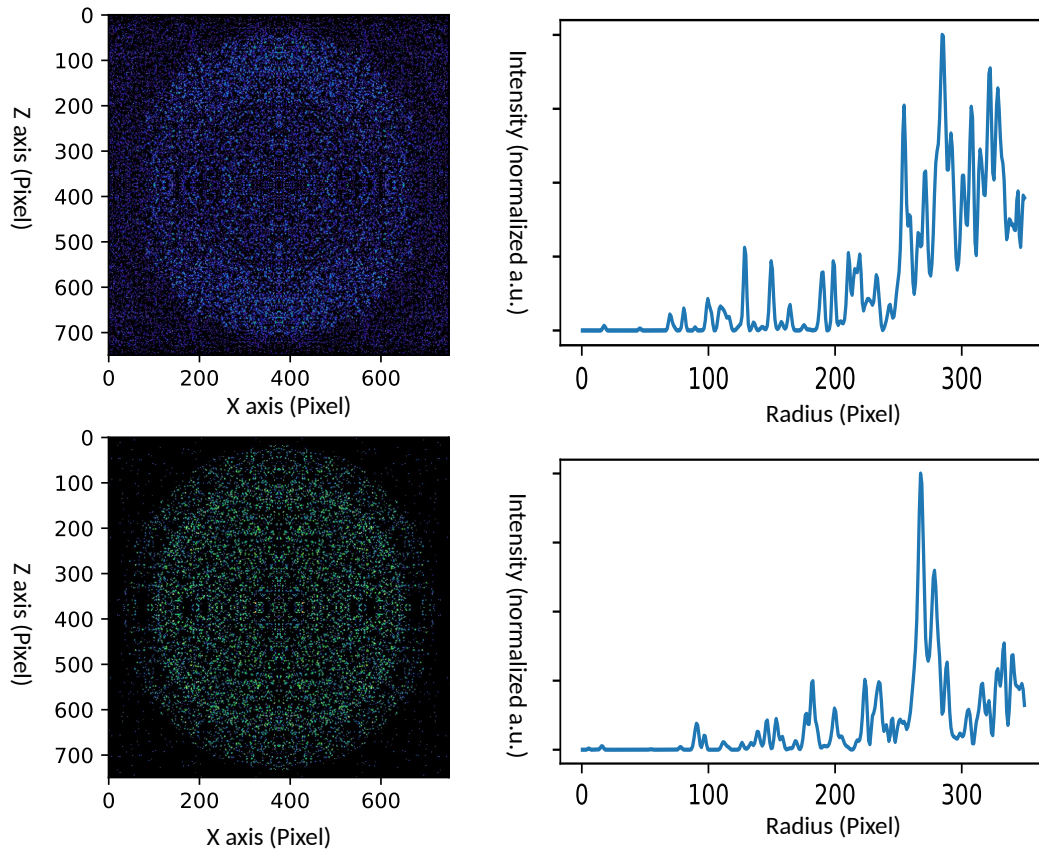


Figure 2.7: A comparison of the raw images (left column) and processed spectra (right column) with signal based discrimination (bottom) and without signal based discrimination (top). The top row shows the inclusion of all shots, while the bottom shows only shots where the photomultiplier tube registered voltages above a baseline value.

associated with each shot saved, it is possible to retroactively set the minimum signal voltage for an image and generate images using varying signal:noise ratios. While the current software lacks centroid functionality, several different software centroiding methods have been shown to allow for a sub-pixel resolution in these experiments [46], and parallel processing of these images would allow us to maintain a raw and centroid image for comparison of the two. Additionally saving every individual shot would allow us to determine their centroid images at a later time and with varied parameters.

## 2.7.2 Pre-Processing

The pre-processing software serves two main purposes, and has several utilities that are largely for troubleshooting. To understand the first purpose, it must be noted that the camera sensor is not spatially even in its response to light. The sensor has several ‘hot pixels’ that report unfeasible signal values on impact and provide a skew in intensity. For example, one pixel may report a value of several hundred while all other pixels have values from zero to a few tens. In this case, statistical methods are used to determine the average value of all pixels with any electron impacts, and these hot pixels are normalized to this value plus three standard deviations. This retains some value on these pixels, but prevents them from skewing the processed spectrum based on one or two values several orders of magnitude above what is statistically likely.

Following this normalization procedure, the software finds the center of the VMI image, and outputs a symmetrized version of the image according to the guaranteed symmetries of the photodetachment process. To find the initial centers, a binary map of the image is created where pixels with high intensity are set to a value of one, and pixels with low intensity are set to a value of zero. The high and low intensity thresholds are determined based on the average of pixels with nonzero value. This binary image is then run through a modified Hough transform [47] which finds circles, as implemented in the OpenCV python library[48]. This program outputs an estimate for the radius of the circles it sees in an image, as well as the pixels of its center. This guess is then shown to the user, who may chose to refine it manually or proceed with the guess. The normalized image is then symmetrized by folding along the x (horizontal) and z (vertical) axis through the center of the image. The user is given the choice of which of the four quadrants of the image to use in the symmetrized output, which can be selected to remove errors due to damage in the MCP stack or phosphor screen. Provided the center of the image was chosen accurately, and the



detector is not damaged, any combination of quadrants should result in the same spectra after processing. As such, the program will produce multiple symmetrized images using different subsets of the whole image if instructed, and show the user their MEVELER spectra to assist in determining if the centers were accurately determined. If the spectra of all of the different subsets are the same, the image can be considered properly centered.

In addition to these main features, the software can interface with the MEVELER program and the acquisition program to process all of the saved images from an imaging run, and display the evolution of both the image and spectrum over time. This can be useful to determine when enough signal has been acquired to render an image ‘done’ based on when the spectrum begins to only show minimal changes after sequential time steps. Similarly, the program can be instructed to create a gif file showing the image acquisition over time, which can be used diagnostically to determine signal quality over time or simply to produce fun images for use in presentations.

### 2.7.3 Processing

As has been previously mentioned (see Sections 1.2 and 2.5), when electrons are detached from an anion by linearly polarized light, they form nested Newton spheres with an axis of cylindrical symmetry defined by the polarization vector. In our experiment, this is vertically polarized light (up and down with respect to the MCP stack), which we define as the  $z$  axis. Additionally we define the  $y$  axis as the TOF axis, and the  $x$  axis is mutually orthogonal to the  $y$  and  $z$  axes (corresponding to left and right on the MCP stack). The VMI optics project these three dimensional Newton spheres into the MCP stack, where they are crushed down to their two dimensional discrete image projection which we define as  $D(z, x)$ . In order to obtain the kinetic energy of the photodetached electrons, we must create the velocity map of our photodetached

electrons, which we define as  $F(z, r)$ . Since both  $F(z, r)$  and  $D(z, x)$  are both two dimensional, it is apparent that all information to go between the two is contained in each function. For a known velocity map  $F(z, r)$ , the exact two dimensional image  $A(z, x)$  can be calculated using the forward Abel transform given by [45, 49]

$$A(z, x) = 2 \int_x^\infty F(z, r) \frac{r dr}{\sqrt{r^2 - x^2}} \quad (2.3)$$

and the velocity map for a known image  $A(z, x)$  can be obtained by the inverse Abel transform given by

$$F(z, r) = \frac{-1}{\pi} \int_r^\infty \frac{\partial A(z, x)}{\partial x} \frac{dx}{\sqrt{x^2 - r^2}} \quad (2.4)$$

While this may appear simple, for a discrete two dimensional discrete image like that created by our experiment, this problem is rather ill defined [45, 49]. Because this problem has a singularity at  $x = r$ , numerical solutions are rather hard to compute, and require some amount of smoothing. Even in instances where computation is possible, it is not always reliable, and several different methods have been proposed to solve this problem in a repeatable way. A decent review of several numerical methods for solving the the inverse Abel transform can be found in Ref [49]. In addition to purely numerical methods, which we have found unreliable in some cases, there also exist some statistical methods to determine the velocity map without directly performing an inverse Abel transform. Because these are statistical methods, they treat random noise qualitatively better, and perform better with images that have less signal.

The method we have chosen to use in our experiments is the Maximum Entropy Velocity Legendre Reconstruction (MEVELER) method [45]. In this method, the need for an inverse Abel transform is neglected entirely, and the velocity map is found treating the problem variationally, and finding the map that has the highest probability of producing the image. This method removes the problems with singular-

ities in the inverse Abel transform, lending much better stability. In the MEVELER program, the map is created as an expansion of Legendre polynomials, which are then modified to best recreate the data map  $D(z, x)$  that we have input into the program. An exact analysis of MEVELER as well as its comparisons to a few other methods can be found in Ref [45]. The MEVELER software takes the raw image output from the acquisition software, or the pre-processed image from the pre-processing software, and generates a spectrum of the intensity vs radius, as well as the velocity map and a simulated version of the image.

## 2.8 Spectrum Calibration

The velocity space spectrum output by MEVELER is calibrated to eKE space using known transitions of an atomic anion, generally  $S^-$ . Sulfur has a series of 6 relatively strong anion to neutral transitions from approximately  $16250\text{cm}^{-1}$  to  $17350\text{cm}^{-1}$ , which is a very convenient range in terms of laser availability. These photodetachment energies are easily accessible by both Nd:YAG 2nd harmonic lasers and efficient dye lasers. Because the relationship between electron binding energy (eBE) and eKE is given simply by  $eKE = h\nu - eBE$ , for a known photon energy  $h\nu$  and known eBE we can easily determine the eKE. Additionally sulfur anions are readily produced by bubbling a driver gas through liquid  $CS_2$  in our experiment before ablating a metal rod, which allows for quick image acquisition when running calibration images.

Energy calibrations use these known transitions to fit a simple second order polynomial to transform from velocity space to eKE space. This second order polynomial is then used for unknown transition energies and radii. To ensure there is good agreement between the polynomial fit and the known transition data, several calibration images are taken at varying photodetachment wavelengths. Finally a sulfur anion im-

age is taken at a known wavelength, and the energies are checked against the values given by the polynomial fit. This process is repeated for all VMI repeller voltages, generating an independent fit for each. A pixel space  $S^-$  photodetachment spectrum, as well as the corresponding eKE and eBE spectrum are given in Figure 2.8.

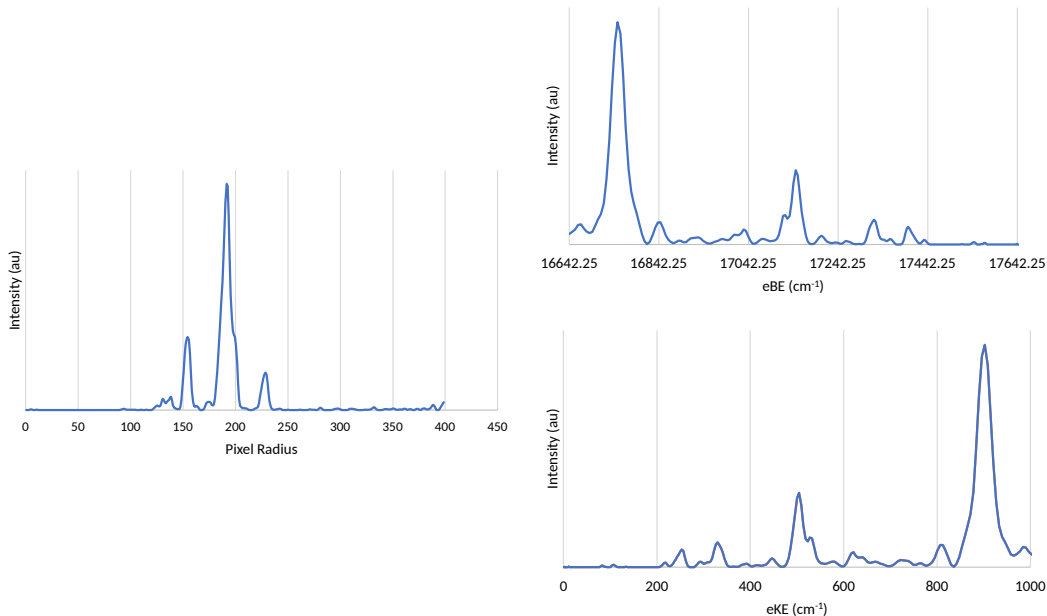


Figure 2.8: A sample Sulfur anion spectrum in units of Pixel (left), eBE (top right), and eKE (bottom right).

## 2.9 Experimental Upgrades

Over the course of the last several years, small sections of the experimental apparatus have been upgraded. The most notable of these has been the transition from a Jordan TOF style pulse valve to the currently used Even-Lavie (EL) style pulse valve [36]. In installing this new pulse valve it was also necessary to redesign the entire ablation source, and the new source was found to be substantially more stable in anion generation than the previous. The new source, shown in Figure 2.9, uses a 3/8-12 ACME threaded rod attached to a commercially available NEMA17 stepper motor in conjunction with two 3/8" ground shafts to move a translation stage vertically. The

translation stage holds a second NEMA17 stepper motor which is directly coupled to the source rod of interest. This design provided much more consistent translation than the original which used a rail to guide the translation coupled with a guide wire attached to a stepper to move it vertically, and was prone to binding. Additionally, it was found that by packing the stepper motors with vacuum grease, the operational lifetimes of the motors were extended by orders of magnitude. Previously, these motors would need to be replaced after roughly six months of vacuum run time due to short circuits in the motor wiring caused by excessive heat, and after grease packing them we have not needed to replace them in over four years. Presumably this is because the vacuum grease allows better cooling of the motor wiring and prevents the wiring from heating past the insulation breakdown point.

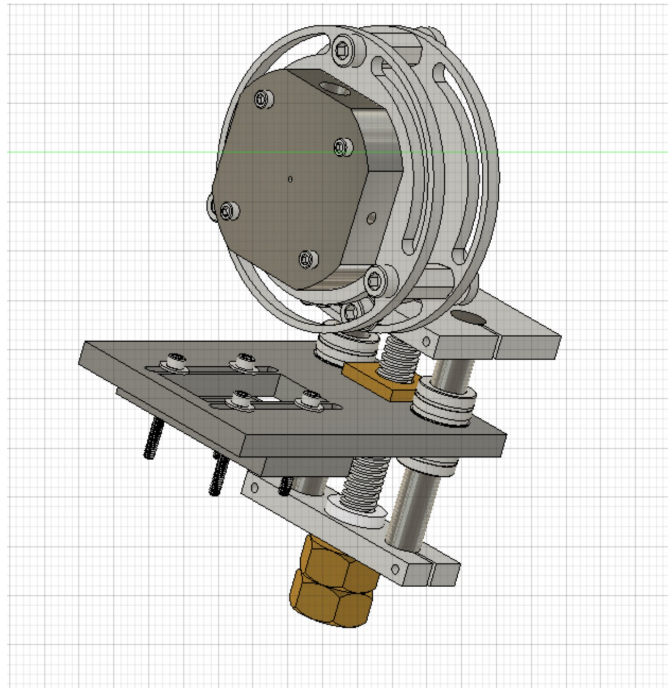


Figure 2.9: A CAD model of the original Even-Lavie ablation source. Motors and the source rod are not shown in this image.

Slight changes were made to this original EL V1.0 ablation source to make it more suitable for manufacture by 3d printing. These largely consist of creating thicker parts, or adding reinforcements that are not needed with metal parts. Additionally

it was found the the translation stage needed to be printed using more thermally resistant materials like poly-carbonate (PC), rather than the poly-lactic acid (PLA) filament we normally used, as the PLA was found to warp where it came in contact with the stepper motors in vacuum due to the heat generated by the motors. This V1.1 3d printed source is the current model in use in our experiment, but in the interest of “fixing what ain’t broke” a V2 source has been designed for manufacture as well. This V2 source fixes a few problems with the maintenance aspect of the V1.1 source, and doubles down on rigidity, serviceability, and vacuum suitability.

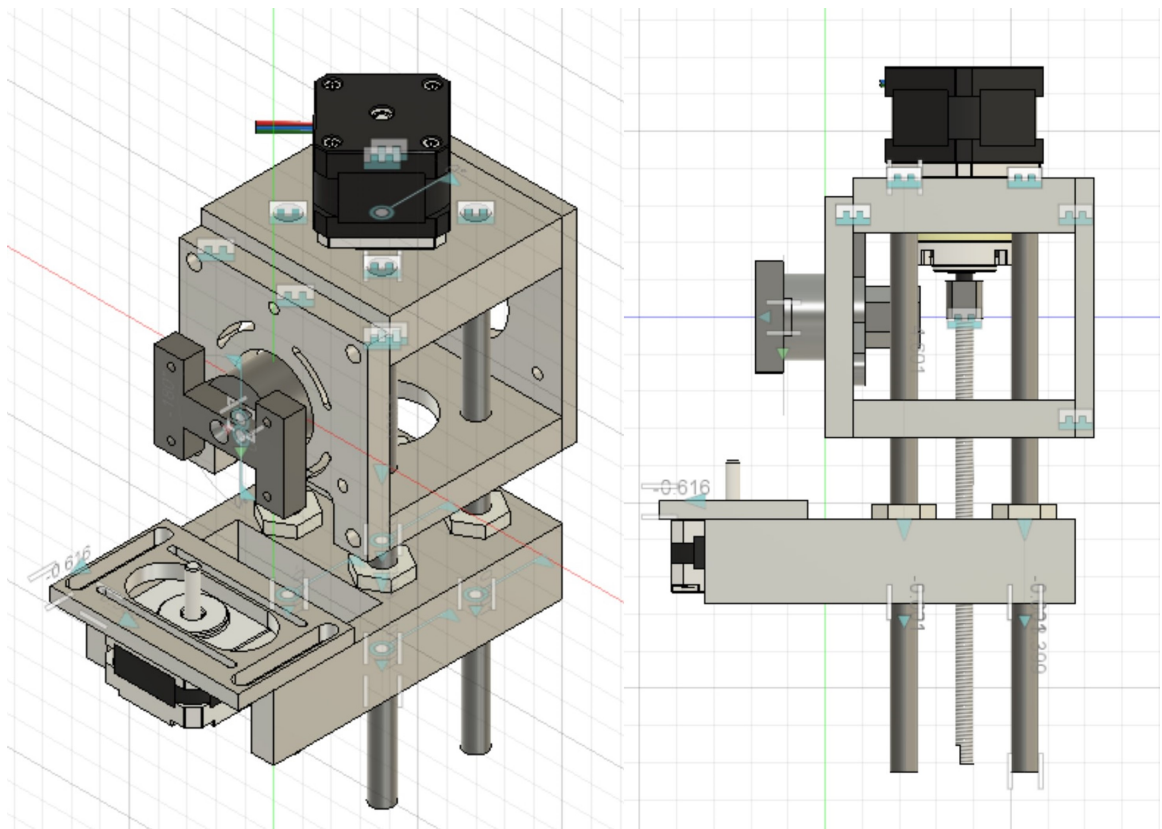


Figure 2.10: A CAD model of the V2 EL ablation source. The left side shows a perspective view from the top front corner and the right shows a view from side-on.

The V2 source, shown in Figure 2.10, is designed with better user serviceability, and even more rigidity. The main qualm with the current V1.1 source is that in order to service the valve, the entire ablation source must be disassembled. Additionally, the translation motor still has occasional binding when the threaded rod is

not properly lubricated or if the source rod is not perfectly mounted in the ablation block, increasing friction. The new source fixes both these problems by introducing a new rear master plate which the translation stepper motor and pulse valve attach to independently. To assist with binding on the translation motor, the previous pancake style motor is replaced with a full size NEMA17 motor that is run through a torque multiplying gearbox. For ease of manufacture, and to reduce the torque needed to rotate the rod, the 3/8-12" ACME thread is replaced a 1/4-20" thread that is machined directly to a motor coupling. The dual ground shafts are replaced by four ground shafts set up in a square arrangement to assist with keeping the stage totally perpendicular to the threaded translation rod and prevent binding due to uneven torque on the threaded rod. These shafts seat into low friction PTFE bushings that are threaded into the translation stage to minimize friction and assist in alignment. In the event that PTFE proves unsuitable due to fast wear, these threaded bushings will be remade using an oil-impregnated bronze. The guide shafts now also are extended and pass through the new translation motor top mount plate to ensure vertical alignment remains as precise as possible. The ablation block has also been altered to allow for slightly more rod translation before interference with the rod coupling.

Additionally, the design for the new ion trap equipped version of our apparatus has been finalized in CAD. The new version will include the ion trap apparatus specified previously [35]. A new chamber support layout, as well as fully adjustable chamber-support mounts were designed, and are ready to be installed pending break long enough to break down and rebuild the apparatus. The chamber mounts act as rollers that are able to level each chamber independently, and separate the chambers from each other for ease of maintenance. Additionally the new support design allows for easier movement of the apparatus around the lab by means of high load casters, and isolates the apparatus from vibrations in the floor by using feet with rubber dampening pads. This schematic is shown in Figure 2.11.

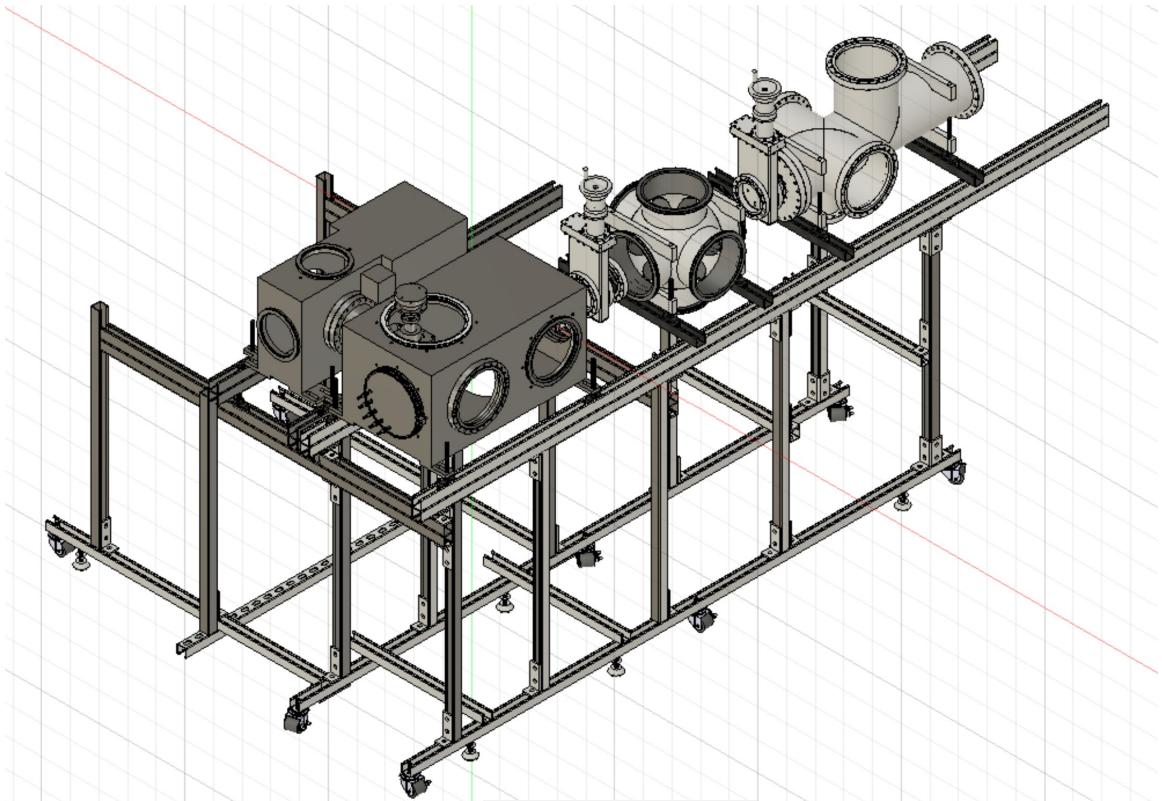


Figure 2.11: A CAD model of the experiment after installation of the ion trap chambers.



## Chapter 3

# A Quirky Little Guy: The Beryllium Trimer and its Anion

Contents from this section have been reprinted or adapted from Ref [50]:

Noah B. Jaffe, John F. Stanton, and Michael C. Heaven.

Photoelectron Velocity Map Imaging Spectroscopy of the Beryllium Trimer and  
Tetramer

The Journal of Physical Chemistry Letters 2023 14 (37), 8339-8344

DOI: 10.1021/acs.jpcllett.3c02169

Computational studies of small beryllium clusters ( $\text{Be}_n$ ) predict dramatic, non-monotonic changes in the bonding mechanisms and per-atom cohesion energies with increasing  $n$ . To date, experimental tests of these quantum chemistry models are lacking for all but the  $\text{Be}_2$  molecule. In the following section we report spectroscopic data for  $\text{Be}_3$  obtained via anion photodetachment spectroscopy. The trimer is predicted to have  $D_{3h}$  symmetric equilibrium structures for both the neutral molecule and the anion. Photodetachment spectra reveal transitions that originate from the  $X^2A_2''$  ground state and the  $1^2A_1'$  electronically excited state. The state symmetries were assigned on the basis of anisotropic photoelectron angular distributions with assistance from *ab initio* computations. The electron affinity of  $\text{Be}_3$  was determined to be  $11363(60) \text{ cm}^{-1}$ , and the  $\text{Be}_3^- 1^2A_1'$  electronically excited state was found to be  $2579(80) \text{ cm}^{-1}$  above the anion ground state.

### 3.1 Introduction

Small beryllium clusters have long been the topic of theoretical study, with a specific focus toward the clusters between two and six beryllium atoms [4–6, 8, 9, 11, 12, 17, 51–53]. The changes in bonding in this range are predicted to be dramatic and non monotonic as the size of the cluster increases. The  $\text{Be}_2$  and  $\text{Be}_3$  clusters are both predicted to be unbound at the Hartree-Fock self consistent field (SCF) level of theory [2, 53]. Bound potentials for these molecules only develop with sufficient electron correlation treatment is applied [1, 9, 54]. Despite this, experimental evidence shows the Be dimer to be bound with a formal bond order of zero and a  $D_e$  of  $934.9\text{cm}^{-1}$  [1, 19]. This dissociation energy is much larger than that of a simple van der Waals interaction between small atoms, and the  $2.444\text{\AA}$  bond length in the dimer also suggests a reasonably strong interaction. High level electronic structure studies predict that the energy needed to remove one Be atom from a  $\text{Be}_n$  cluster has non-monotonic dependence on  $n$ , and this result is present in both *ab initio* and DFT methods [6, 8, 9, 11, 17].

Despite the interest in these  $\text{Be}_n$  clusters, previous spectroscopic studies have only been presented for the  $\text{Be}_2$  neutral and cation [1, 19]. Previous attempts to use laser excitation techniques to study the electronic structure of  $\text{Be}_n$  clusters with  $n \geq 3$  in our lab proved unsuccessful. Fortunately, a previous photoelectron study on  $\text{Mg}_n$  clusters [55] was successful in forming the  $n=3-35$  clusters. In the Mg study, the electron affinity (EA) and gap between the EA transition and onset of features due to electronic excitations in the neutral molecule was measured. This energy gap was interpreted as an indication of the HOMO-LUMO gap within a Koopman’s model approximation, and the closing of this gap was equated with the onset of bulk metallic character. A Previous mass spectrum showing the  $\text{Be}_n^-$  clusters from  $n=2-6$  had been published as well [56], lending feasibility to an anion based study of the  $\text{Be}_n$  clusters. Additional theoretical studies of the smaller  $\text{Be}_n$  anions have also been

reported [51, 52, 54, 57]. A recent MRCI study reported the  $\text{Be}_3$  EA to be  $11125\text{cm}^{-1}$ , and predicted that the equilibrium structure of the  $\text{Be}_3$  anion ground state was very similar to that of the neutral molecule, both being  $D_{3h}$  with an equilibrium bond length of  $2.1\text{\AA}$  in the anion and  $2.2\text{\AA}$  in the neutral molecule [54]. Given this history, we have decided to use slow electron velocity map imaging (SEVI) spectroscopy to study these beryllium cluster anions.

## 3.2 Experimental Procedure

An in depth description of the experimental apparatus can be found in Chapter 2. The details specific to  $\text{Be}_3$  and a brief overview are found here. Pulsed laser ablation of a pure beryllium rod in argon backing gas using the focused fundamental output of an Nd:YAG laser (1064nm, 100mJ/pulse) was able to produce workable signal for imaging in our apparatus. It was found that adding a small amount (1-5%) of  $\text{N}_2$  to the argon backing gas provided a good third body collider in the supersonic expansion process, and assisted in stabilizing signal as well as cooling the anions more effectively. Gas pulses were produced using an Even-Lavie type valve with a backing pressure of approximately 1000PSI. The supersonic expansion was directed into our WM-TOFMS where all anions were directed down the TOF axis. As the anions travel, they are mass separated in time, and pass over a series of steering optics and Einzel lens. The steering optics serve to condition the beam and ensure it is traveling as axially as possible, and the Einzel lens focuses the anions into the photodetachment region in the final chamber. As the anions leave the second chamber, they pass over a mass gate which rapidly turns off as the anion of interest passes over it, allowing it to pass into the final chamber. The final chamber contains the VMI optics, where the electrons are photodetached from the anions using a vertically polarized photodetachment laser. These experiments used a photodetachment wavelength of 532nm

for the survey conditions, produced using the second harmonic of an Nd:YAG laser. 735nm and 890nm wavelengths were used for the high resolution images, produced using an optical parametric oscillator (OPO). OPO wavelengths were confirmed using a Bristol Wavemeter. These photodetached electrons are then focused onto our chevron stacked MCPs, which in turn light up a phosphor screen that is recorded by a CCD camera. The CCD camera output is fed to the lab computer, which discriminates high signal shots from low signal shots based on the voltage output of a photomultiplier tube (PMT) that also views the phosphor screen, as described in Section 2.7.1. Approximately 2% of all shots were kept in the final images for  $\text{Be}_3^-$ . Images were pre-processed using custom written python software described in Section 2.7.2, and processed using MEVELER [45]. Image reconstructions were produced in python using the output of the MEVELER software. Calibrations of the spectra were performed using known transitions of the  $\text{S}^-$  anion as described in Section 2.8.

### 3.3 Results and Discussion

Figure 3.1 shows a survey photoelectron spectrum of  $\text{Be}_3^-$  with an inset velocity map image. Linearly polarized light was used for photodetachment and the double-headed arrow next to the image shows the orientation of the polarization. The electron binding energy is given by the difference between the energy of the detachment photon and the kinetic energy of the photoelectron. Figure 3.1 is dominated by two prominent features, separated by approximately  $2500 \text{ cm}^{-1}$  in energy. Interestingly, with guidance from the high-level theory predictions shown in Table 3.1, we assign the lower binding energy feature to the  $\text{Be}_3^- 1^2\text{A}'_1 \rightarrow \text{Be}_3\text{X}^1\text{A}'_1$  transition. This assignment is further supported by the parallel anisotropy present in the velocity map image (anisotropy parameter  $\beta=2$ ), consistent with an  $\text{A}'_1 \rightarrow \text{A}'_1$  transition. We have not attempted to assign the weaker features of Figure 3.1 as they were not sufficiently

reproducible in successive measurements.

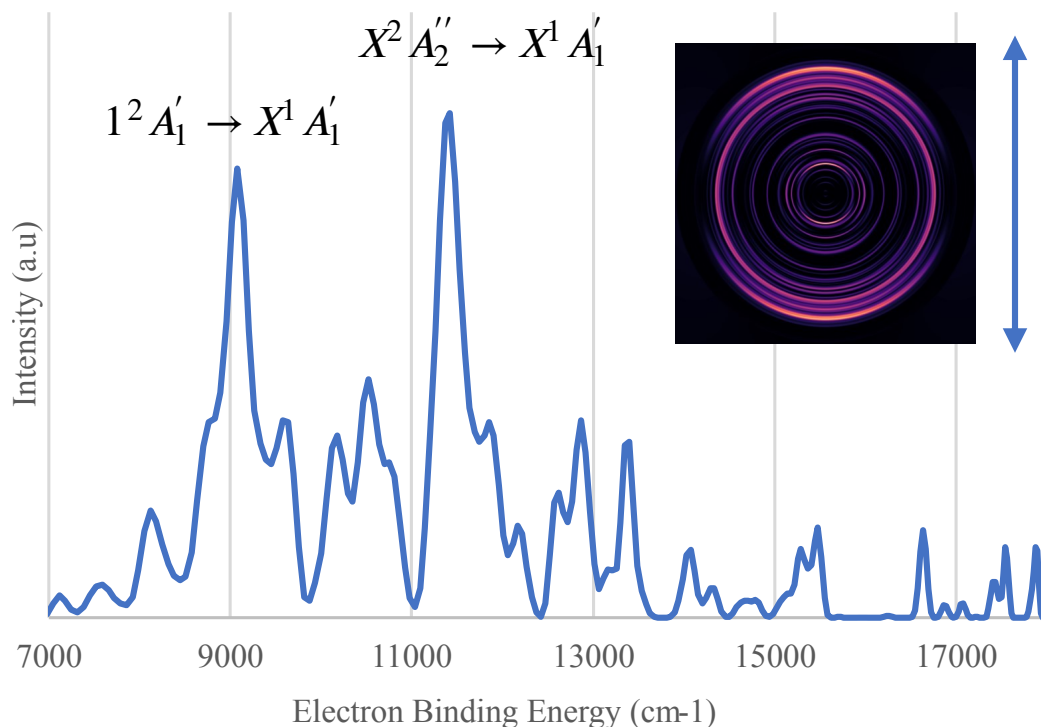


Figure 3.1: Photoelectron survey spectrum of the  $\text{Be}_3^-$  anion taken with detachment photon energy of  $18797\text{cm}^{-1}$  (vertical polarization shown by blue double sided arrow). The strongest electronic transitions have been labeled with guidance from high-level electronic structure calculations. Inset photo shows the velocity map image produced by MEVELER software

Using SEVI, it is possible to improve resolution by reducing the eKE of the photoelectrons, and reducing the voltage on the VMI extractor plates [33]. A higher resolution image of the low energy feature at approximately  $9000\text{cm}^{-1}$  was obtained using  $11236\text{cm}^{-1}$  (890nm) detachment photons. The result, shown in Figure 3.2 with its image reconstruction, gives an electron binding energy (eBE) of  $8784 \pm 40\text{cm}^{-1}$ . This error is given as a  $2\sigma$  value, which was determined by converting the error in pixel space from the original image into its equivalent value in eKE space.

The second prominent peak in Figure 3.1 is assigned to the  $\text{Be}_3^- X^2 A''_2 \rightarrow \text{Be}_3 X^1 A'_1$  origin transition. A higher-resolution spectrum and image for the  $\text{Be}_3^- X^2 A''_2 \rightarrow \text{Be}_3 X^1 A'_1$  transition is presented in Figure 3.3. This measurement yielded an EA of

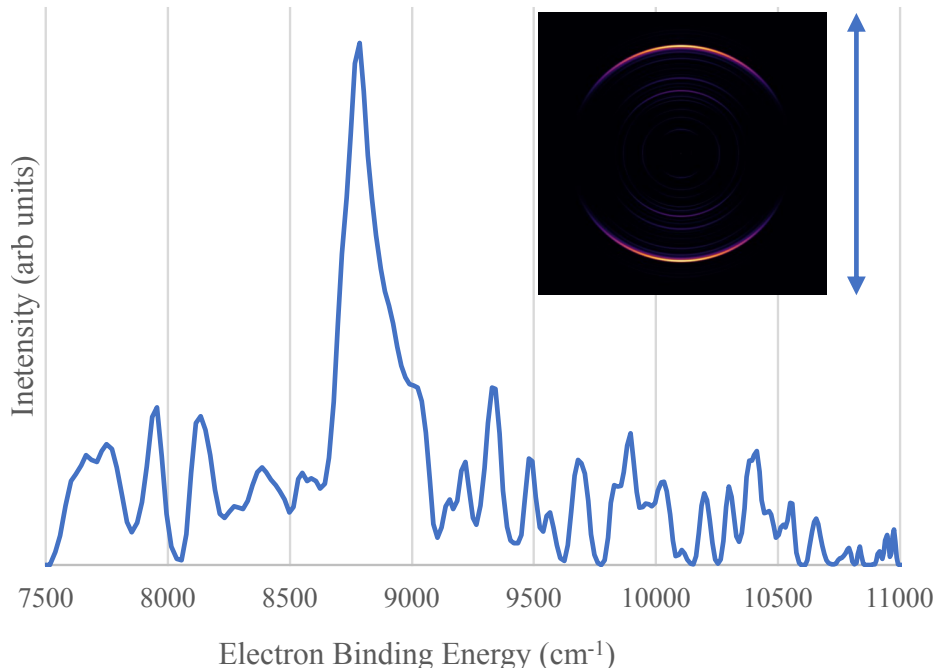


Figure 3.2: Photoelectron spectrum of  $\text{Be}_3^-$  taken with a detachment photon energy of  $11236 \text{ cm}^{-1}$  (vertical polarization shown by double sided blue arrow). Inset photo shows the velocity map image produced by MEVELER software.

$11363(60) \text{ cm}^{-1}$ , in good agreement with the present EOMEA-CCSDT calculations (Table 3.1) and previously reported MRCI studies [54]. The image shows a reasonable amount of perpendicular anisotropy, with  $\beta = -0.5 \pm 0.3$ , which is consistent with the predicted symmetries of these states. Interestingly because the smaller peaks just left of the EA peak show near parallel anisotropy, the EA peak in the survey spectrum (Figure 3.1 appears to show S wave detachment. This apparent S wave detachment is an artifact of these different peaks collapsing to almost the same radius under the survey conditions, and the high intensity part of this peak still shows an anisotropy of  $\beta = -0.5 \pm 0.3$ .

To gain further insight into the experimental data, ab initio computations were carried out using the CFOUR package[58]. Dunning correlation consistent basis sets[59] were used along with several different coupled-cluster treatments[60–64]. Electronic energy predictions are given in Table 3.1 and geometry parameters are given in Table 3.2. Harmonic frequency predictions are given in Table 3.3.

Table 3.1: Be<sub>3</sub> Transition Energies

Transition	Method	Basis	Energy (cm <sup>-1</sup> )	$\Delta E_{exp}$
Be <sub>3</sub> <sup>-</sup> X <sup>2</sup> A <sub>2</sub> <sup>''</sup>	EOMEA-CCSD	aug-cc-pCVTZ	10193	-1170
→Be <sub>3</sub> X <sup>1</sup> A <sub>1</sub> <sup>'</sup>	EOMEA-CCSD	aug-cc-pCVQZ	10408	-955
	EOMEA-CCSDT	aug-cc-pCVTZ	11575	212
	EOMEA-CCSDT	aug-cc-pCVQZ	11774	411
	MRCI [54]	aug-cc-pV5Z	11125	-238
	Experiment	–	11363(60)	–
Be <sub>3</sub> <sup>-</sup> 1 <sup>2</sup> A <sub>1</sub> <sup>'</sup>	EOMEA-CCSD	aug-cc-pCVTZ	7912	-872
→Be <sub>3</sub> X <sup>1</sup> A <sub>1</sub> <sup>'</sup>	EOMEA-CCSD	aug-cc-pCVQZ	8073	-711
	EOMEA-CCSDT	aug-cc-pCVTZ	8843	59
	EOMEA-CCSDT	aug-cc-pCVQZ	9001	217
	MRCI [54]	aug-cc-pV5Z	8226	-558
	Experiment	–	8784(80)	–

Table 3.2: Bond Lengths of Be<sub>3</sub> and Be<sub>3</sub><sup>-</sup>

Method	Basis	Bond Length (Å)		
		Be <sub>3</sub> X <sup>1</sup> A <sub>1</sub> <sup>'</sup>	Be <sub>3</sub> <sup>-</sup> X <sup>2</sup> A <sub>2</sub> <sup>''</sup>	Be <sub>3</sub> <sup>-</sup> 1 <sup>2</sup> A <sub>1</sub> <sup>'</sup>
MRCI [54]	aug-cc-pV5Z	2.203	2.106	2.177
CCSD	aug-cc-pCVTZ	2.218	2.129	2.195
CCSD	aug-cc-pCVQZ	2.201	2.116	2.179
CCSDT	aug-cc-pCVDZ	2.247	2.150	2.216
CCSDT	aug-cc-pCVTZ	2.206	2.114	2.180
CCSDT	aug-cc-pCVQZ	2.191	2.102	2.167

Table 3.3: Be<sub>3</sub> and Be<sub>3</sub><sup>-</sup> Harmonic Vibrations

Method	Basis	Be <sub>3</sub> X <sup>1</sup> A <sub>1</sub> <sup>'</sup>		Be <sub>3</sub> <sup>-</sup> X <sup>2</sup> A <sub>2</sub> <sup>''</sup>		Be <sub>3</sub> <sup>-</sup> 1 <sup>2</sup> A <sub>1</sub> <sup>'</sup>	
		A <sub>1</sub> <sup>'</sup>	E <sup>'</sup>	A <sub>1</sub> <sup>'</sup>	E <sup>'</sup>	A <sub>1</sub> <sup>'</sup>	E <sup>'</sup>
CCSDT	aug-cc-pCVDZ	475	409	568	468	514	394
CCSDT	aug-cc-pCVTZ	512	442	580	486	529	408



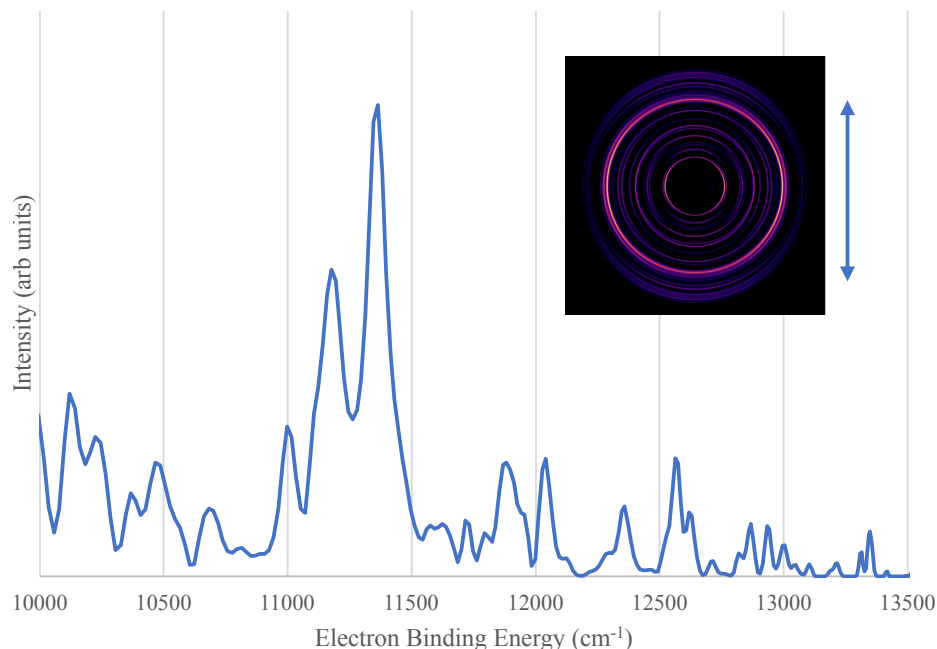


Figure 3.3: Photoelectron spectrum of  $\text{Be}_3^-$  taken with a detachment photon energy of  $13605 \text{ cm}^{-1}$  (vertical polarization shown by double sided blue arrow). Inset photo shows the velocity map image produced by MEVELER software.

Predictions using the EOMEA-CCSDT method and the aug-cc-pcVTZ basis set were found to provide a better treatment of these transitions than any other method tested when comparing the experimentally determined transition energies to the computational predictions. Interestingly the EOMEA-CCSDT calculations both overestimate the EA of this molecule, with the aug-cc-pcVQZ computation overestimating slightly more than the aug-cc-pcVTZ computation. This may imply that, even with the aug-cc-pcVTZ basis set, the neutral is already almost converged to the CCSDT complete basis limit, while the anion has not reached this limit. The energy of the anion then shifts further down relative to that of the neutral molecule when the basis set is increased from VTZ to VQZ. More accurate predictions would require a method that accounts for higher order correlation effects like CCSDTQ. As can be seen from the comparison with EOMEA-CCSD, the role of triple excitations is very important to this system, leading to EOMEA-CCSD under-converging the anion states substantially and leading to an EA value approximately  $1000 \text{ cm}^{-1}$  below the experimental

value (not including zero-point energy contributions). It does however appear that EOMEA-CCSD is sufficient to determine the geometry of this molecule, with the bond length being the same within  $\sim 0.02$  Å as compared to EOMEA-CCSDT and MRCI. The previously published MRCI/aug-cc-pV5Z results [54] also agree well with the EOMEA-CCSDT geometries and come close to the experimental values, differing by about  $230 \text{ cm}^{-1}$  when considering the EA. It is possible that a core-valence correlated basis set would tip the scales in favor of the MRCI method for this molecule, as computations of Be-containing molecules often require the inclusion of core-core and core-valence correlation to be accurately computed, and this phenomenon has been predicted to be substantial for pure Be clusters like  $\text{Be}_3$  as well.

The  $\text{Be}_3^- 1^2A'_1 \rightarrow \text{Be}_3 X^1A'_1$  and  $\text{Be}_3^- X^2A''_2 \rightarrow \text{Be}_3 X^1A'_1$  transitions were observed to have comparable intensities (c.f. Figure 3.1) under jet cooling conditions, where the  $X^2A''_2$  state would be expected to have a greater population than the  $1^2A'_1$  state. The comparable intensities suggest that the threshold photodetachment cross section for the  $\text{Be}_3^- 1^2A'_1 \rightarrow \text{Be}_3 X^1A'_1$  transition is greater than that for  $\text{Be}_3^- X^2A''_2 \rightarrow \text{Be}_3 X^1A'_1$ . This difference in cross sections is consistent with what may be expected based on the results from computational geometry optimizations.

The relevant bond lengths are shown in Table 3.2, and the CCSDT (neutral) and EOM-CCSDT (anion) potential energy curves for the symmetric stretch using an aug-cc-pCVTZ basis set are shown in Figure 3.5. The bond length and shape of the potential curve of the  $\text{Be}_3^- 1^2A'_1$  state is nearly identical to that of the  $\text{Be}_3 X^1A'_1$  state, in contrast to the shorter equilibrium bond length and slightly steeper curvature of the  $\text{Be}_3^- X^2A''_2$  potential energy function. As such, the near vertical Franck-Condon profile of the  $\text{Be}_3^- 1^2A'_1 \rightarrow \text{Be}_3 X^1A'_1$  transition may partially account for the higher-than-expected intensity for transitions originating from the anion excited state, as compared to the smaller, less vertical Franck-Condon profile of the  $\text{Be}_3^- X^2A''_2 \rightarrow \text{Be}_3 X^1A'_1$  transition. Surprisingly, neither the survey spectrum (Figure 3.1)

nor the higher-resolution spectrum (Figure 3.3) showed an obvious progression in the totally symmetrical stretch, although an observable progression was predicted by a Franck-Condon simulation based on the symmetric stretch potential energy curves (see Figure 3.4). It is possible that the small peaks at energies above the EA transition were produced by excited vibrational levels in the neutral ground state, but they were not repeatable enough in our study to warrant assignment.

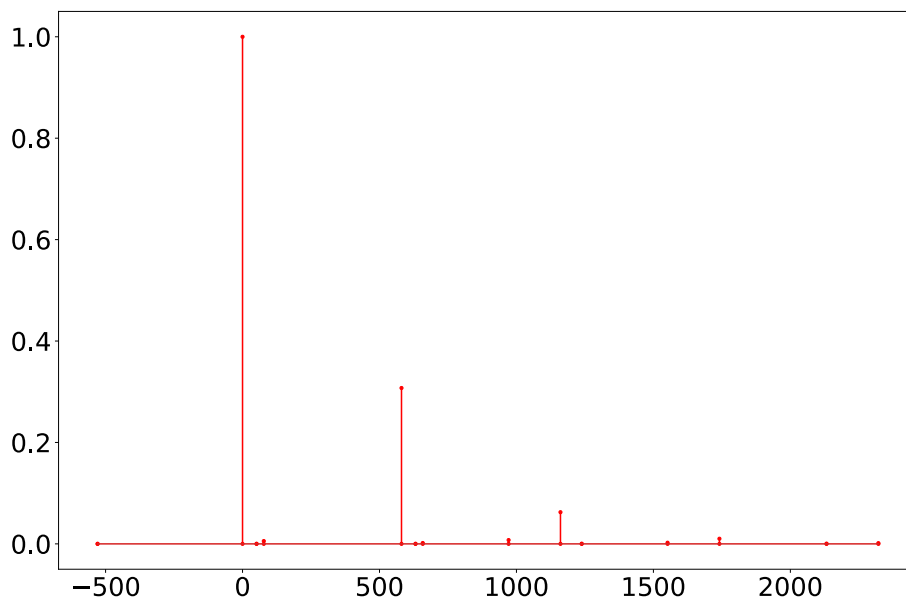


Figure 3.4: A Franck-Condon simulation for the  $\text{Be}_3$  EA transition at 100K. X axis is given in  $\text{cm}^{-1}$  with the 0-0 transition at zero, and intensity is normalized to 1.

Our ability to consistently image the transition originating from the  $\text{Be}_3^- 1^2A'_1$  state suggests that this state has a lifetime of 100  $\mu\text{s}$  or more, based on the time it takes for an anion to reach the position where photodetachment occurs in our apparatus. This is substantially longer than may be expected considering that decay to the anion ground state is (by symmetry) allowed by the electric dipole moment. To determine if this long-lived excited state hypothesis was physically reasonable, the oscillator strength was calculated at the EOMEE-CCSD (EOMEE-equations of motion excitation energy) level with an aug-cc-pCVTZ basis set for the  $\text{Be}_3^- 1^2A'_1 \rightarrow \text{Be}_3^- X^2A''_2$  transition. The oscillator strength was found to be approximately  $7.4 \times$

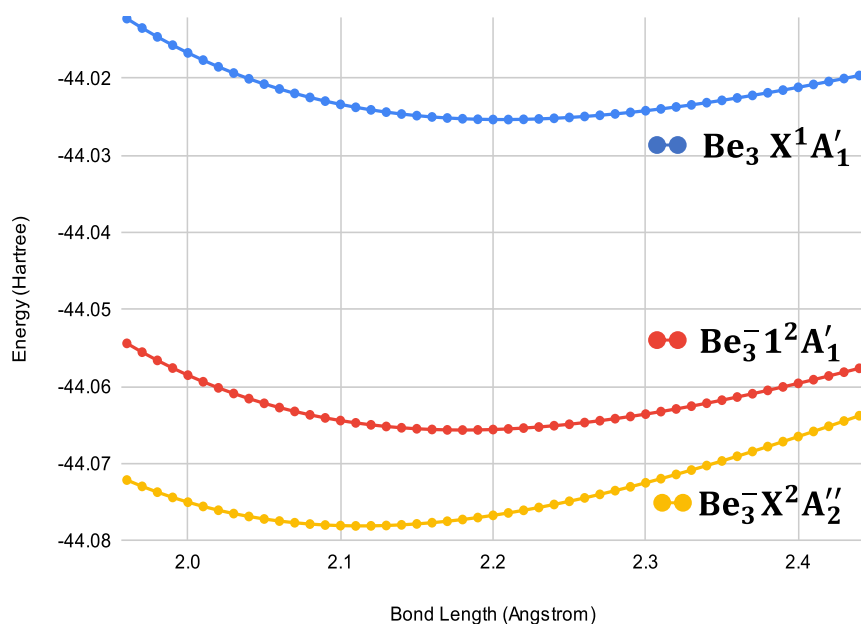


Figure 3.5: Potential energy curves for the  $\text{Be}_3$  anion and neutral molecule between  $1.95\text{\AA}$  and  $2.44\text{\AA}$ , computed in  $0.01\text{\AA}$  steps along the symmetric stretch. The neutral ground state was computed using CCSDT and the anion states were computed using EOMEA-CCSDT. All computations were performed in CFOUR using an aug-cc-pCVTZ basis set.

$10^{-5}$ , consistent with an Einstein A coefficient of  $330\text{ s}^{-1}$  and a radiative lifetime of  $3024\ \mu\text{s}$  when using the experimentally determined energy gap, or an Einstein A coefficient of  $2320\text{ s}^{-1}$  and lifetime of  $431\ \mu\text{s}$  when using the energy gap from the calculation that provided the oscillator strength. In either case, this lifetime is substantially longer than the  $\sim 100\ \mu\text{s}$  flight time in our experiment and longer than the lifetime of any other anion excited state that has a dipole allowed transition to the ground state that we have been able to find in the literature. This long lifetime can be partially explained by looking at the shapes of the  $1^2A'_1$  and  $X^2A''_2$  potential energy curves with respect to bond length as seen in Figure 3.5. The excited  $1^2A'_1$  anion state has substantially different curvature at the bottom of the well as compared to the ground  $X^2A''_2$  anion state, which likely leads to a lower vibrational wavefunction overlap. The inability to relax from the  $\text{Be}_3^- 1^2A'_1$  excited state within

the time of our experiment, as well as the strong vibrational wave function overlap with the neutral ground state, leads to the  $\text{Be}_3^- 1^2A'_1 \rightarrow \text{Be}_3X^1A'_1$  transition showing substantial intensity in all spectra we have taken of this anion.

Higher energy photoelectron spectra for  $\text{Be}_3^-$  were recorded by using 355nm photodetachment, as shown in Figure 3.6 . These wavelengths provided observation windows for states with internal energies of up to  $16800 \text{ cm}^{-1}$ . These energies are well above most computational predictions of the triplet excited state energies[54]. In  $\text{Be}_3$ , weak transitions were observed in the energy range beginning approximately  $6140 \text{ cm}^{-1}$  above the ground state zero-point level but without strong enough repeatable features to be reliably assigned. We believe this is due to the predicted Jahn-Teller distortion of the  $\text{Be}_3$  geometry in its first excited triplet state (reducing the symmetry to  $C_{2v}$ ), which lowers the wavefunction overlap to these excited states and prevents adequate intensity to assign these features when combined with the already weak signal from  $\text{Be}_3^-$ .

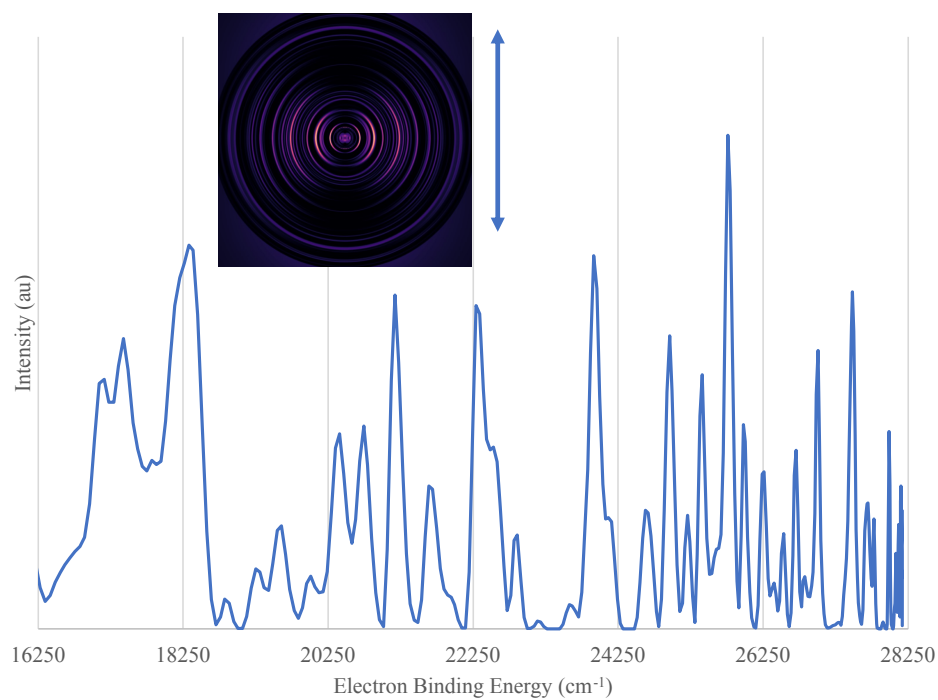


Figure 3.6: Photoelectron spectrum of  $\text{Be}_3^-$  taken with a detachment photon energy of  $28169 \text{ cm}^{-1}$  (vertical polarization shown by double sided blue arrow). Inset photo shows the velocity map image produced by MEVELER software.

## Chapter 4

# Almost an Atom: The Beryllium Tetramer and its Anion

Portions of this section have been reprinted or adapted from Ref [50]:

Noah B. Jaffe, John F. Stanton, and Michael C. Heaven.

Photoelectron Velocity Map Imaging Spectroscopy of the Beryllium Trimer and  
Tetramer

The Journal of Physical Chemistry Letters 2023 14 (37), 8339-8344

DOI: 10.1021/acs.jpcllett.3c02169

Computational studies of small beryllium clusters ( $\text{Be}_n$ ) predict dramatic, non-monotonic changes in the bonding mechanisms and per-atom cohesion energies with increasing  $n$ . To date, experimental tests of these quantum chemistry models are lacking for all but the  $\text{Be}_2$  molecule. In the following section we report spectroscopic data for  $\text{Be}_4$  obtained via anion photodetachment spectroscopy. The tetramer is predicted to have  $T_d$  symmetric equilibrium structures for both the neutral molecule and the anion. Photodetachment spectra reveal transitions that originate from the  $X^2A_1$  ground state. The electron affinity of  $\text{Be}_4$  was determined to be  $13052(50) \text{ cm}^{-1}$ .



## 4.1 Introduction

Small beryllium clusters have long been a topic of theoretical study, with a specific focus toward the clusters below  $n=6$  [4–6, 8, 9, 11, 12, 17, 51–53]. The changes in bonding strength and character in this range are predicted to be dramatic as the size of the cluster increases. The  $\text{Be}_2$  and  $\text{Be}_3$  clusters are both unbound at the Hartree-Fock self consistent field (SCF) level of theory [2, 53].  $\text{Be}_4$  is the first pure Be cluster to be bound at the SCF level of theory [65, 66]. Experimentally, the Be dimer has been found to have a formal bond order of zero and a  $D_e$  of  $934.9\text{cm}^{-1}$  [1, 19]. This dissociation energy is much larger than that of a simple van der Waals interaction between small atoms, and the  $2.444\text{\AA}$  bond length in the dimer also suggests a reasonably strong interaction. High level electronic structure studies predict that the energy needed to remove one Be atom from a  $\text{Be}_n$  cluster has non-monotonic dependence on  $n$ , with  $\text{Be}_4$  representing a local maximum one atom removal energy of  $22400\text{cm}^{-1}$ , substantially higher than that of  $\text{Be}_3$  ( $8470\text{cm}^{-1}$ ) and  $\text{Be}_5$  ( $13830\text{cm}^{-1}$ ) [67]. This result is present in both *ab initio* and DFT methods [6, 8, 9, 11, 17]. A Jellium model that predicts a super-atom closed-shell configuration for  $\text{Be}_4$  has been invoked to explain its high dissociation energy compared to the  $\text{Be}_3$  and  $\text{Be}_5$  clusters [8, 9, 51, 68].

Previous spectroscopic studies on the  $\text{Be}_n$  clusters have only been presented for the  $\text{Be}_2$  neutral and cation [1, 19]. While our lab has previously attempted to use laser excitation techniques to study the electronic structure of  $n \geq 3$  clusters, these attempts proved fruitless. A previous photoelectron study on  $\text{Mg}_n$  clusters [55] was successful in forming the  $n=3-35$  clusters, which has lead us to attempt a similar study on the  $\text{Be}_n$  anions. In the Mg study and others of its kind, the electron affinity (EA) and gap between the EA transition and onset of features due to electronic excitations in the neutral molecule were measured. This energy gap was interpreted as an indication of the HOMO-LUMO gap within a Koopman’s model approximation, and the closing of

this gap was equated with the onset of bulk metallic character. A previous study also reported mass spectra containing  $\text{Be}_n^-$  clusters from  $n=2-6$  [56], lending feasibility to an anion based study of the  $\text{Be}_n$  clusters. A number of theoretical studies of the smaller  $\text{Be}_n$  anions have also been reported [51, 52, 54, 57, 66]. A previous study predicted the EA of  $\text{Be}_4$  to be  $13530\text{cm}^{-1}$  [66]. Given this history, we have decided to use slow electron velocity map imaging (SEVI) spectroscopy to study the beryllium tetramer anion.

## 4.2 Experimental Procedure

An in depth description of the experimental apparatus can be found in Chapter 2. The details specific to  $\text{Be}_4$  and a brief overview are found here. Pulsed laser ablation of a pure beryllium rod in argon backing gas using the focused fundamental output of an Nd:YAG laser (1064nm, 40mj/pulse) was able to produce workable signal for imaging in our apparatus. It was found that adding a small amount (1-5%) of  $\text{N}_2$  to the argon backing gas provided a good third body collider in the supersonic expansion process, and assisted in stabilizing signal as well as cooling the anions more effectively. Gas pulses were produced using an Even-Lavie type valve with a backing pressure of approximately 1000PSI. The supersonic expansion was directed into our WM-TOFMS where all anions were directed down the TOF axis. As the anions travel, they are mass separated in time, and pass over a series of steering optics and Einzel lens. The steering optics serve to condition the beam and ensure it is traveling as on axis to the VMI optics as possible, and the Einzel lens focuses the anions into the photodetachment region in the final chamber. As the anions leave the second chamber, they pass over a mass gate which rapidly turns off as the anion of interest passes over it, allowing it to pass into the final chamber. The final chamber contains the VMI optics, where the electrons are photodetached from

the anions using a vertically polarized photodetachment laser. These experiments used a photodetachment wavelength of 550nm for the survey conditions, produced using an Nd:YAG 2nd harmonic pumped dye laser with a wavelength of 550nm. High resolution images were recorded using a pulsed dye laser with a wavelength of 705nm, and dye laser wavelengths were confirmed using a Bristol Wavemeter. These photodetached electrons were then focused onto our chevron stacked MCPs, which in turn light up a phosphor screen that is recorded by a CCD camera. The CCD camera output is fed to the lab computer, which runs our in-house accumulation software to discriminate high signal shots from low signal shots based on the voltage output of a photomultiplier tube (PMT) that also views the phosphor screen, as described in Section 2.7.1. Approximately 20% of all shots were kept in the final images for  $\text{Be}_4^-$ . Images were pre-processed using custom written python software described in Section 2.7.2, and processed using MEVELER [45]. Image reconstructions were produced in python using the output of the MEVELER software. Calibrations of the spectra were performed using known transitions of the  $\text{S}^-$  anion as described in Section 2.8. Signal for  $\text{Be}_4^-$  was notably strong, especially compared to other pure  $\text{Be}_n^-$  clusters, which may point to the stability of the neutral molecule and its ability to form during ablation.

### 4.3 Results and Discussion

Figure 4.1 shows the survey photoelectron spectrum for  $\text{Be}_4^-$  with inset velocity map image. A linearly polarized Nd:YAG 2<sup>nd</sup> harmonic pumped dye laser (550nm) was used for photodetachment, and the double headed arrow shows the polarization vector. The electron binding energy (eBE) is given as the difference between the photon energy and kinetic energy of the photodetached electron (eKE). Figure 4.1 is entirely dominated by a single feature with strong parallel anisotropy. Using SEVI,

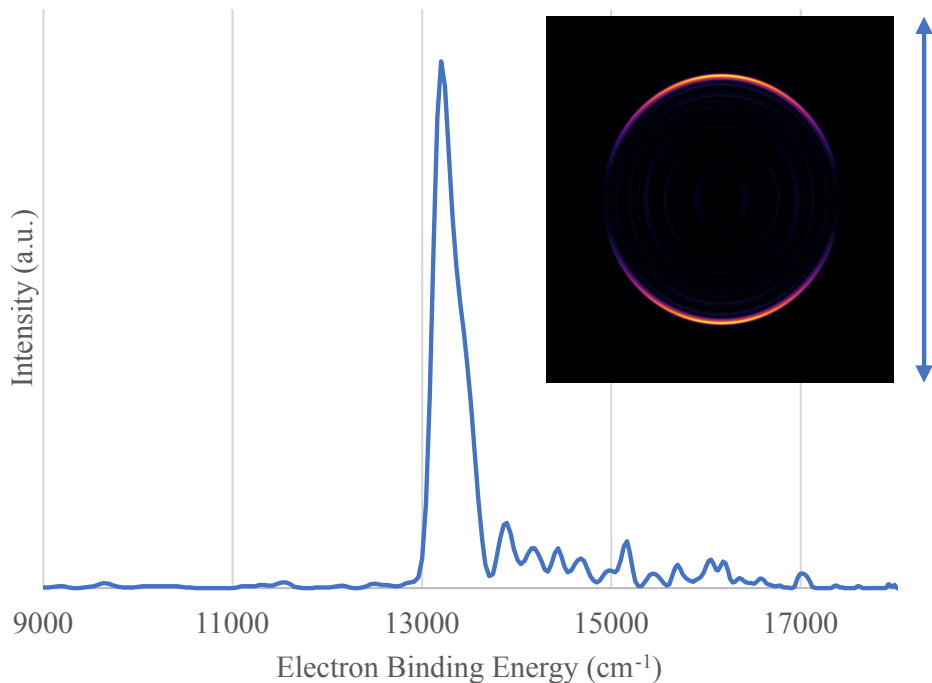


Figure 4.1: Photoelectron spectrum of  $\text{Be}_4^-$  taken with a detachment photon energy of  $18182\text{cm}^{-1}$  (550nm). Inset photo shows the velocity map image produced by MEVELER software, and laser polarization is given by the double headed arrow

we can reduce the extractor voltages on our VMI plates and use a photon energy much closer to the photodetachment threshold in order to improve the image resolution [33]. The higher resolution image shown in Figure 4.2 was obtained using a detachment energy of  $13800\text{cm}^{-1}$  and shows a similarly strong feature, with somewhat diminished anisotropy that is likely due to the lower eKE of the electrons at this lower photodetachment energy, and yields an EA value of  $13052(60)\text{cm}^{-1}$ .

The dominance of a single feature in the spectra is consistent with what may be expected from both existing computation in the literature [66] and our own coupled cluster computations, shown in Table 4.1. Diaz et al [66] computed the equilibrium geometries of  $\text{Be}_4$  and  $\text{Be}_4^-$  at the RMP2 and ROMP2 levels respectively using an aug-cc-pVQZ basis and found a difference of only  $0.02\text{\AA}$  on addition of the electron. Our own computations show an even more minimal change, with the CCSD equilibrium bond length varying by less than  $0.015\text{\AA}$  and the CCSD(T) equilibrium bond length

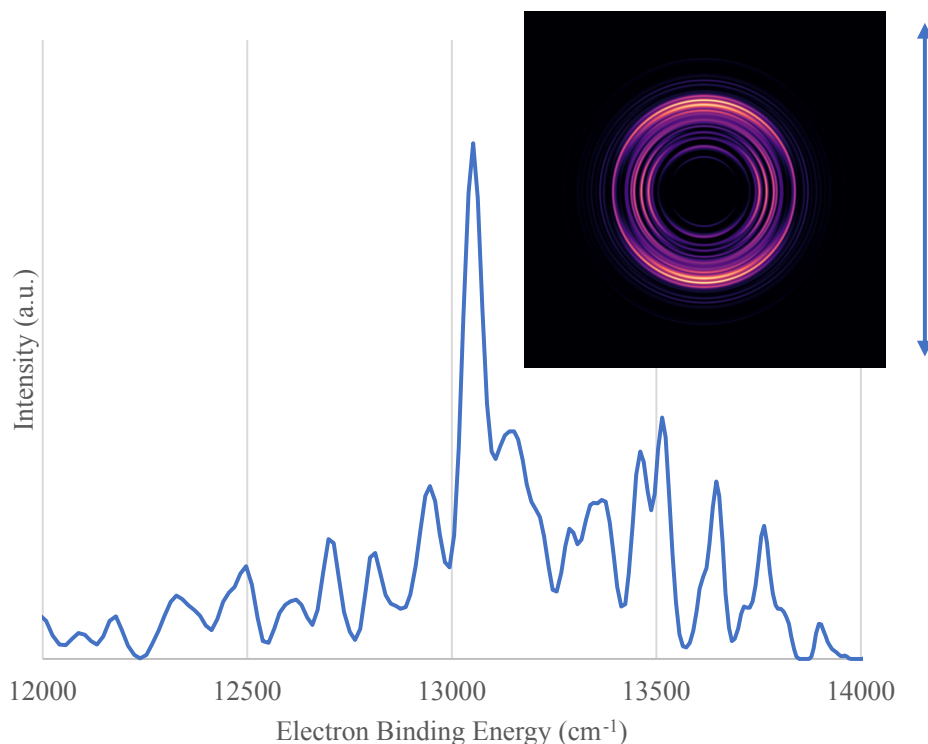


Figure 4.2: Photoelectron spectrum of  $\text{Be}_4^-$  taken with a detachment photon energy of  $14184\text{cm}^{-1}$  ( $705\text{nm}$ ). Inset photo shows the velocity map image produced by MEVELER software, and laser polarization is given by the double headed arrow

varying by less than  $0.005\text{\AA}$  when using an aug-cc-pVTZ basis set. The computed harmonic vibrational frequencies, shown in Table 4.2, tell a similar story. While the non-symmetric modes have slightly lower frequencies upon the addition of an electron, the totally symmetric  $a_1$  mode harmonic frequency is virtually unchanged at the CCSD(T)/aug-cc-pVTZ level, differing by only  $3\text{ cm}^{-1}$ .

$\text{Be}_4$  has a closed shell  $X^1A_1$  ground state, and the excess electron on  $\text{Be}_4^-$  sits in an orbital of  $A_1$  symmetry leading to an anion ground state configuration of  $X^2A_1$ . The electron containing orbital is well described as the in-phase linear combination of sp hybrids which point to the center of the tetrahedron [66], and appears to be a non-bonding orbital. This description is in qualitative agreement with the dominant single peak in Figures 4.1 and 4.2, as well as the anisotropy present in these images. Additionally, the predicted EA values from Diaz [66] of  $13534\text{cm}^{-1}$  for the vertical and

adiabatic EA ( $482\text{cm}^{-1}$  above the experimental value) and our own CCSD(T) aug-cc-pVTZ study of  $12718\text{cm}^{-1}$  ( $334\text{cm}^{-1}$  below the experimental value) are in reasonably good quantitative agreement with the EA obtained from our high resolution image of  $13052(50)\text{cm}^{-1}$ .

The bonding character of  $\text{Be}_4$  has been previously studied[53] by means of Bader's atoms in molecules (AIM) analysis [71] on SCF and MP2 wavefunctions. We performed similar AIM analysis, as well as electron localization function (ELF) analysis [72, 73] using Multiwfn[69, 70] on CCSD wavefunctions for the tetramer. The AIM method determines for the location of bonds by critical points defined by areas where the where  $\nabla^2\rho$  is zero. The method then further separates all of these critical points based on the rank of the Hessian of  $\rho$  (represented by  $\omega$ ) and the sum of the sign of the eigenvalues (represented by  $\sigma$ ). There are then four possible  $(\omega,\sigma)$ : (3,-3), (3,-1), (3,1), and (3,3). (3,-3) is considered by Bader to be an atom, as this corresponds to a local maximum of  $\rho$  in all directions [71]. In Bader's original paper, he states  $\rho$  can only be a local maximum in three dimensions at a nucleus [71], and as such the (3,3) critical point is named the nuclear critical point (NCP). A (3,-1) is a second order saddle point where  $\rho$  is at a local maximum that occurs between two attractive NCPs and signifies a bond within the QTAIM analysis, these (3,-1) points are known as bond critical points (BCPs). There have also been several reported cases of (3,-3) critical points occurring at locations other than nuclei, which are deemed non nuclear attractors (NNA)[74-76] and are not very well understood in terms of their physical relevance. The ELF plots along with the  $\text{Be}_4$  AIM critical point analysis are shown in Figure 4.3. The previous paper [53] suggested that higher level theory description may show  $\text{Be}_4$  as four Be atoms bound to a singular non-nuclear attractor (NNA), but our AIM analysis reveals the same topography as the previous study. Each pair of Be atoms bonds through a NNA and two bond critical points (BCPs), with the NNAs forming an octahedron inside the  $\text{Be}_4$  tetrahedron, where each octahedron point is

centered roughly on a Be-Be bond. There is then a cage critical point (CCP) at the center of the  $\text{Be}_4$  tetrahedron, as well as an additional CCP in each corner of the tetrahedron for a total 5 CCPs. Additionally there are a total of twenty ring critical points (RCPs) of three different types, one type from the Be-NNA-NNA rings, one type from the NNA-NNA-NNA rings on a face of the tetrahedron, and one type from NNA-NNA-NNA rings inside the tetrahedron. This leads to a remarkably even polarization of electron density throughout the tetrahedron. The ELF analysis shows very slight changes in electron density through the center of the tetrahedron, but incredibly uniform and shell like density generally.

Interestingly, the excess electron in the anion seems to slightly change the bonding motif if not the bonding strength. The ELF and BCP plot of the anion is shown in 4.4. The anion shows no CCP, and an NNA ring formed in the center of the dimer bisecting plane. Each Be then bonds to the NNA ring in the center of the tetrahedron. It is possible that this represents an instability in the topology, as was previously suggested for the neutral molecule [53], and in reality this is closer to a singular NNA that all the Be atoms bond to. The ELF plot agrees reasonably with this hypothesis, as there now appears to be a slight increase of density at the center of the tetrahedron, and a general spread of the electron density into a more spherical distribution outside of the molecule as compared to the neutral.

Table 4.1:  $\text{Be}_4$  and  $\text{Be}_4^-$  Equilibrium Bond Lengths

Method	Basis	$\text{Be}_4$ $r_e$ (Å)	$\text{Be}_4^-$ $r_e$ (Å)
CCSD	aug-cc-pVTZ	2.036	2.049
CCSD(T)	aug-cc-pVTZ	2.046	2.042
RMP2/ROMP2 [66]	aug-cc-pVQZ	2.06	2.04

Additional high energy photoelectron images for  $\text{Be}_4^-$  were recorded using 25189  $\text{cm}^{-1}$  (397nm) detachment photons and an example is shown in Figure 4.5. This de-

Table 4.2: Be<sub>4</sub> and Be<sub>4</sub><sup>-</sup> Harmonic Frequencies

		Be <sub>4</sub> ω (cm <sup>-1</sup> )	Be <sub>4</sub> <sup>-</sup> ω (cm <sup>-1</sup> )
CCSD(T)	aug-cc-pVTZ	a <sub>1</sub>	721
		e	456
		t <sub>2</sub>	576

tachment energy provides an additional 12264 cm<sup>-1</sup> of internal energy to the tetramer, which is above most computational predictions for the first excited triplet state energy [8, 9, 11, 12, 16]. This triplet state in Be<sub>4</sub> is predicted to experience a Jahn-Teller distortion, which lowers its symmetry to either D<sub>2d</sub> or C<sub>2v</sub> depending on the exact method of computation. In our high energy spectra we found a reasonable amount of activity in the energy range 7950-11000cm<sup>-1</sup> above the Be<sub>4</sub> origin (eBE from 21000-25000 cm<sup>-1</sup>). While this is in qualitative agreement with the expected singlet-triplet gap in the tetramer, large amounts of spectral congestion due to the assumed Jahn-Teller splitting of the triplet has restricted our ability to make definitive assignments of these peaks.



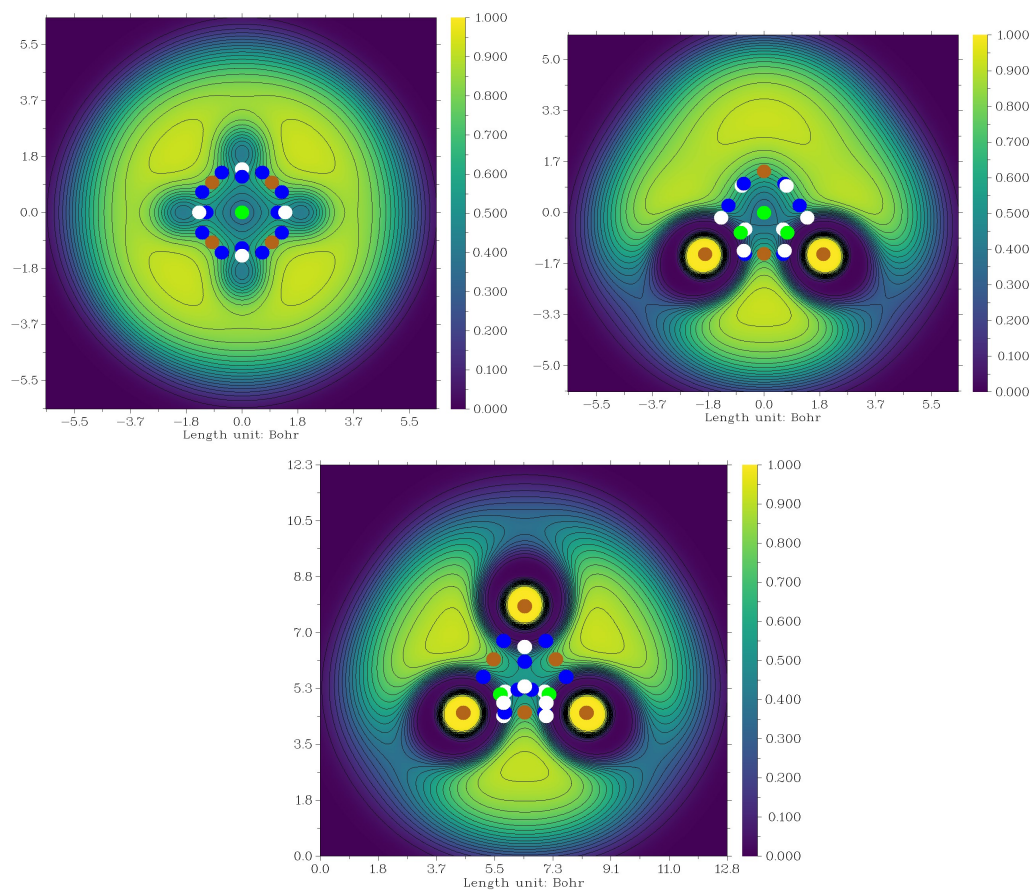


Figure 4.3: ELF contour maps along the plane of the  $\text{Be}_4$   $^1A_1$  molecule through the center of the tetrahedron bisecting it into two Be dimers (top left), the plane through two Be atom bisecting the tetrahedron (top right), and the plane through three Be atoms forming a face of the tetrahedron (bottom). (3,-3) non-nuclear attractor (NNA) and nuclear critical points are shown as brown dots, (3,-1) bond critical points (BCP) critical points in blue, (3,1) ring critical points (RCPs) in white, and (3,3) cage critical points (CCPs) in green. Image and analysis performed using Multiwfn [69, 70]

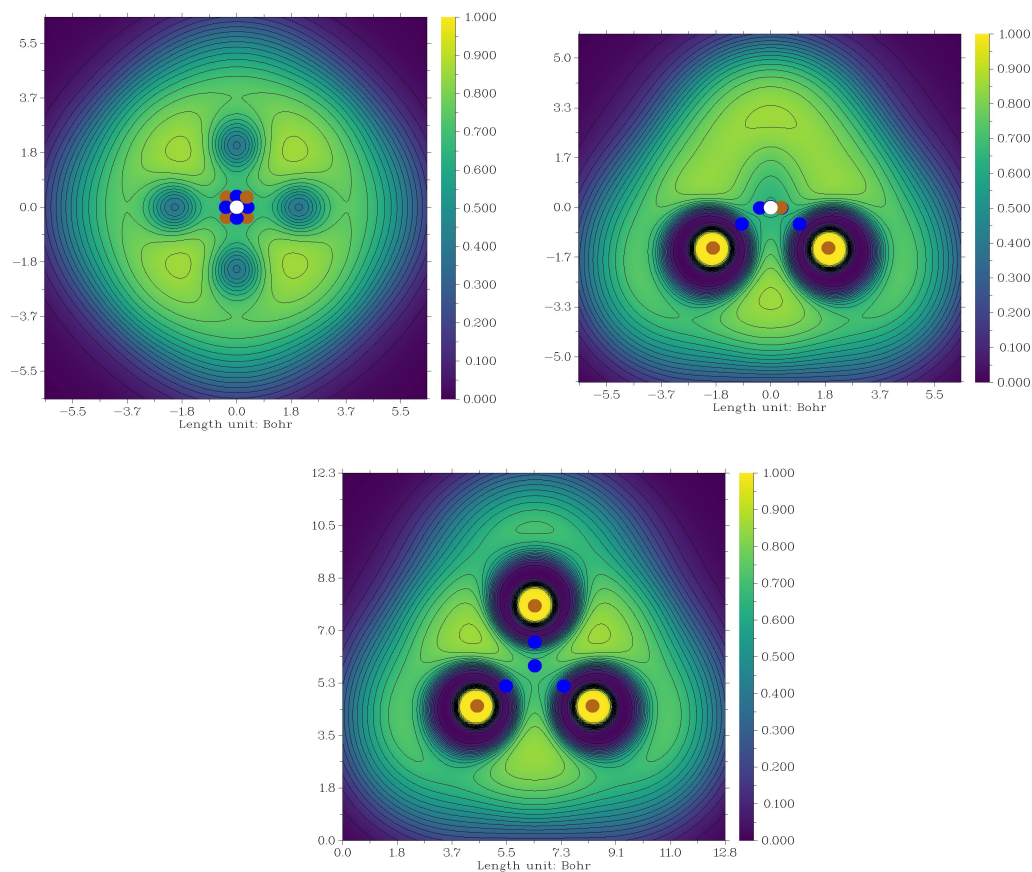


Figure 4.4: ELF contour maps along the plane of the  $\text{Be}_4 \ ^2A_1$  anion through the center of the tetrahedron bisecting it into two Be dimers (top left), the plane through two Be atom bisecting the tetrahedron (top right), and the plane through three Be atoms forming a face of the tetrahedron (bottom). (3,-3) non-nuclear attractor (NNA) and nuclear critical points are shown as brown dots, (3,-1) bond critical points (BCP) critical points in blue, and (3,1) ring critical points (RCPs) in white. (3,3) cage critical points (CCPs) are notably absent. Image and analysis performed using Multiwfn [69, 70]

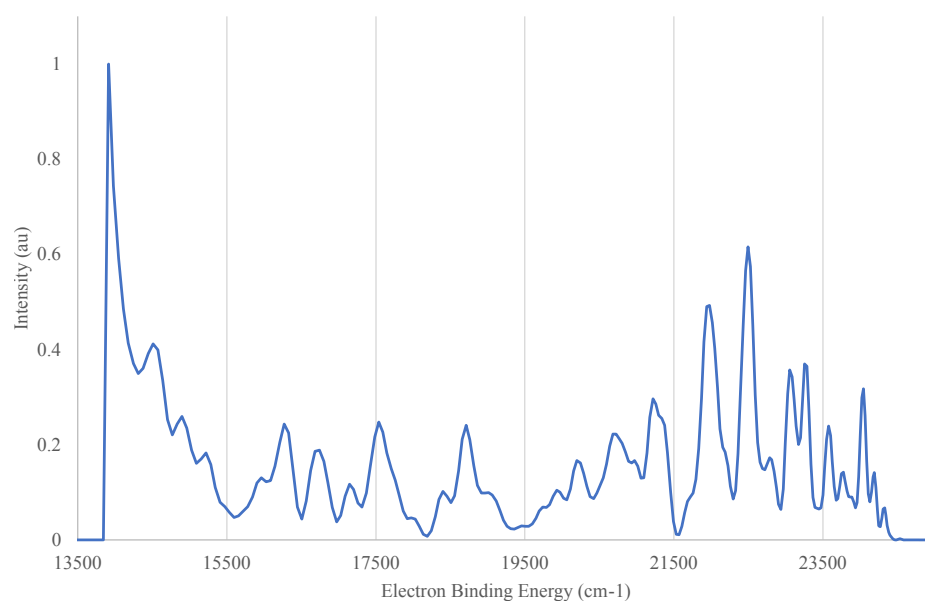


Figure 4.5: Photoelectron spectrum of Be<sup>4-</sup> taken with a detachment photon energy of 25189 cm<sup>-1</sup> (397nm). The sharp cutoff just above 13500 cm<sup>-1</sup> is due to the edge of the detector, and the large peak is due to the electron affinity transition being partially captured.

## Chapter 5

# The Youth Taker: The Beryllium Pentamer and its Anion

Studies of the Be pentamer were assisted by Dr John Stanton

“A proper - exhaustive treatment of all of these states might take the rest  
of your youth away and work well into middle age”

-John Stanton, PhD

(he was right)

Computational studies of small beryllium clusters ( $\text{Be}_n$ ) predict dramatic, non-monotonic changes in the bonding mechanisms and per-atom cohesion energies with increasing  $n$ . To date, experimental tests of these quantum chemistry models are lacking for all but the  $\text{Be}_2$  molecule. In the following section we report spectroscopic data for  $\text{Be}_5$  obtained via anion photodetachment spectroscopy. The Be pentamer is predicted to have a  $D_{3h}$  symmetric equilibrium structure (trigonal bipyramidal) in the neutral ground state and a Jahn-Teller distorted ( $D_{3h} \rightarrow C_{2v}$ ) structure in the anion ground state. Photodetachment spectra reveal transitions that we believe originate from the anion  $X^2A_2$  anion ground state and the  $2^2A_1$  anion electronically excited state. The state symmetries were assigned on the basis of anisotropic photoelectron angular distributions with assistance from high level *ab initio* computation. The adiabatic electron affinity of  $\text{Be}_5$  has been assigned to be  $12109(268) \text{ cm}^{-1}$ , and the  $\text{Be}_5$   $1^3A_2$  electronically excited state was found to be approximately  $3585(351) \text{ cm}^{-1}$  above the ground state. Additionally, the excited  $\text{Be}_5^- 2^2A'_1$  state was observed  $3542(333) \text{ cm}^{-1}$  above the anion ground state.

## 5.1 Background and Introduction

While  $\text{Be}_5$  represents a potential turning point for  $\text{Be}_n$  clusters, it has previously been studied only by computational methods. While the neutral ground state has been reasonably well studied and assigned a trigonal bipyramid  $D_{3h}$  geometry [4, 9, 12, 53, 67, 77], the literature on the anion leaves much to be desired. Additionally, there are rather few predictions of the first excited neutral state, but what predictions do exist show a substantial decrease in singlet-triplet gap from the smaller  $\text{Be}_4$  cluster [16]. Additionally, the predictions on the anion ground state and neutral triplet lack the same amount of consistency as those of the neutral ground state.

Interestingly, from an electron correlation standpoint, the pentamer is most similar to the dimer, experiencing large amounts of static correlation in addition to its dynamic correlation [67]. A common method to determine the static correlation effects in a molecular system treated within the coupled cluster framework is to look at the  $T_1$  diagnostic and the magnitude of the largest  $t_2$  amplitudes. Generally, larger values for these diagnostics point to higher static correlation effects. A CCSD(T) study of  $\text{Be}_n$  clusters using a cc-pCVQZ basis set found that  $\text{Be}_2$ ,  $\text{Be}_4$ , and  $\text{Be}_5$  all had similar  $T_1$  diagnostics, but the largest  $t_2$  amplitudes of  $\text{Be}_5$  ( $t_2 \approx 0.126$ ) were two to four times larger than that of  $\text{Be}_4$  ( $t_2 \approx 0.062$ ), and roughly half that of  $\text{Be}_2$  ( $t_2 \approx 0.225$ ) [67]. The study also found that the per atom bonding energy of  $\text{Be}_5$  was only slightly higher than that of the tetramer, with a binding energy per atom (BEPA) of  $25.9 \text{ kcal mol}^{-1}$  vs the tetramer's BEPA of  $22.4 \text{ kcal mol}^{-1}$ .

A much earlier study of the bonding nature of Be clusters suggested that the bonds of  $\text{Be}_5$  are actually not Be-Be bonds, but instead are all Be atoms bonded to the center of the bipyramid [53]. This type of bonding has previously been invoked as an explanation of metallic character [76]. A study of the neutral and ionic  $\text{Be}_5$  clusters suggested that the bonding in  $\text{Be}_5$  was due to  $sp^3$  hybridization of the equatorial Be atoms, and that the bonds in  $\text{Be}_5$  were of a multi-centered nature [77]. While

this study did present a few isomers of the  $\text{Be}_5$  anion, it was unable to conclusively determine the ground state geometry or symmetry. The study used both DFT and MP2, and found that for both B3LYP and B3PW91 the anion ground state was predicted as a  $\text{C}_{2v}$  distorted trigonal pyramid, but for MP2 the lowest energy isomer was a  $\text{C}_{3v}$  structure resembling the tetramer with an extra Be atom attached to a vertex of the tetrahedron. While they did note that the  $\text{C}_{2v}$  geometry was an  $\text{A}_2$  state with the DFT methods and a  $\text{B}_2$  state using MP2, they did not provide any insight into how these two states were linked.

## 5.2 Experimental Procedure

An in depth description of the experimental apparatus can be found in Chapter 2. The details specific to  $\text{Be}_5$  and a brief overview are found here. Pulsed laser ablation of a pure beryllium rod in argon backing gas using the focused fundamental output of an Nd:YAG laser (1064nm) was able to produce workable signal for imaging in our apparatus. It was found that adding a small amount (1-5%) of  $\text{N}_2$  to the argon backing gas provided a good third body collider in the supersonic expansion process, and assisted in stabilizing signal as well as cooling the anions more effectively. Gas pulses were produced using an Even-Lavie [36] type valve with a backing pressure of approximately 1000PSI. The supersonic expansion was directed into our WM-TOFMS where all anions were directed down the TOF axis. As the anions travel, they are mass separated in time, and pass over a series of steering optics and an Einzel lens. The steering optics serve to condition the beam and ensure it is traveling as on axis to the VMI axis as possible, and the Einzel lens focuses the anions into the photodetachment region in the final chamber. As the anions leave the second chamber, they pass over a mass gate which is rapidly turns off as the anion of interest passes over it, allowing it to pass into the final chamber. The final chamber contains the VMI optics,

where the electrons are photodetached from the anions using a vertically polarized photodetachment laser. These experiments used a photodetachment wavelength of 532nm for the survey conditions, produced using the second harmonic of an Nd:YAG laser. Longer wavelengths were generated with a Nd:YAG 2nd harmonic pumped dye laser or OPO, and wavelengths were confirmed using a Bristol Wavemeter. These photodetached electrons are then focused onto our chevron stacked MCPs, which in turn light up a phosphor screen that is recorded by a CCD camera. The CCD camera output is fed to the lab computer, which discriminates high signal shots from low signal shots based on the voltage output of a photomultiplier tube (PMT) that also views the phosphor screen, as described in Section 2.7.1. Photodetachment efficiency for  $\text{Be}_5^-$  images ranged from 0.5% to 30% depending on the state of interest. Images were pre-processed using custom written python software described in Section 2.7.2, and processed using MEVELER [45]. Image reconstructions were produced in python using the output of the MEVELER software. Calibrations of the spectra were performed using known transitions of the  $\text{S}^-$  anion as described in Section 2.8. All uncertainties given are  $2\sigma$  values and are determined by propagating the uncertainty in pixel space to energy space, unless otherwise noted.

### 5.3 Computational Results

Computational predictions of the pentamer have pointed to a  $\text{D}_{3h}$  trigonal bipyramidal ground state geometry for the neutral molecule and a distorted trigonal bipyramidal  $\text{C}_{2v}$  geometry in the anion, described as a shift of the axial Be atoms at the top and bottom of the bipyramid away from one of the equatorial Be atoms, and a distortion of the equilateral triangle that is formed by the equatorial Be atoms[4, 8, 9, 67]. Several bond length predictions for the neutral cluster's ground state are presented in Table 5.1. Because the anion is rather distorted, the anion ground state



geometry is given as the set of Z-Matrix coordinates to build the molecule in Table 5.3. The associated Z matrix is given in Table 5.2, where BE are beryllium atoms and X is a dummy atom to simplify construction.

Table 5.1: Be<sub>5</sub> Computational Geometry Predictions

Method	Basis	Reference	$r_{eq-eq}$	$r_{eq-ax}$
MP2 <sup>(FC)</sup>	cc-pVQZ	Ascik et al. [67]	2.0137	2.0697
CCSD <sup>(FC)</sup>	cc-pVQZ	Ascik et al. [67]	2.0096	2.0602
CCSD(T) <sup>(FC)</sup>	cc-pVQZ	Ascik et al. [67]	2.0129	2.0752
CCSD	cc-pCVQZ	Ascik et al. [67]	1.9969	2.0460
CCSD(T)	cc-pCVQZ	Ascik et al. [67]	2.0000	2.0604
CCSD(T)	aug-cc-pCVTZ	This work	2.02	2.08
CCSDT	aug-cc-pCVTZ	This work	2.011	2.068
B3LYP	aug-cc-pVTZ	This work	2.01	2.07

<sup>(FC)</sup> Denotes a frozen core computation

$r_{eq-eq}$  is the bond length for an equatorial Be-Be bond

$r_{eq-ax}$  is the bond length for an equatorial Be to axial Be bond

Table 5.2: Be<sub>5</sub> Z-Matrix

X						
BE	1	R1				
BE	1	R12	2	T120		
BE	1	R12	2	T120	3	T180
BE	1	R2	2	T90	3	T901
BE	1	R2	2	T90	3	M90

To better understand the level of multireference character in the pentamer, we performed CASSCF computations with an aug-cc-pCVTZ basis. These computations predicted approximately two thirds of the total wavefunction was contained in

Table 5.3:  $\text{Be}_5^- X^2 A_2$  Geometry Parameters

Method	EOMEA-CCSD		EOMEA-CCSDT	
	aug-cc-pCVDZ	aug-cc-pCVTZ	aug-cc-pCVDZ	aug-cc-pCVTZ
R1 (Å)	1.275	1.249	1.289	1.272
R12 (Å)	1.22	1.204	1.224	1.201
T120 (°)	109.808	110.254	109.399	109.310
T180 (°)	180	180	180	180
R2 (Å)	1.649	1.627	1.658	1.635
T90 (°)	91.569	91.602	91.457	91.031
T901 (°)	90	90	90	90
M90 (°)	-90	-90	-90	-90

the single reference determinant (leading CI coefficient  $\approx 0.82$ ). The potential multireference problems were also hinted at in our single reference studies, as some SCF algorithms seem to converge to the wrong SCF occupancy for the neutral ground state. Our studies using CFOUR [58] often converged to an  $A_1''$  ground state (with an occupancy of five  $A_1'$  orbitals, two  $A_2'$  orbitals, two  $A_2''$  orbitals, and one  $A_1''$  orbital) unless forced to create the proper  $A_1'$  ground state (with an occupancy of six  $A_1'$  orbitals, two  $A_2'$  orbitals, two  $A_2''$  orbitals, and no  $A_1''$  orbitals). The energy differences of the two wavefunctions at the CCSDT/aug-cc-pCVTZ optimized geometry (geometry given in Table 5.1) is given in Table 5.4. In our studies, both the default wavefunction guess from the SCF procedure and alternative ground state wavefunctions were calculated to ensure that the lowest energy state was found. This process can be assisted using the HFSTABILITY keyword in CFOUR, which will perform a stability analysis on the SCF wavefunction and can assist in finding other low energy SCF solutions. Generally, we found that CCSD with a substantial basis set that includes core-valence correlation was sufficient for determining the geometry of the neutral molecule, and moving to CCSDT only made small changes to the optimized geometry.

Table 5.4: Be<sub>5</sub> Ground State Wavefunction Energies

Method	Basis	Energy of A <sub>1</sub> '' State	Energy of A <sub>1</sub> ' State
SCF	aug-cc-pCVDZ	-72.8854	-72.9363
MP2	aug-cc-pCVDZ	-73.2718	-73.3733
CCSDT	aug-cc-pCVDZ	-73.3407	-73.4206

All computations performed at the CCSDT/aug-cc-pCVTZ Geometry  
Energies given in Hartree

Additionally, keeping with its beryllium heritage, Be<sub>5</sub> exhibits a rather strange bonding motif. One (potentially controversial) method to determine the location of bonds is to look for critical points defined by areas where the where  $\nabla^2\rho$  is zero. This method, originally introduced by Bader [71, 78], then further separates all of these critical points based on the rank of the Hessian of  $\rho$  (represented by  $\omega$ ) and the sum of the sign of the eigenvalues (represented by  $\sigma$ ). There are then four possible  $(\omega,\sigma)$ : (3,-3), (3,-1), (3,1), and (3,3). (3,-3) is considered by Bader to be an atom, as this corresponds to a local maximum of  $\rho$  in all directions [71]. In Bader's original paper, he states  $\rho$  can only be a local maximum in three dimensions at a nucleus [71], and as such the (3,3) critical point is named the nuclear critical point (NCP). A (3,-1) is a second order saddle point where  $\rho$  is at a local maximum that occurs between two attractive NCPs and signifies a bond within the QTAIM analysis, these (3,-1) points are known as bond critical points (BCPs). There have also been several reported cases of (3,-3) critical points occurring at locations other than nuclei, which are deemed non nuclear attractors (NNA)[74–76] and are not very well understood in terms of their physical relevance. Using multiwfn [69, 70] to do both critical point and electron localization function (ELF) analysis [72, 73] we find that the BCP's of Be<sub>5</sub> do not lie between individual atoms, but instead the individual Be atoms all seem to have BCPs that connect to a NNA at the center of the D<sub>3h</sub> cage. These BCPs

are shown along with the ELF contour in Figure 5.1. Because of limitations of most computational software chemistry software including CFOUR it should be noted that  $D_{3h}$  computations are run as  $C_{2v}$ , which is why the ELF plot is not perfectly  $D_{3h}$  symmetric. While there exists some question as to the NNA's and their existence as more than an artifact of the computation, this NNA has appeared in all of our computations for  $Be_5$ , as well as one earlier study using only SCF orbitals [53], and does not appear to change with different basis sets or methods as some in the literature report [74, 76]. Additionally, of the few examples of an experimentally confirmed NNA that do exist, one was in bulk hexagonal close packed (HCP) beryllium studied by xray diffraction [79], which suggested that the HCP structure only contained Be-NNA bonds and NNA-NNA bonds, and no Be-Be bonds as we see in our analysis. Another more recent experimental study showed that these NNA's are also present other alkali earth metals, namely dimeric Mg(1) compounds [80].

Predictions on the anion ground state symmetry and relative energies in the literature are somewhat sparse. A previous study using B3LYP and B3PW91 with a 6-311+G\* basis predicted the ground state to be a  ${}^2A_2$   $C_{2v}$  distorted trigonal bipyramidal geometry, while MP2 predicted this structure to have  ${}^2B_2$  symmetry and predicted a lower energy  $C_{3v}$  structure [51]. In our own studies, we found that the prediction of the anion distorted bipyramid state symmetry varies depending on the combination of method and basis set. Despite this, higher level computations found that the  $C_{3v}$  anion geometries were much higher in energy than the  $C_{2v}$  structures when restricted, and some of these  $C_{3v}$  geometries converged to  $C_{2v}$  geometries when allowed to free-run. A summary of the state energies and symmetries of a few of the anion low lying states can be found in Table 5.5. It appears that this difficulty in prediction occurs because of SCF based computations using correlation consistent basis sets pick the incorrect symmetry due to the Jahn-Teller (JT) effect, and may also be exacerbated by the difficulty in predicting the SCF wavefunction correctly as is

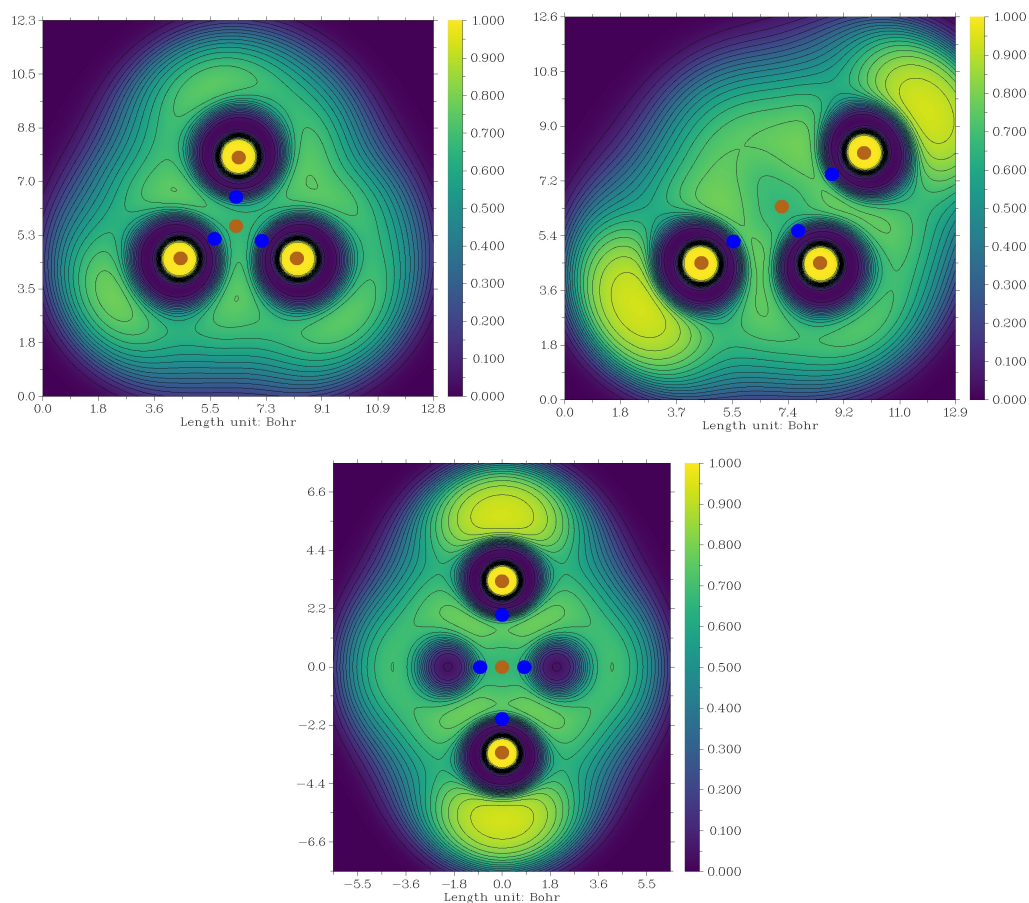


Figure 5.1: ELF contour maps along the plane of the  $\text{Be}_5$   $^1A'_1$  equatorial ring (top left), two axial Be and one equatorial Be (top right), and two axial Be parallel to two equatorial Be (bottom). (3,-3) NNA and NCP critical points are shown as brown dots, while (3,-1) BCP critical points are shown in blue. Image and analysis performed using Multiwfn [69, 70]

the case in the neutral. While this effect also occurred in our own B3LYP/cc-pVTZ computation, the previously reported study using Pople basis sets had the correct symmetry for this geometry [51]. To combat this problem, we have used equations of motion electron attachment coupled cluster (EOMEA-CC) theories in this study. EOMEA-CC methods use the ground state wavefunction of the neutral and perform an electron attachment from this wavefunction into an orbital of specified symmetry [61–63], allowing us to control which part of the JT system we are computing easily. Because the EOM based methods rely on having the correct ground state

wavefunction, it is incredibly important that the stability of the SCF wavefunction is investigated thoroughly. In addition to checking the neutral ground state, the lowest energy anion state of each  $C_{2v}$  symmetry was calculated to ensure the ground state of the anion was properly selected.

Table 5.5:  $\text{Be}_5^-$  Relative Energies

State	Method	Basis	Energy (Hartree)	$\Delta E$ ( $\text{cm}^{-1}$ )
$A_2$ ( $C_{2v}$ )	EOMEA-CCSD	aug-cc-pCVDZ	-73.44037232	0
	EOMEA-CCSD	aug-cc-pCVTZ	-73.51623997	0
	EOMEA-CCSDT	aug-cc-pCVDZ	-73.47680621	0
$B_1$ ( $C_{2v}$ )	EOMEA-CCSD	aug-cc-pCVDZ	-73.43996246	89.95
	EOMEA-CCSD	aug-cc-pCVTZ	-73.51592913	68.22
	EOMEA-CCSDT	aug-cc-PCVDZ	-73.47640602	87.83
$A'_1$ ( $D_{3h}$ )	EOMEA-CCSD	aug-cc-pCVDZ	-73.42244136	3935.42
	EOMEA-CCSD	aug-cc-pCVTZ	-73.49412967	4852.69

$\Delta E$  values given as energy difference between optimized geometries without ZPE

The results of the EOMEA-CCSD and EOMEA-CCSDT computations for the lowest three states are shown in Table 5.5 without zero-point energy (ZPE) corrections. Due to the massive memory and time costs of EOMEA-CCSDT computations using an aug-cc-pCVTZ basis set over an aug-cc-pCVDZ basis (a single iteration of EOMEA-CCSDT takes roughly 30 times as long with the larger basis set, and just the single point EOMEA-CCSDT single point energy takes roughly 145 days of computer time with the aug-cc-pCVTZ basis), EOMEA-CCSDT optimizations were only performed for the ground state of the anion and neutral with the larger basis set. Other states' EOMEA-CCSDT/aug-cc-pCVTZ energies were computed using the EOMEA-CCSDT/aug-cc-pCVDZ geometry, which was found to be similar to the EOMEA-CCSDT/aug-cc-pCVTZ geometry when computed. Interestingly, it was found that the two states of the JT coupled system, namely the  $A_2$  and  $B_1$  anion states, were remarkably close in energy, with an energy gap of approximately  $88 \text{ cm}^{-1}$  at the

EOMEA-CCSDT/aug-cc-pCVDZ level at their respective optimized geometries. In the spirit of overkill, we attempted to compute these states' single point energies at the EOMEA-CCSDTQ/aug-cc-pCVDZ level, but were unable to procure enough memory overhead. Additionally, the predicted linear Jahn-Teller stabilization of the  $A_2$  anion is rather small, with only a  $1015 \text{ cm}^{-1}$  gap at the EOMEA-CCSDT/aug-cc-pCVDZ level when comparing the  $A_2$  optimized  $C_{2v}$  geometry with a  $D_{3h}$  restricted optimized geometry. A table of the JT energy differences at several treatments is shown in Table 5.6. It is worth noting here that as the  $A_2$  state is consistently lower in energy than the  $B_1$  state (if only slightly) we make the assumption that the  $A_2$  state is the lower energy state in our spectra. While we designate transitions as originating from the  $A_2$  state, in reality the  $A_2$  and  $B_1$  states are fundamentally intertwined and the  $A_2$  state will experience pseudorotation through the  $B_1$  state. As such the distinction between the  $A_2$  and  $B_1$  states is one of notation more so than physical reality.

Table 5.6:  $\text{Be}_5^-$  Jahn-Teller Stabilization Energies

Method	Basis	$A_2-B_1$ ( $\text{cm}^{-1}$ )	$A_2-E''$ ( $\text{cm}^{-1}$ )
EOMEA-CCSD	aug-cc-pCVDZ	89.95	1009.5
EOMEA-CCSD	aug-cc-pCVTZ	68.22	998.2
EOMEA-CCSDT	aug-cc-pCVDZ	87.83	1014.3

While the intersection through the  $D_{3h}$  minimum provides a  $1015 \text{ cm}^{-1}$  barrier, the potential surfaces of both the  $A_2$  and  $B_1$  state are extremely flat when not restricted. Potential energy surface calculations along the T90 coordinate (see Table 5.2) at the EOMEA-CCSDT/aug-cc-pCVDZ level from 85 to 94.5 degrees showed constant energy down to  $10^{-8}$  Hartree when the other coordinates were re-optimize at each grid point. An additional set of computations was performed to determine the minimum viable basis size by calculating energies on sample grid over one direction using a jun-cc-pv(D+d)z, a cc-pCVDZ, and an aug-cc-pVDZ basis in addition to the aug-cc-

Table 5.7:  $\text{Be}_5$  and  $\text{Be}_5^-$  Ground State Harmonic Frequencies

State	Neutral $A'_1$	Neutral $A'_1$	Neutral $A'_1$	Anion $A_2$
Method	CCSD(T)	CCSD	CCSD	EOMEA-CCSD
Basis	cc-pCVQZ	aug-cc-pCVDZ	aug-cc-pCVDZ	aug-cc-pCVDZ
Geometry	Neutral $D_{3h}$	Neutral $D_{3h}$	Anion $A_2$	Anion $A_2$
$\downarrow$ mode : $D_{3h}$ ( $C_{2v}$ )				
$\nu_1$ : $a'_1$ ( $a_1$ )	730	758	667	686
$\nu_2$ : $a'_1$ ( $a_1$ )	456	473	335	398
$\nu_3$ : $e'$ ( $a_1$ )	583	604	509	527
$\nu_3$ : $e'$ ( $b_2$ )	583	604	590	560
$\nu_4$ : $e'$ ( $a_1$ )	338	337	169	252
$\nu_4$ : $e'$ ( $b_2$ )	338	337	395	201
$\nu_5$ : $a''_2$ ( $b_1$ )	611	635	335	652
$\nu_6$ : $e''$ ( $a_2$ )	488	467	267	569
$\nu_6$ : $e''$ ( $b_1$ )	488	467	436	425

Energies given in  $\text{cm}^{-1}$

CCSD(T)/cc-pCVQZ values from Ascik et al.[67]

pCVXZ (X=D,T) sets to determine which was more suitable for this computation, and it was found that the cc-PCVDZ basis yielded lower energies at all points than the non core-valence basis sets but all tested basis sets provided qualitatively the same result as the aug-cc-pCVDZ basis results. Using the cc-pCVDZ basis as our minimum viable basis set, three dimensional potential energy surfaces were calculated at the EOMEA-CCSD/cc-pCVDZ level by fixing two coordinates on a grid over the area of interest and allowing the other coordinates to re-optimize at each point. These grids were smoothed by two-dimensional third order polynomial spline interpolation and are shown in Figures 5.2, 5.3, and 5.4. The original, untreated surfaces are shown in Section 5.6, Figures 5.12, 5.13, and 5.14. These potential surfaces show very small barriers between the  $A_2$  and  $B_1$  states, from 200-800  $\text{cm}^{-1}$  depending on the two



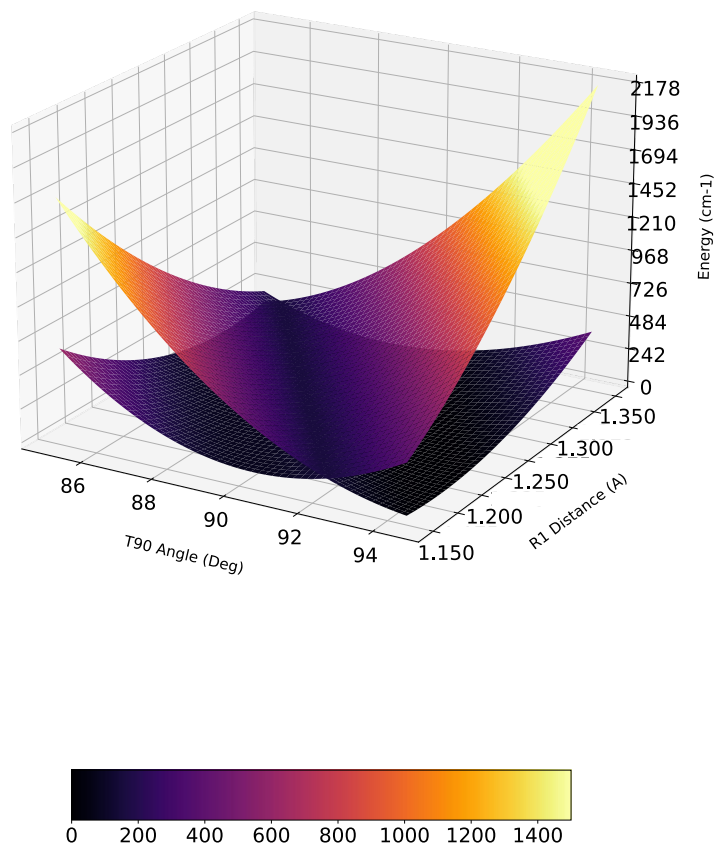


Figure 5.2: Interpolated EOMEA-CCSD/cc-pCVDZ potential energy surfaces across the T90 (deg) and R1 ( $\text{\AA}$ ) coordinates. All other coordinates were optimized at each point in the grid. Color-mapping and Z axis shows the energy in  $\text{cm}^{-1}$ . The  $A_1$  state minimum is on the right side.

coordinates chosen, that are incredibly flat near the potential energy minimum of each respective state. This barrier is well below the zero point energy of the anion in so far as this can be determined by harmonic frequencies of the  $A_2$  state, meaning pseudorotation between the  $A_2$  and  $B_1$  states is incredibly likely. Additionally, hot vibrations in non symmetric modes of  $a_2$  and  $b_1$  symmetry would allow for vibronic coupling between the two states even without JT coupling, and we expect these hot vibrations to be common due to the high temperatures of ablation, so the ground state of the anion likely behaves like a rather unhappy  $E''$  state.

The  $A_2$  anion has a similar bonding motif to the neutral ground state, and also

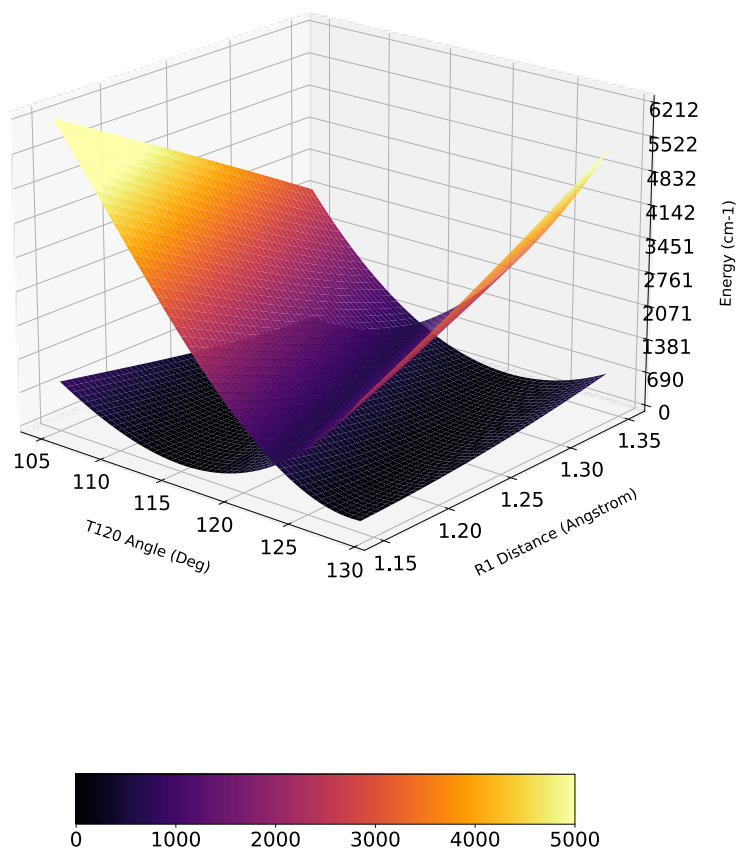


Figure 5.3: Interpolated EOMEA-CCSD/cc-pCVDZ potential energy surfaces across the T120 (deg) and R1 ( $\text{\AA}$ ) coordinates. All other coordinates were optimized at each point in the grid. Color-mapping and Z axis shows the energy in  $\text{cm}^{-1}$ . The  $A_1$  state minimum is on the right side.

features a similar NNA. The JT distortion of the anion shifts the top and bottom beryllium atoms of the trigonal bipyramid away from one of the equatorial Be atoms, and shifts the central three membered Be ring from an equilateral triangle to isosceles. Our restricted grids suggest that there is not one singular dominant JT coordinate, and it is instead a combination of T90, T120, and R1 which distort together to determine the final JT state. The ELF plot of the  $\text{Be}_5^{-1}\text{X}^2\text{A}_2$  state and the associated BCPs are shown in Figure 5.5. The ELF plot clearly shows that the electron density has largely moved from the axial Be atoms to the equatorial Be opposite the distorted axial Be atoms at the top and bottom of the trigonal bipyramid. Additionally, the

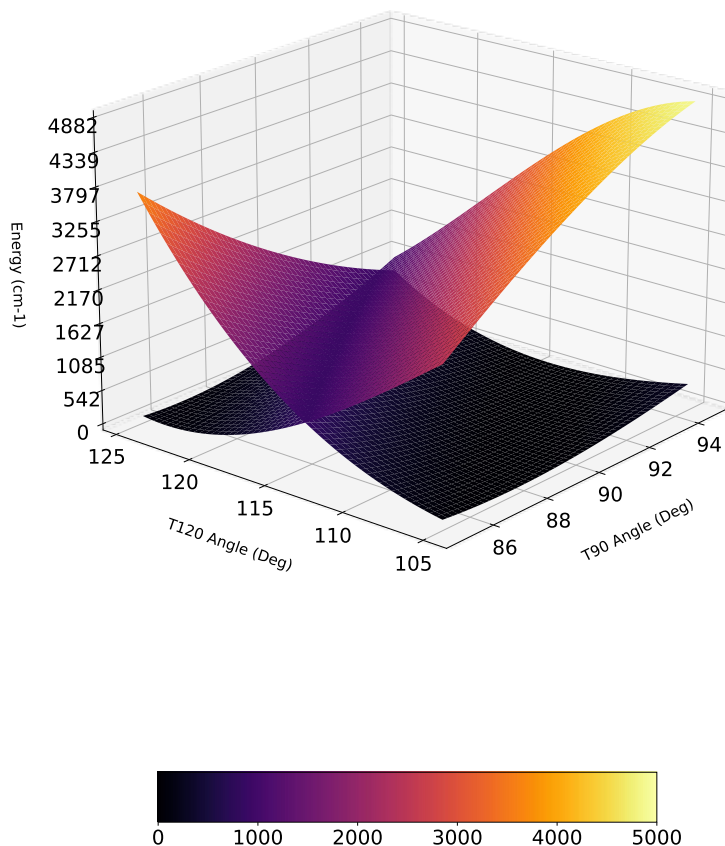


Figure 5.4: Interpolated EOMEA-CCSD/cc-pCVDZ potential energy surfaces across the T120 (deg) and T90 (deg) coordinates. All other coordinates were optimized at each point in the grid. Color-mapping and Z axis shows the energy in  $\text{cm}^{-1}$ . The  $A_1$  state minimum is on the right side.

electron density has generally become much more dispersed, rather than being focused at the top and bottom of the bipyramid in the neutral.

In addition to  $\text{Be}_5$ 's singlet ground state, the triplet excited state is also of interest. Much like the anion ground state, this excited neutral triplet state experiences a Jahn-Teller distortion from  $D_{3h}$  to  $C_{2v}$ , ( $E'' \rightarrow A_2/B_1$ ) which lends itself well to treatment with EOMEE-CC methods. At this  $C_{2v}$  geometry, the SCF energy ordering of the  $A_1'$  (now  $A_1$ ) and  $A_1''$  (now  $A_2$ ) singlet states mentioned earlier have swapped, and the  $A_2$  state is the SCF ground state by a very small 0.002 Hartree gap. Correlation effects at the MP2 and CCSD levels swap these states back to the ordering in the  $D_{3h}$

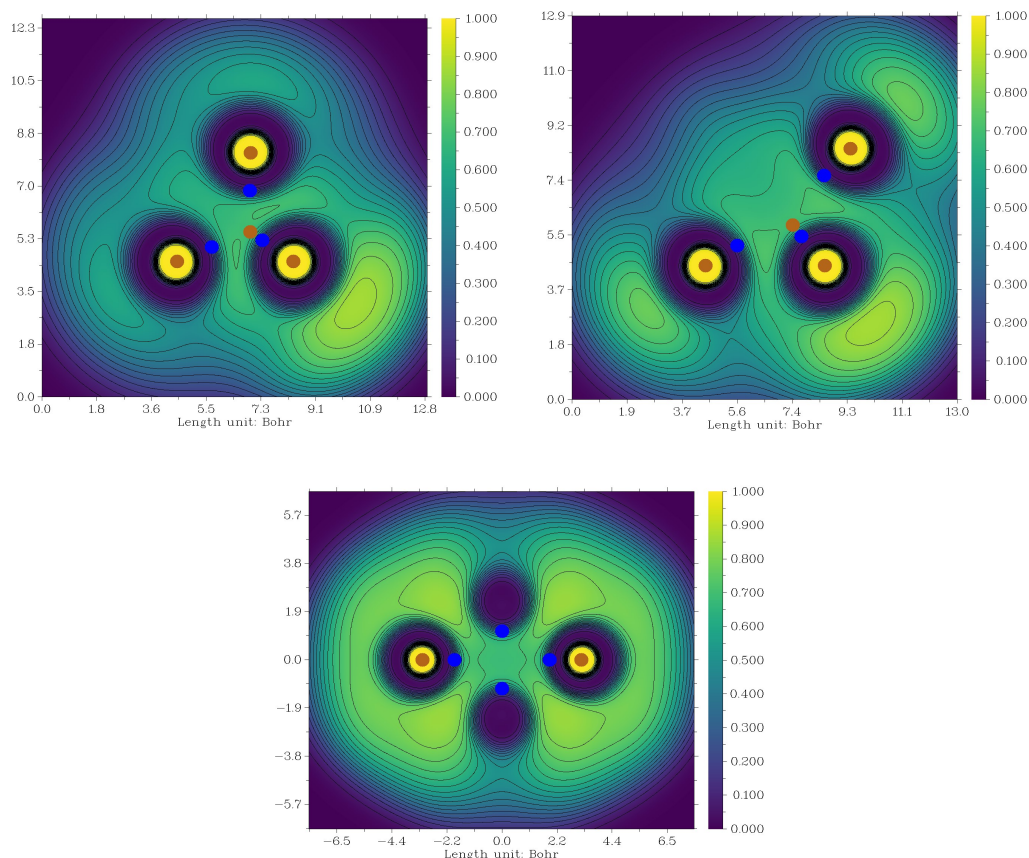


Figure 5.5: ELF contour maps along the plane of the  $\text{Be}_5^- \ ^2A_2$  equatorial ring (top left), two axial Be and one equatorial Be (top right), and two axial Be parallel to two equatorial Be (bottom). (3,-3) NNA and NCP critical points are shown as brown dots, while (3,-1) BCP critical points are shown in blue. Image and analysis performed using Multiwfn [69, 70]

geometry ( $A_1$  ground state and  $A_2$  excited state), but these states remain much closer in energy at the distorted geometry than at the more symmetric  $D_{3h}$  geometry of the singlet ground state. The singlet-triplet gap in the neutral  $\text{Be}_5$  cluster is predicted to be on the order of  $1000\text{-}2000 \text{ cm}^{-1}$  from the singlet to the lower energy triplet state from the Jahn-Teller distortion using DFT methods[16]. Our predictions using EOMEE-CC methods predict the singlet triplet gap to be larger, around  $6400\text{cm}^{-1}$  for the adiabatic energy difference and  $3200\text{cm}^{-1}$  for the vertical difference at the triplet geometry using EOMEE-CCSD with an aug-cc-pCVTZ basis and neglecting zero-point energy contributions. Additionally, the gap between the two JT states of

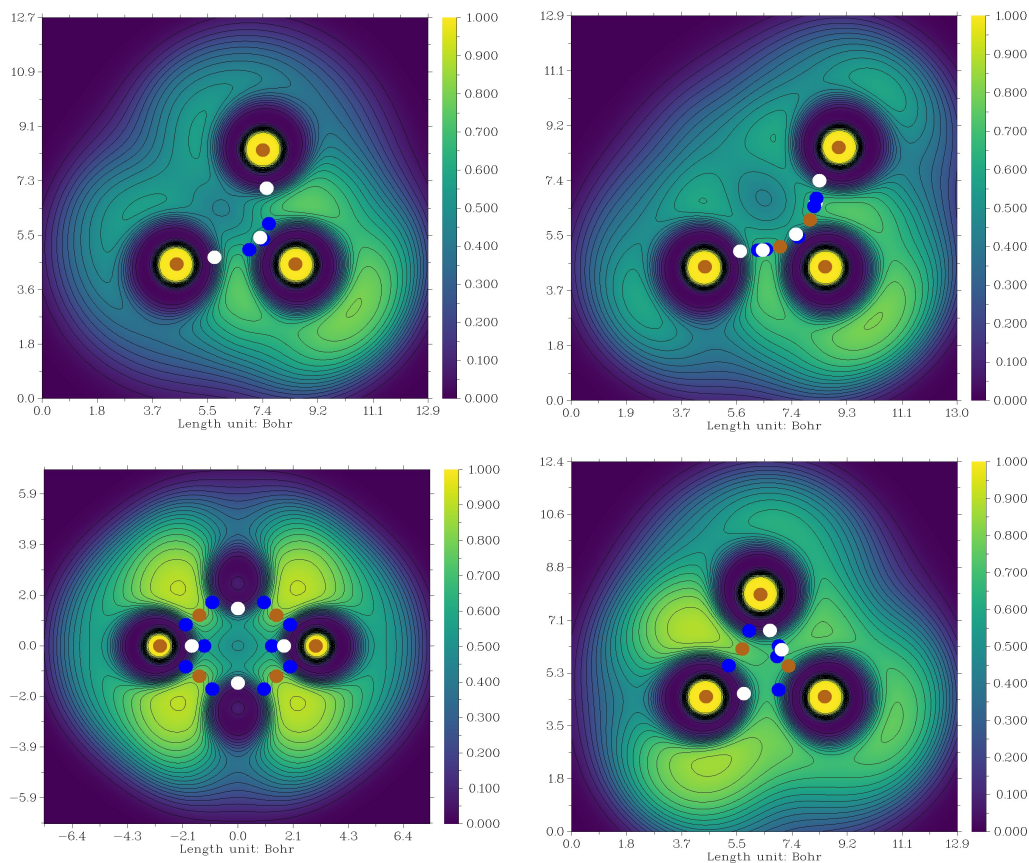


Figure 5.6: ELF contour maps along the plane of the  $\text{Be}_5$   $^3A_2$  equatorial ring (top left), two axial Be and one equatorial Be (top right), and two axial Be parallel to two equatorial Be (bottom left), and the plane of the 1, 3 and 4 Be atoms from 5.2. (3,-3) NNA and NCP critical points are shown as brown dots, (3,-1) BCP critical points are shown in blue, and (3,1) RCPs are shown in white. Image and analysis performed using Multiwfn [69, 70]

the triplet is predicted to be rather small, only  $346 \text{ cm}^{-1}$  at the EOMEE-CCSD/aug-cc-pCVTZ level. A table of the first excited triplet state's energy is given for several methods in Table 5.8, along with the optimized geometry parameters in terms of the ZMAT coordinates in Table 5.2. This singlet-triplet gap is substantially lower than the predictions and experiment on the Be tetramer, which shows the onset of triplet activity at approximately  $8000 \text{ cm}^{-1}$  above the ground state, but potentially in the range of the Be trimer where the triplet onset is approximately  $6500 \text{ cm}^{-1}$  above the neutral ground state [50].

Table 5.8: Be<sub>5</sub> A<sub>2</sub> Triplet Geometries and Energies

Method	EOMEE-CCSD	EOMEE-CCSD	EOMEE-CCSDT
Basis	aug-cc-pCVDZ	aug-cc-pCVTZ	aug-cc-pCVDZ
Energy (Hartree)	-73.35949216	-73.43328541	-73.39248814
R1 (Å)	1.317149647	1.297612516	1.320320985
R12 (Å)	1.30898925	1.277237063	1.312593366
T120 (°)	105.6204987	106.1021472	105.7075992
T180 (°)	180	180	180
R2 (Å)	1.589597702	1.576135512	1.59675349
T90 (°)	93.57816815	93.06550153	93.69222411
T901 (°)	90	90	90
M90 (°)	-90	-90	-90

Interestingly, the triplet ELF and BCP plots show a departure from the bonding motifs displayed in both the anion and neutral ground state. While we have already discussed BCPs, NNAs, and NCPs, the (3,1) ring critical point (RCP) also appears in the triplet. RCPs show a minimum of  $\rho$  in two directions and a maximum along the axis perpendicular to the ring, and as the name suggests are generally found at the center of a ring structure like benzene. In Be<sub>5</sub>'s  $1^2A_2$  state, six NNA's and seven RCP's both appear. According to the BCP analysis, this state paradoxically has no Be-Be bonds, and shows an NNA between each Be and its nearest neighbor(s). Additionally, there are ring critical points approximately between every set of three NNA's, with an additional two between the axial Be's (4 and 5 in 5.2) and the NNA that connects them to the farthest Be (1 in 5.2). These RCPs are somewhat reminiscent of the Be<sub>4</sub> topology[53], but very few other systems exist with RCPs formed at the center of NNAs. The AIM critical points are shown with their associated bond paths in Figure 5.7.



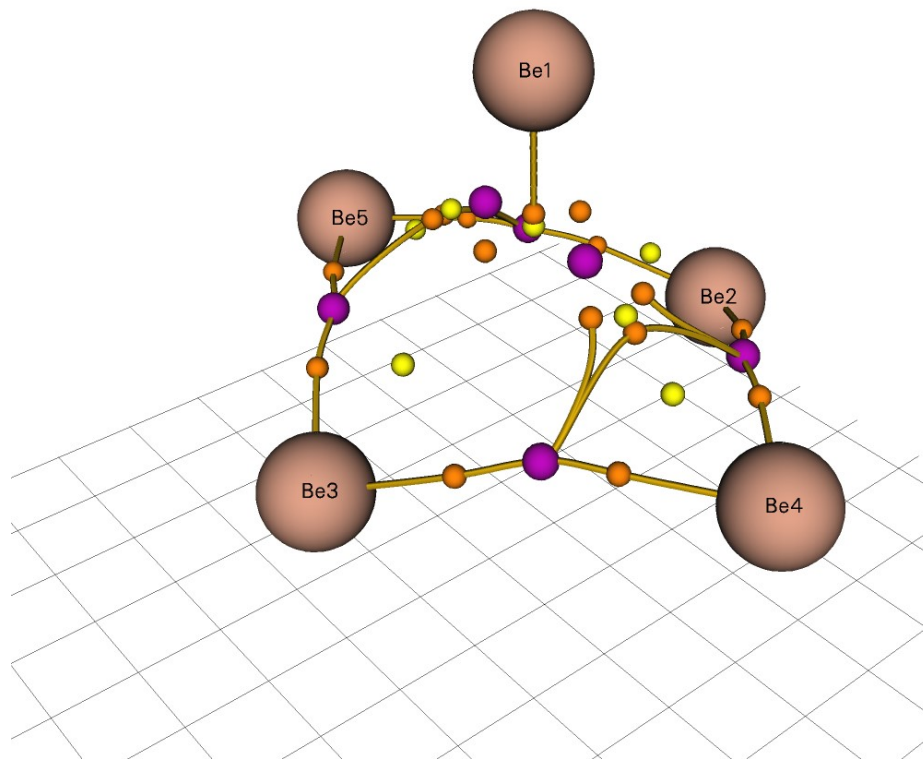


Figure 5.7: AIM analysis[71] of the  $\text{Be}_5$   $1^3\text{A}_2$  state. NNAs are shown as purple dots, BCPs as orange, and RCPs as yellow. Bonding paths have been drawn between (3,-3) and (3,-1) critical points. Image and analysis performed using Multiwfn [69, 70]

## 5.4 Experimental Results

A survey photoelectron image of  $\text{Be}_5^-$  is shown with inset velocity map image in Figure 5.8. A Nd:YAG 2nd harmonic (532nm) was used to photodetach the anions, and the double headed arrow next to the inset image shows the laser polarization vector. The electron binding energy (eBE) is given as the difference between the detachment photon energy and the kinetic energy of the detached electrons (eKE). Figure 5.8 shows two reasonably strong features with peaks at approximately  $13420\text{cm}^{-1}$  and  $15940\text{cm}^{-1}$ , as well as several weaker features beginning at approximately  $11500\text{cm}^{-1}$  that increase in intensity up to the lower energy  $13420\text{cm}^{-1}$  peak. The strongest

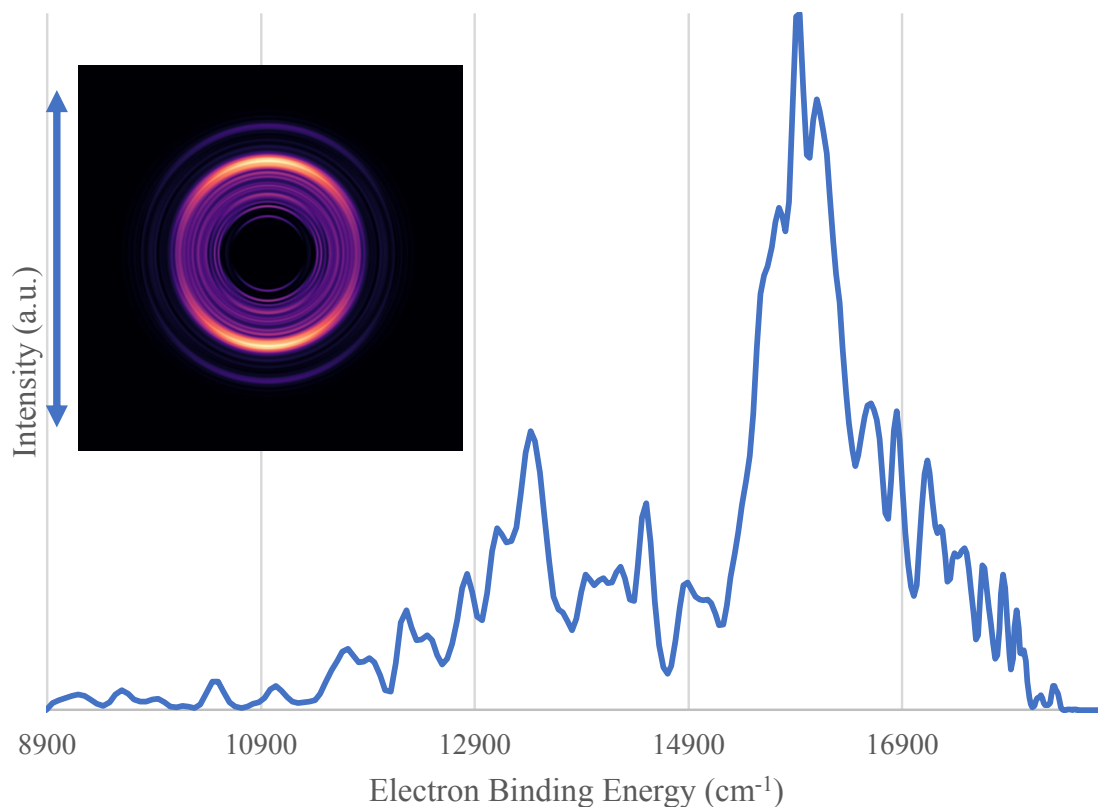


Figure 5.8: Photoelectron spectrum of  $\text{Be}_5^-$  taken with a detachment photon energy of  $18797\text{cm}^{-1}$  (532nm). Inset photo shows the velocity map image produced by MEVELER software, and laser polarization is given by the double headed arrow

feature shows a reasonable amount of parallel anisotropy, with  $\beta=1.4(0.4)$ . This is consistent with a photoelectron being detached from the anion's highest occupied  $A_1$  orbital, which corresponds to the neutral molecule's HOMO orbital, and resulting in a triplet of (at least nominally)  $A_2$  symmetry that derives from an  $E''$  JT state. Additionally, due to the large changes in geometry between the anion and neutral ground states for  $\text{Be}_5$ , compared to the reasonably small geometry shift between the anion ground state and neutral's triplet state we would expect that the anion preferentially detaches into the neutral's excited triplet state.

To further confirm this assignment, high resolution images of both features were taken. The high resolution image of the lower energy peak at  $13420\text{cm}^{-1}$  is shown in figure 5.9, and we assign this section of the spectra to  $\text{Be}_5^-X^2A_2 \rightarrow \text{Be}_5X^1A_1'$



transitions. We would like to make note that while we are assigning these transitions an  $A_2$  origin state the energy difference between the  $A_2$  and  $B_1$  states, as well as the remarkably small barrier between the two states almost ensures the true state is a distorted  $E''$  state, and the adiabatic potentials and states are an incomplete picture. As such, exact and definitive assignment of each of these peaks is near impossible, and may remain indeterminate even after cryo-cooled spectra are available. Fortunately, because of the large geometry shift between these the anion JT states and neutral ground we expect very little to no intensity for the adiabatic electron affinity (AEA, the energy difference between the equilibrium structures of the respective states), and a vibrational progression in the  $a_2''$  mode of increasing intensity to the vertical electron affinity (VEA) where the intensity would peak. As such we try to paint a more qualitative picture of these transitions, with the assignments being based on our best understanding. With the assistance of our computations, we believe the AEA to be  $12109(268) \text{ cm}^{-1}$ , which corresponds to the small peak marked by the leftmost green arrow in Figure 5.9. Because there is some amount of uncertainty in the assignment of this feature, we have elected to use a  $2.5\sigma$  uncertainty for this transition. The peaks between the AEA transition and the grey dashed lines are believed to be hot band vibration transitions between the anion ground state and neutral ground state, and the most intense peak is the vertical electron affinity (marked VEA with rightmost green arrow in Figure 5.9) at  $13325(106) \text{ cm}^{-1}$ . The peaks between the AEA peak and VEA peak are attributed to a mix of sequence bands originating from hot vibrations in the anion and a vibrational progression along the Jahn-Teller distortion coordinate ( $e'' \rightarrow a_2/b_1$ ) from the neutral's  $D_{3h}$  minimum on the potential surface to the point on the potential surface of the neutral that corresponds to the anion's  $C_{2v}$  ground state geometry. This could be the  $\nu_4 e'$  ( $a_1/b_2$ ) mode of the neutral, or the  $\nu_6 e''$  ( $a_2/b_1$ ) mode, but it is difficult to tell. The harmonic frequencies of the neutral molecule, as well as the anion  $A_2$  state's harmonic frequencies, are shown in Table 5.7. The

peaks following the VEA peak are assumed to be a continued vibrational progression of both the Jahn-Teller active mode and other vibrational modes, but the Jahn-Teller nature of these transitions makes exact assignment of each peak incredibly difficult. Additionally, we believe that the hallmarks of the  $B_1$  state are also embedded inside of the spectra presented in Figure 5.9, but as has been stated the adiabatic states paint an incomplete picture of this transition, and transitions from the pure adiabatic states that result from our EOMEA computations are not physically realistic. In lieu of an exact assignment, the position of each peak attributed to this manifold is provided in Section 5.6, Table 5.9. We hope that, as is tradition in the discussion of Jahn-Teller systems (see for example, the more than century of  $\text{NO}_3$  discussion [81–85]), others in the scientific community assist us untangling this system.

While predicting exact photoelectron angular distributions (PADs) is difficult without very high level simulation, in a low level approximation we can use the s&p model treatment to see if the anisotropy of a given PAD is consistent with our expectations. The s&p model is a simplification to the full detachment process in the molecular frame which requires that the direct product of the irreducible representation of  $\psi_{MO}$  (the initial bound orbital),  $\hat{\mu}$  (the dipole operator), and  $\psi_f$  (the free electron wave function) is invariant under the symmetry operations of the molecular point group. The s&p model additionally limits the expansion of  $\psi_f$  to  $l = 0$  (s) and  $l = 1$  (p) type partial waves [30]. These partial waves are then referenced in the lab frame axes. For an in depth overview of this treatment and the interpretations of PADs the reader is referred to Sanov’s review on the topic [30] and the original Cooper and Zare paper on the topic [31]. The VEA peak shows strong perpendicular anisotropy of  $\beta = -1.0(0.2)$ , which is consistent with our expectation of detachment from a molecular orbital of  $A_2$  symmetry within the s&p model. Notably, if this state were purely  $B_1$  symmetry, we would expect a  $\beta$  that was only slightly negative and closer to zero. This model is a simplification though, and we must also include

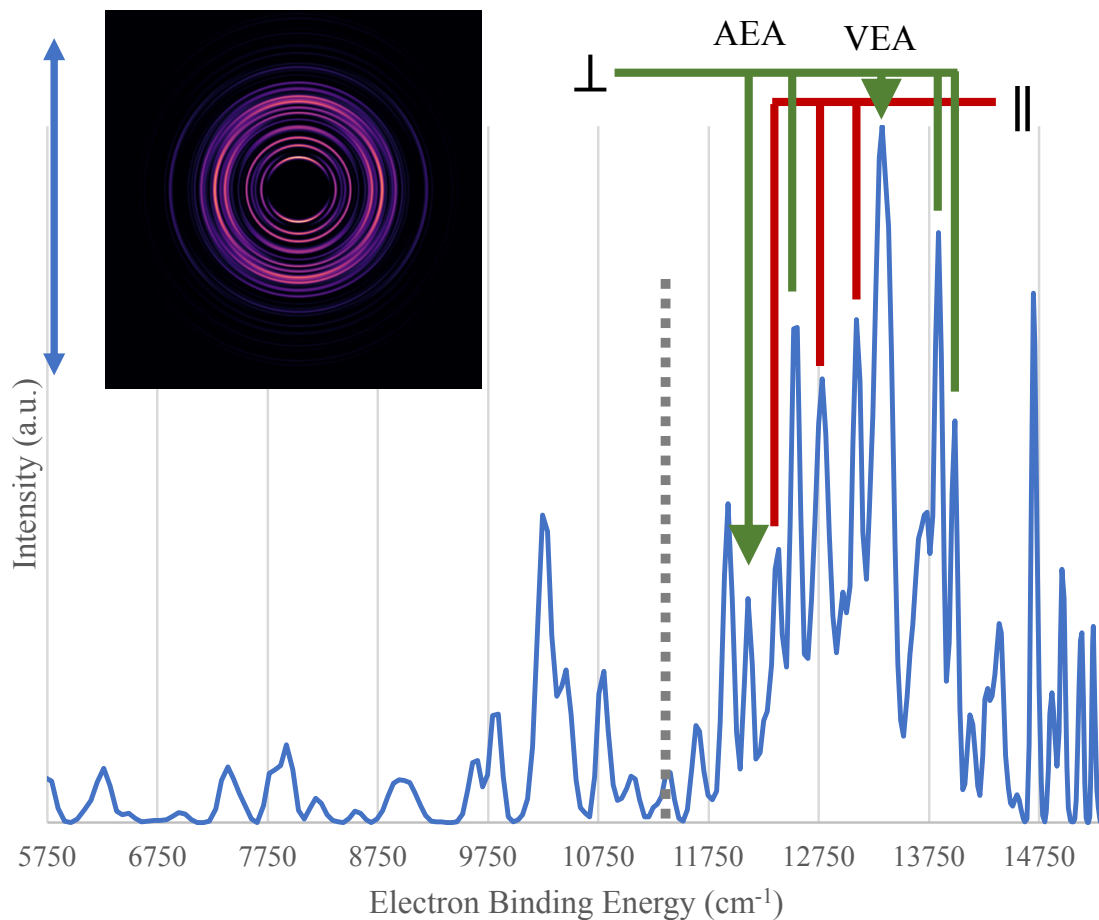


Figure 5.9: Photoelectron spectrum of  $\text{Be}_5^-$  taken with a detachment photon energy of  $15576\text{cm}^{-1}$  (642nm). Inset photo shows the velocity map image produced by MEVELER software, and laser polarization is given by the double headed arrow. Perpendicular and parallel transitions are marked by the green and red manifolds respectively.

the symmetry of the vibration to determine the anisotropy. For odd quanta changes ( $\pm 1, 3, \dots$ ) of a given asymmetric mode between the starting vibronic state in the anion and final vibronic state in the neutral we expect that the anisotropy gains parallel character that is qualitatively less than a perfect parallel detachment, as the overall symmetry of the state swaps to at least partially include  $A_1$ . It is important to reiterate that if the anion begins with excited vibrations of  $a_2$  or  $b_1$  vibrations, it would also allow for vibronic coupling between the anion  $A_2$  and  $B_1$  states in addition to the pseudorotation we expect along the ground state potential. For even quanta changes

( $\pm 0, 2, \dots$ ) in the  $a_2$ ,  $b_2$ , and  $b_1$  modes, the overall vibrational symmetry change is  $a_1$  which leaves the overall symmetry of the state as  $A_2$ , and we expect to see strong perpendicular anisotropy. Additionally, because the even change in quanta is formally allowed, and the odd change is formally forbidden, we would expect to see the perpendicular PAD transitions show more intensity than the nearby parallel transitions. It should be noted that in the case of the complex vibronic coupling of a Jahn-Teller system, things that are forbidden in a Born-Oppenheimer system are only nominally forbidden, and can still show reasonable intensity. In this system we believe we see exactly these nominally forbidden peaks in addition to the allowed transitions. The peaks in the green manifold of Figure 5.9 labeled  $\perp$  are perpendicular transitions, all of which have  $\beta = -1.0(0.4)$  corresponding to even quanta changes in the asymmetric modes, and those in the red manifold labeled  $\parallel$  are mostly parallel with  $\beta = 1.0(0.5)$  corresponding to odd transitions. The odd peak at  $10242 \text{ cm}^{-1}$  is further discussed toward the end of this section along with the other low energy peaks.

We attribute the stronger feature in Figure 5.8 to the  $\text{Be}_5^- \text{X}^2\text{A}_2 \rightarrow \text{Be}_5 1^3\text{A}_2/\text{B}_1$  ( $\text{E}''$  JT) transitions. The high resolution image of this transition is shown in Figure 5.10. The first strong peak in the figure marks the onset of the triplet, followed by a short vibronic progression. Because the geometry of the triplet is slightly offset from that of the anion, we expect that the first large peak in Fig 5.10 is the adiabatic transition to the triplet's vibrational ground state rather than a hot band, and the largest peak corresponds to a vibrational excitation of a low energy vibration mode or a sequence band. As such we assign the electron binding energy of the  $\text{Be}_5 1^3\text{A}_2$  state a value of  $15695(125) \text{ cm}^{-1}$ .

We know this excited triplet state to be an  $\text{E}''$  JT state, which will lead to substantial difficulty in exact assignment. Much like the singlet manifold, an exact assignment of each of these peaks is unlikely, and instead we list the peak positions in Section 5.6, Table 5.10. From the location of the  $\text{Be}_5^- \text{X}^2\text{A}_2 \rightarrow \text{Be}_5 \text{X}^1\text{A}'_1$  and  $\text{Be}_5^- \text{X}^2\text{A}_2 \rightarrow \text{Be}_5 1^3\text{A}_2$

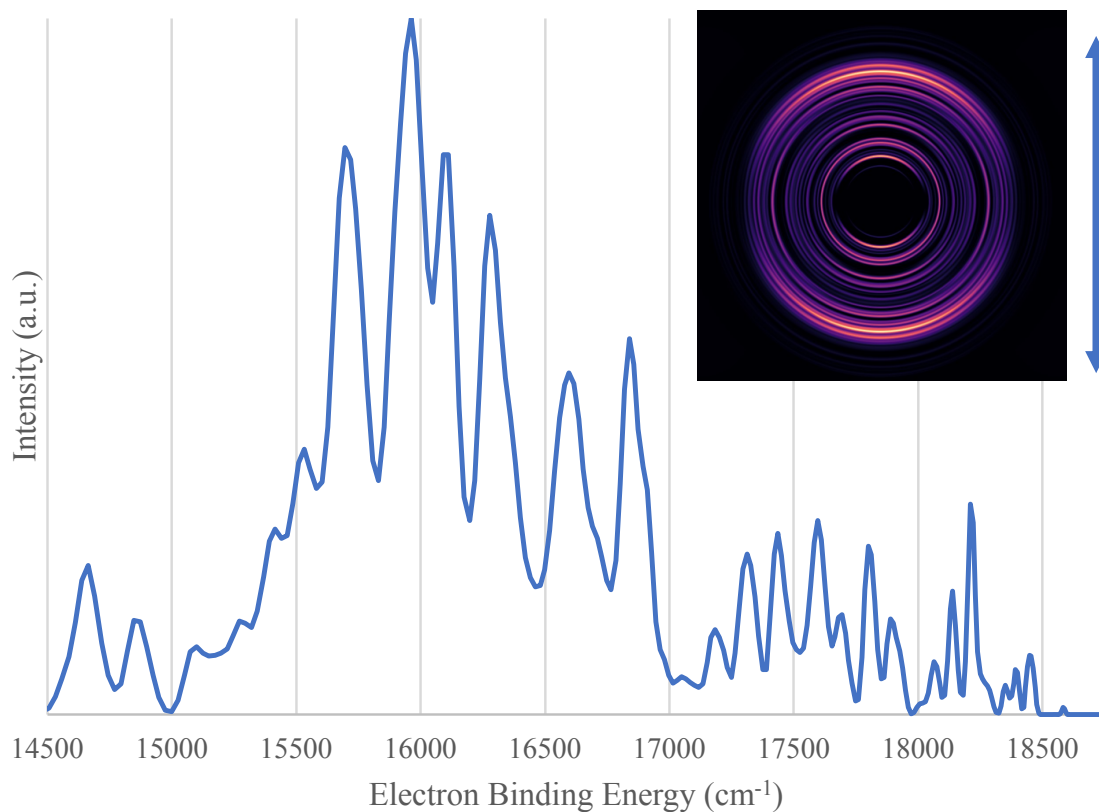


Figure 5.10: Photoelectron spectrum of  $\text{Be}_5^-$  taken with a detachment photon energy of  $18797\text{cm}^{-1}$  ( $532\text{nm}$ ). Inset photo shows the velocity map image produced by MEVELER software, and laser polarization is given by the double headed arrow. Perpendicular and parallel transitions are marked by the green and red manifolds respectively.

manifolds, we assign the  $\text{Be}_5X^1A'_1 \rightarrow \text{Be}_51^3A_2$  transition an energy of  $3585(351)\text{cm}^{-1}$ . This is in reasonable agreement with the EOMEE-CCSDT/aug-cc-pCVDZ value of the energy gap between the two states when held at the triplet geometry of  $3582\text{cm}^{-1}$ , but a far cry from the predicted adiabatic difference of  $6166\text{cm}^{-1}$ . Because the EOMEE computations rely on the neutral ground state wavefunction, this could imply that the true potential surface of the singlet is much flatter than the CCSDT/aug-cc-pCVDZ potential surface leads us to believe. Unfortunately, the inclusion of quadruples (or moving to a larger aug-cc-pCVTZ basis) to compute such a surface is much too computationally expensive using a large basis set like those required for this molecule.

The transitions in this manifold all show some amount of parallel anisotropy, with a value of  $\beta=0.7(0.3)$ . In this transition the s&p model can break down for two major reasons. Because the electron is no longer photodetached from the highest energy orbital, the approximation of the Dyson orbital being the single molecular orbital that contained the photoelectron being detached somewhat breaks down. Additionally, vibronic coupling between the  $A_2$  and  $B_1$  anion states and between the  $A_2$  and  $B_1$  triplet states makes tunneling a possibility for states with asymmetric modes, which would affect the PAD, but is not accounted for in such a basic model. Additionally, the pseudorotation that occurs in the anion ground state will also likely occur in the triplet state, as the energy difference between the  $A_2$  and  $B_1$  states in the triplet is reasonably small. If the approximation held strongly, we would expect to see higher  $\beta$  values, as the detached electron resides in an orbital of  $A_1$  symmetry. Here, we see a slight degradation of the anisotropy, but it remains mostly parallel.

Interestingly, our survey and electron affinity images both showed signal at eBE values substantially below where we would expect for ordinary vibrational hot bands. Investigation of Figure 5.9 in particular shows a reasonably strong peak at  $10242\text{ cm}^{-1}$ , and a few peaks from  $7750\text{ cm}^{-1}$  up to the  $10242\text{ cm}^{-1}$  peak. A more thorough look at the possible anion electronic states shows that there is an anion excited state of  $A_1'$  symmetry that would be dipole forbidden to relax to an  $E''$  or  $A_2$  electronic state, and that this anion excited state geometry is of  $D_{3h}$  symmetry, meaning it would also have poor wavefunction overlap with the anion JT states. Additionally the adiabatic energy difference between the anion's  $2^2A_1'$  state and the neutral  $X^1A_1'$  state is approximately  $8630\text{ cm}^{-1}$  at the EOMEA-CCSDT level with an aug-cc-pCVDZ basis set. As such we attribute this set of peaks to the excited  $\text{Be}_5^- 2^2A_1' \rightarrow \text{Be}_5 X^1A_1'$  transition, and the  $10242\text{ cm}^{-1}$  peak from Figure 5.9 to the  $\nu_9$  overtone of the neutral ground state's totally symmetric stretch, which has a fundamental frequency of  $758\text{ cm}^{-1}$  according to our CCSD/aug-cc-pCVDZ computations.

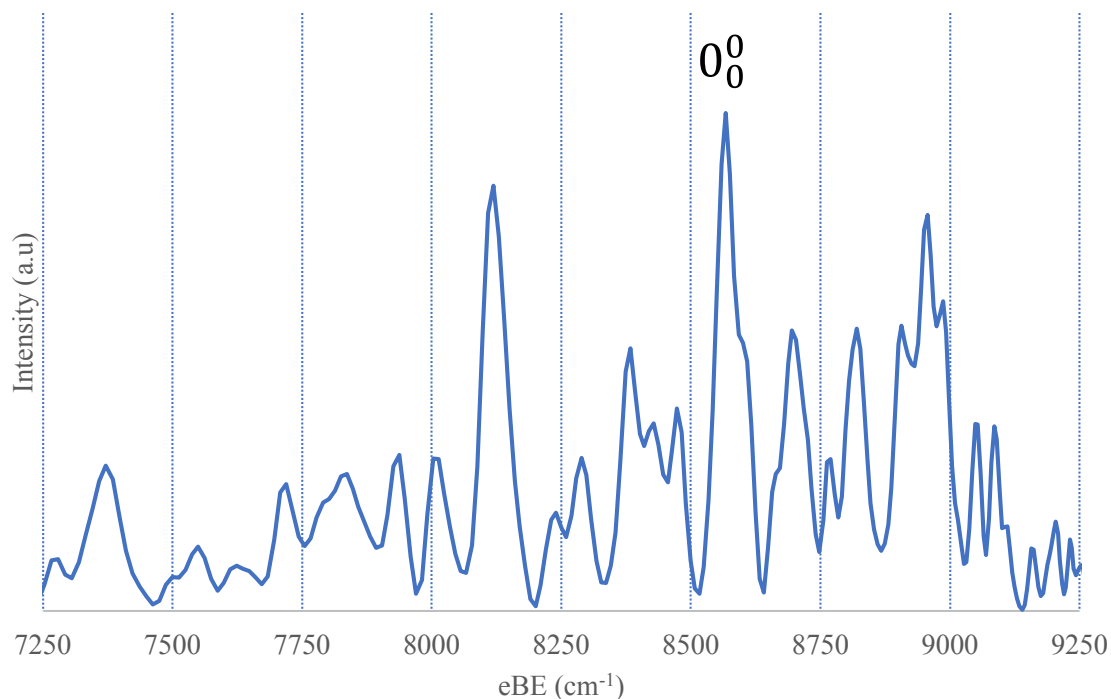


Figure 5.11: Photoelectron spectrum of  $\text{Be}_5^-$  taken with a detachment photon energy of  $9398.5 \text{ cm}^{-1}$  (1064nm). Due to low signal the anisotropy of the associated Velocity Map is over-fit and has non-physical anisotropies. As such it has been omitted

A high resolution image of this low energy spectral range is shown in Figure 5.11. The image shows three strong features, as well as a series of weaker features. The large peak at  $8567(52) \text{ cm}^{-1}$  is believed to be the  $\text{Be}_5^- 2^2A_1'$  to  $\text{Be}_5 X^1A_1'$  origin, while the strong peak at  $8119(84) \text{ cm}^{-1}$  is the result of a hot band transition originating from the  $\text{Be}_5^- 2^2A_1' \nu_5$  mode (based off the neutral's  $\omega = 473$  at CCSD/aug-cc-pCVDZ). While unassigned, the other strong peak at  $8956(88) \text{ cm}^{-1}$  is believed to be a combination band originating from an anion hot band. Imaging of this spectral range proved to be very dependant on the ablation conditions of the source, lending credence to the assignment of an anion excited state origin. Additionally, in imaging anion excited states we generally expect to see large hot band contributions to the overall spectra, explaining why there are so many weaker peaks.

## 5.5 Conclusions and Future Areas of Interest

The first in depth study of the beryllium pentamer has been completed, but several questions remain. While approximate assignments for the EA and singlet-triplet gap have been made, higher resolution and lower temperature spectra will be necessary in order to make definitive and quantitative assignments for these transitions. There is also the possibility of unraveling this spectra ‘peace-wise’ using other methods like laser induced fluorescence (LIF) techniques or cation techniques to build out the neutral state manifold and assist in untangling the current spectra. Further analysis using cryo-SEVI may also provide the necessary information to understand some of these transitions, but it is possible that this system is inherently too complex to be studied by a singular experimental method like SEVI, and studies on the singlet manifold via LIF may be a necessary piece of the puzzle here.

There is strong evidence that the pentamer represents a ‘metallic’ system based on its bonding characteristics, but the singlet-triplet gap alone implies that this molecule still behaves within a more ‘molecular’ framework. This may suggest that using the singlet-triplet and HOMO/LUMO criterion for determination of metallic character is somewhat naive or incomplete. An in depth overview of the anion’s ground Jahn-Teller potential surface showed remarkably flat surfaces and small tunneling barriers, which pose an interesting problem for future theorists to assist in solving. While this work largely neglects the triplet state of the neutral, preliminary analysis suggest it will likely follow a similar trend.

On a more personal (and perhaps unsurprising) note, Dr John Stanton does in fact have very good intuition for how these Jahn-Teller coupling problems behave, and if he suggests a Jahn-Teller system will be the end of your youth he’s probably correct.



## 5.6 Be Pentamer Supplemental Info

Table 5.9: Figure 5.9 Peaks and Intensities

eBE (cm <sup>-1</sup> )	Uncertainty (cm <sup>-1</sup> )	Intensity (a.u.)
10286	302	0.44
10799	252	0.27
11930	220	0.45
12109	268	0.32
12387	204	0.39
12555	190	0.71
12782	192	0.64
13092	122	0.72
13326	114	1
13836	100	0.84
13983	94	0.57
14696	70	0.75

Intensities have been normalized to one by dividing the max intensity from all values

Table 5.10: Figure 5.10 Peaks and Intensities

eBE ( $\text{cm}^{-1}$ )	Uncertainty ( $\text{cm}^{-1}$ )	Intensity (a.u)
15533	141	0.38
15695	137	0.81
15962	131	1
16102	150	0.8
16279	124	0.72
16597	116	0.49
16839	109	0.54

Intensities have been normalized to one by dividing the max intensity from all values

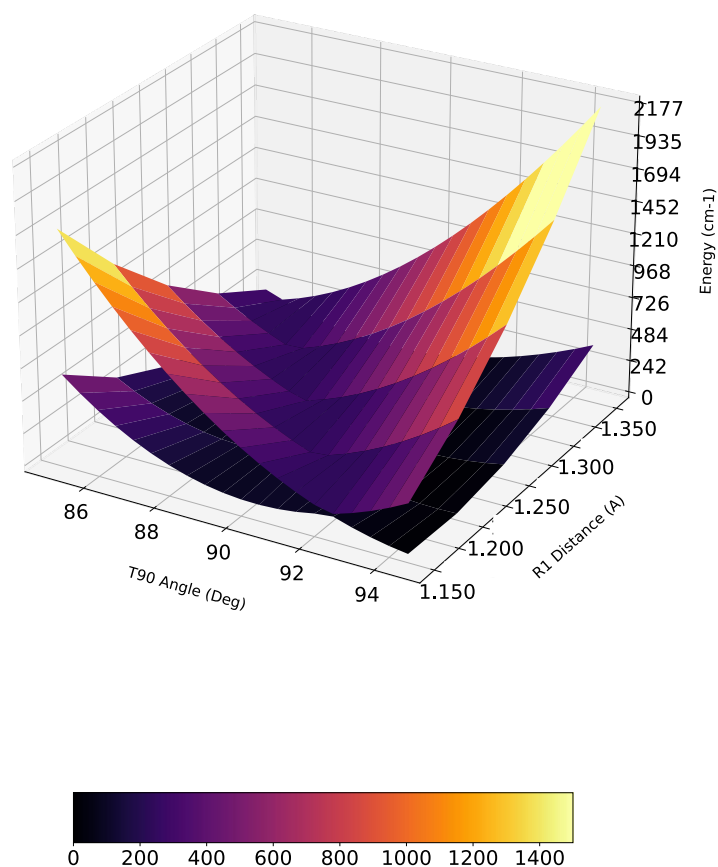


Figure 5.12: Raw EOMEA-CCSD/cc-pCVDZ potential energy surfaces across the T90 (deg) and R1 ( $\text{\AA}$ ) coordinates. All other coordinates were optimized at each point in the grid. Color-mapping and Z axis shows the energy in  $\text{cm}^{-1}$ . The  $A_1$  state minimum is on the right side.

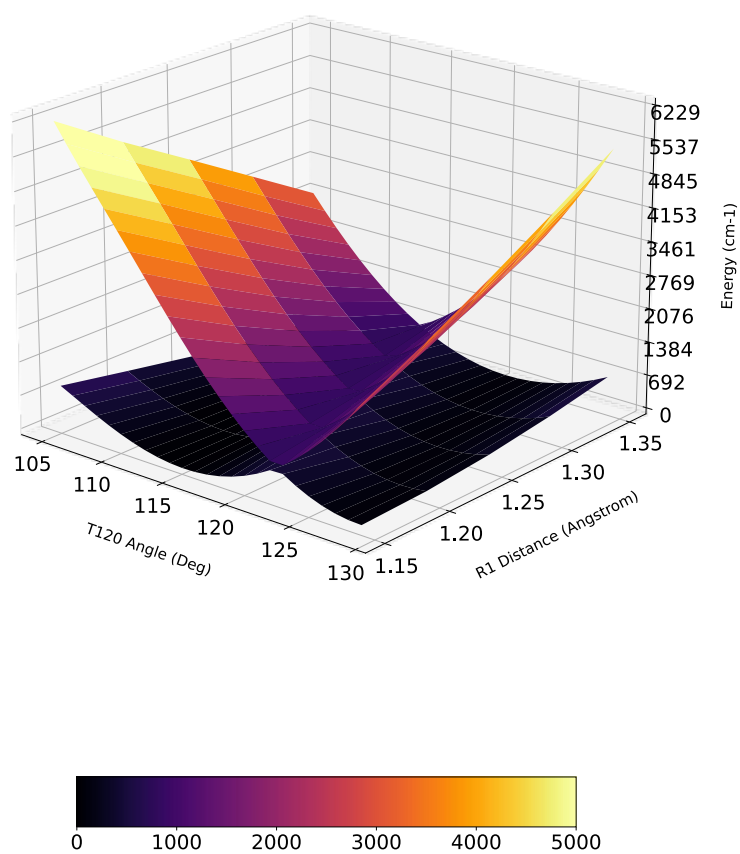


Figure 5.13: raw EOMEA-CCSD/cc-pCVDZ potential energy surfaces across the T120 (deg) and R1 ( $\text{\AA}$ ) coordinates. All other coordinates were optimized at each point in the grid. Color-mapping and Z axis shows the energy in  $\text{cm}^{-1}$ . The  $A_1$  state minimum is on the right side.

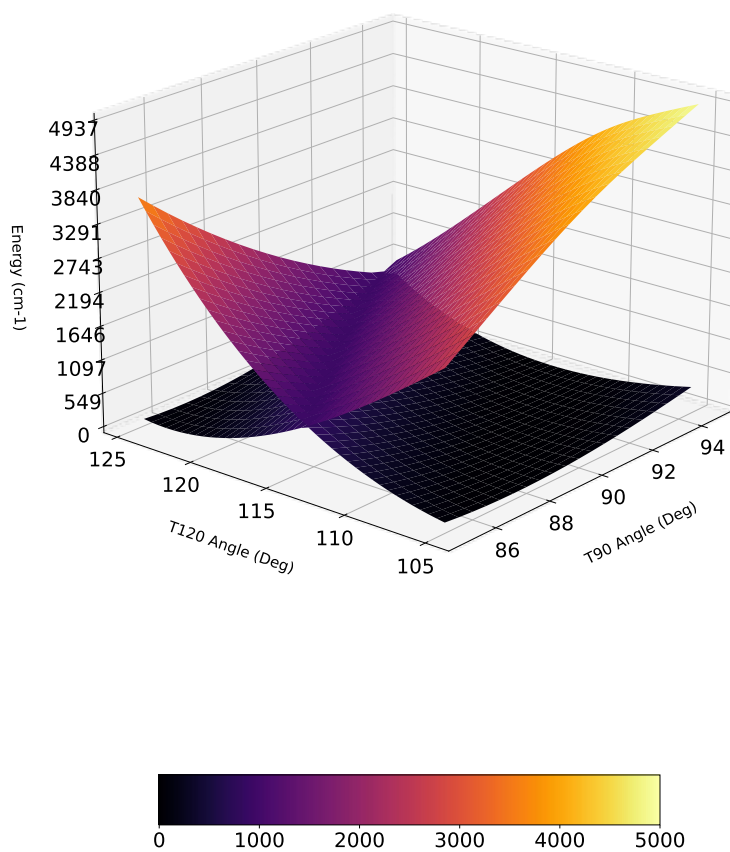


Figure 5.14: raw EOMEA-CCSD/cc-pCVDZ potential energy surfaces across the T120 (deg) and T90 (deg) coordinates. All other coordinates were optimized at each point in the grid. Color-mapping and Z axis shows the energy in  $\text{cm}^{-1}$ . The  $A_1$  state minimum is on the right side.

## Chapter 6

# All Bets Off: Multireference Problems in Hyper-metallic Beryllium Oxide Clusters

Hyper-metallic oxides are an ongoing area of interest due to their unique properties. While there have been a reasonable number of theory studies on  $(\text{BeO})_n$  ( $n=1,2,\dots$ ) clusters, with the exception of  $\text{BeOBe}$ , the hyper-metallic  $\text{Be}_n\text{O}$  clusters have not received the same attention. Here we present preliminary spectra for these  $\text{Be}_n\text{O}$  clusters ( $n=2,3,4,5$ ), as well as a brief overview of their electronic structure *ab initio* methods. Additionally, spectra of the  $n=6, 7$ , and  $8$  clusters are presented, with computational analysis and exact assignment remaining an open question. The clusters show substantial non-monotonic changes with respect to their electron affinities and spectral density, and evidence of large multireference contributions.

## 6.1 Introduction and Background

The current literature on Be hyper-metallic oxides largely centers on BeOBe. A molecular orbital based bonding approach to BeO would suggest that Be shares its 2s electrons with the O atom, and forms a reasonably happy octet that has no reason to bond to another Be atom. Early mass spectrum studies of hot Be based vapors found large quantities of  $\text{Be}_2\text{O}^+$ , which suggested the reasonable stability of the parent neutral molecule [86]. This observation spurred on early studies [87, 88] which suggested both BeBeO and BeOBe were stable structures, with the latter being the global minimum. The bonding of the hyper-metallic Be atom was determined to be due to the lack of full 2s electron donation from the initial Be atom in BeO, which allows the second Be to bond with the existing BeO [18, 87]. These initial studies also found that there is an exceptionally small splitting between the singlet and triplet states of the neutral molecule, that the state ordering was very sensitive to the level of theory applied, and that the BeOBe  $^1\Sigma_g^+$  state was best described using multireference based methods [87, 88]. Due to the singlet's multireference character, single reference methods commonly predicted a  $^3\Sigma_u^+$  ground state, while multireference often favored a  $^1\Sigma_g^+$  minimum (initial MP2 predictions suggested that the  $^1\Sigma_g^+$  state was roughly  $6000\text{ cm}^{-1}$  above the  $^3\Sigma_u^+$  state [87]). Following theory based studies using single reference methods were indeterminately reliable until an in depth series of experimental studies on the neutral and cation were performed, which were able to determine that the ground state of the neutral is a  $^1\Sigma_g^+$  via nuclear spin statistics [18, 20]. While this did determine the true ground state, experimental validation for the energy gap between the two states has remained elusive to the present date.

A series of reasonably recent *ab initio* studies on of the alkali-earth MOM (M=Be, Mg, Ca, Sr, Ba, Ra) by Ostojić et al used CASSCF and MRCI methods to predict the low energy IR vibrational spectra of these species as well as the singlet-triplet gaps [89–92]. For BeOBe, they predicted this singlet-triplet gap to be  $280\text{ cm}^{-1}$  using a

complete basis extrapolation of MRCI energies. Merritt et al had also predicted this splitting with FV-CASSCF/MRCISD(2,2)+Q and FV-CASSCF/MRCISD(10,12)+Q with a cc-pCVQZ basis, obtaining estimates of  $242\text{ cm}^{-1}$  and  $39\text{ cm}^{-1}$  respectively [18]. Merritt et al also made a FV-CASSCF/cc-pCVQZ prediction of  $154\text{ cm}^{-1}$ . While Merritt was able to predict these splittings, they were not able to observe them in their resonance enhanced multi-photon ionization (REMPI) study. Similarly, a later study of the cation using pulsed field ionization zero electron kinetic energy (PFI-ZEKE) was unable to observe the splitting [20]. This is because both of these methods rely on exciting through an intermediate state, which will select out for one of the manifolds through the intermediate. These studies were able to experimentally determine vibrational frequencies for the ground state [18].

Surprisingly, despite the interest in the stoichiometric  $(\text{BeO})_n$  clusters [93, 94], beyond the BeOBe studies there are no studies of the hyper-metallic  $\text{Be}_n\text{O}$  clusters. The related  $\text{Mg}_n\text{O}$  ( $n=1, 2, 3, 4$ ) clusters were studied by generating MP2/6-31G\* geometries and examining the energies at up to the QCISD(T)/6-311+G\* level [95]. Notably, this single reference treatment favors the triplets in the MgOMg [89, 95], and the study also found that the  $\text{Mg}_3\text{O}$  clusters had similar multireference character. The  $\text{Mg}_4\text{O}$  cluster's potential multireference character was not investigated.

## 6.2 Computational Studies

Previous studies on Be based anions have shown us that the EOMEA-CC type methods are often a reasonable and good approach for determining properties like the electron affinity and structure of Be containing anions (see: [50] and Section 5.3). In what might be accurately described as a moment of extreme hubris, we also attempted to use these methods to compute the properties of the hyper-beryllium oxides as well. These attempts are roughly outlined in this section.



As has been previously discussed in Section 5.1, one mechanism to determine the multireference character of a molecule within the coupled cluster framework is to inspect the  $T_1$  and  $T_2$  diagnostics, as well as the the largest  $t_1$  and  $t_2$  amplitudes [96]. In general, larger  $t_1$  and  $t_2$  amplitudes and  $T_1$  and  $T_2$  diagnostics point toward more multireference character and a wavefunction that is poorly described by a single reference determinant. Previously it has been shown that  $\text{Be}_2$ , a known multireference problem child, has a largest  $t_2$  value of approximately 0.225 [67]. The Be dimer ground state is not accurately described by CCSDT quantitatively, but is qualitatively described reasonably well [1].

Our initial study on  $\text{Be}_2\text{O}$  using coupled cluster methods up to CCSDT found, perhaps unsurprisingly given past MRCI and CASSCF studies [18, 91], incredibly large  $t_2$  amplitudes. Our CCSD/aug-cc-pCVDZ study reports that the excitation coupling the two largest contributors to the multireference wavefunction, namely the  $|3\sigma_g^2 1\pi_u^4 4\sigma_g^2\rangle$  and  $|3\sigma_g^2 1\pi_u^4 4\sigma_u^2\rangle$  single reference determinants, has a  $t_2$  amplitude of -0.742. This is almost twice that of  $\text{Be}_2$  and more than three times that of  $\text{Be}_5$ . The two orbitals involved in this excitation are shown in Figure 6.1, and correspond to the HOMO and LUMO of the singlet SCF wavefunction. The orbitals here are particularly demonstrative of the source of the problems in computing the singlet and the lack of problems in the triplet state. In the singlet, the ground state CI vector is  $0.729|4\sigma_g^2 1\pi_u^4 3\sigma_u^2\rangle - 0.602|3\sigma_g^2 1\pi_u^4 4\sigma_g^2\rangle$  [18]. In the triplet, the leading term in the CI vector is  $0.953|3\sigma_g^2 1\pi_u^4 4\sigma_g 3\sigma_u\rangle$  [18]. Because the triplet is effectively a single reference state, while the singlet is nearly a 50-50 split, capturing the singlet accurately is not realistic with a single reference treatment. Additionally, because the the major change between the  $4\sigma_g$  and  $3\sigma_u$  is if the Be atoms' (largely undisturbed by the oxygen atom) 2s orbitals are an in or out of phase combination, and both orbitals show only very small contributions from the oxygen p orbitals, these two orbitals are near degenerate.

Interestingly, when we move to the  $\text{Be}_3\text{O}$  cluster, we begin to see a departure from

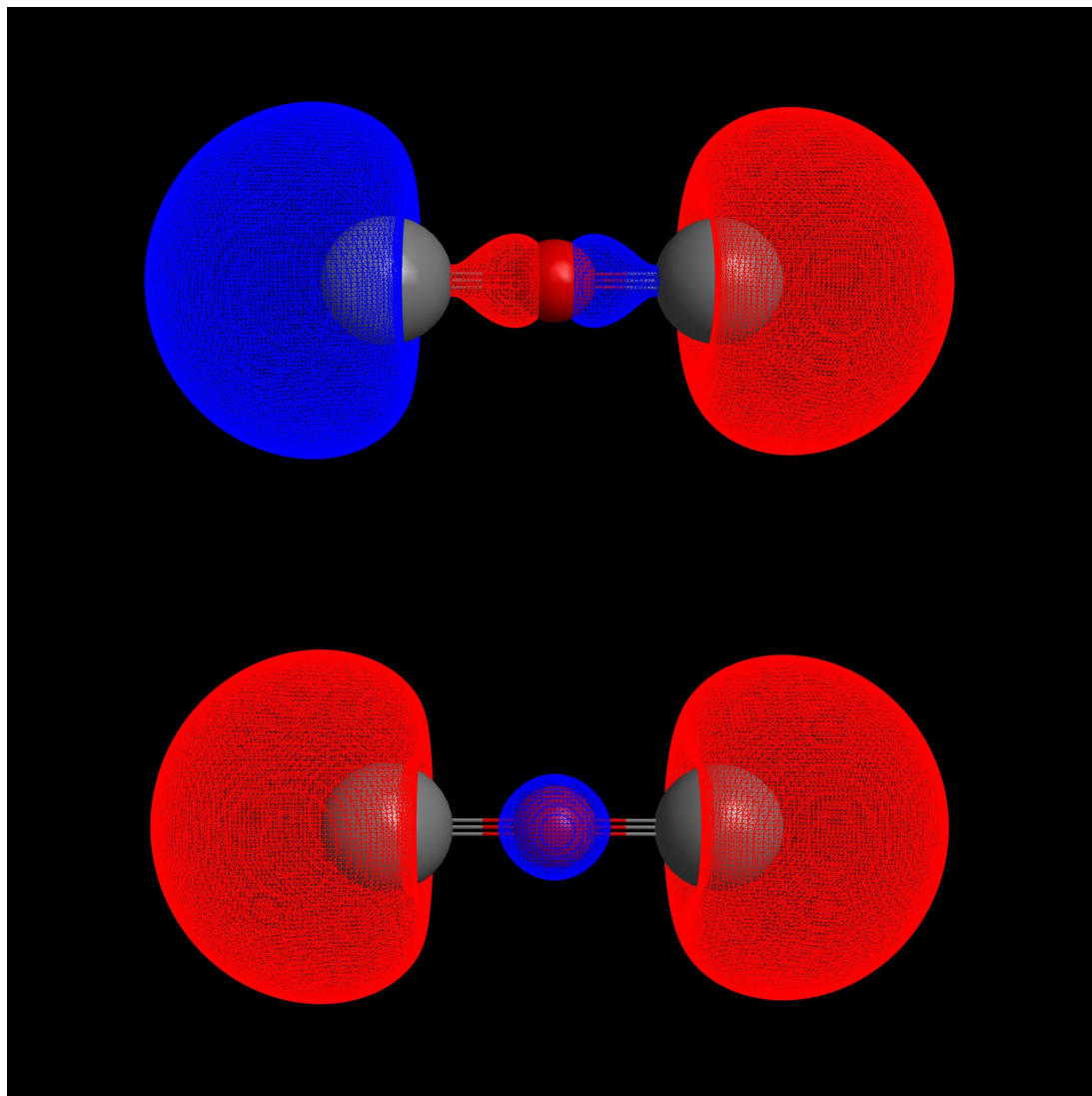


Figure 6.1:  $|3\sigma_g^2 1\pi_u^4 3\sigma_u^2\rangle$  (top) and  $|3\sigma_g^2 1\pi_u^4 4\sigma_g^2\rangle$  (bottom) orbitals. Image produced using wxMacMolPlt[97].

the results of the  $\text{Mg}_3\text{O}$  cluster study [95]. While  $\text{Mg}_3\text{O}$  was predicted to have a  $C_{2v}$  ground state geometry resembling a  $\text{Mg}_3$  triangle with an O atom placed in the center, we found that  $\text{Be}_3\text{O}$  resembles a Be atom attaching itself linearly to BeOBe when studied at the CCSD/aug-cc-pCVDZ level. The SCF HOMO and LUMO orbitals are shown in Figure 6.2. These orbitals are almost exactly the same as those of BeOBe with the addition of an excess Be atom that is either in or out of phase with the farthest Be atom. Additionally, the CCSD/aug-cc-pCVDZ bond lengths rather

closely resemble that of the Be dimer and BeO, with a Be-Be bond length of 2.12 Å on the dimer unit, Be-O bond length of 1.44 Å on the Be dimer-O beryllium atom, and a bond Be-O bond length of 1.43 Å on the final Be-O bond. What is even more interesting and (in a twisted sense) impressive about this molecule is its massive max  $t_2$  amplitude of -0.84 for the excitation links the HOMO and LUMO. This seems to suggest that in addition to inheriting some geometry parameters from both Be<sub>2</sub> and BeOBe, it has also inherited the worst parts of the multireference character from both.

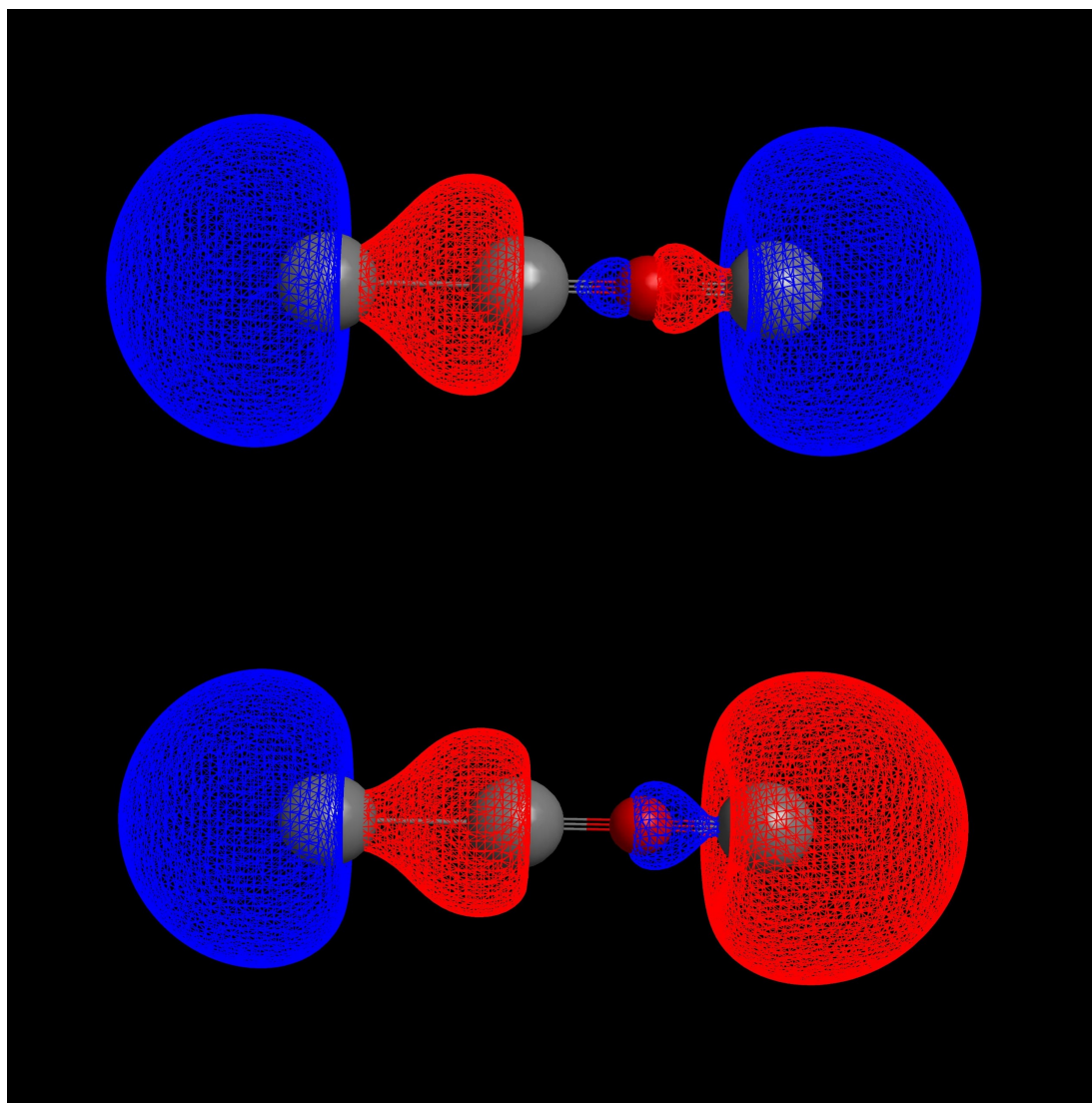


Figure 6.2: The HOMO (bottom) and LUMO (top) orbitals of BeBeOBe. Image produced using wxMacMolPlt[97].

The  $\text{Be}_4\text{O}$  cluster also departs from the  $\text{Mg}_4\text{O}$  cluster, as it is predicted to be a linear,  $D_{\infty h}$  molecule rather than a  $C_{2v}$  like  $\text{Mg}_4\text{O}$  as reported by Boldyrev [95] when studied by CCSD with an aug-cc-pCVDZ basis. Interestingly, the orbital ordering appears to shift around in  $\text{Be}_4\text{O}$ , and the HOMO/LUMO orbitals become  $\pi_u$  and  $\pi_g$  symmetry respectively. This orbital reordering improves the behavior of the single reference wavefunction based on the  $t_2$  criterion, with a max  $t_2$  amplitude of -0.406 for the excitation linking the HOMO and LUMO, which is ‘only’ double that of  $\text{Be}_2$ .

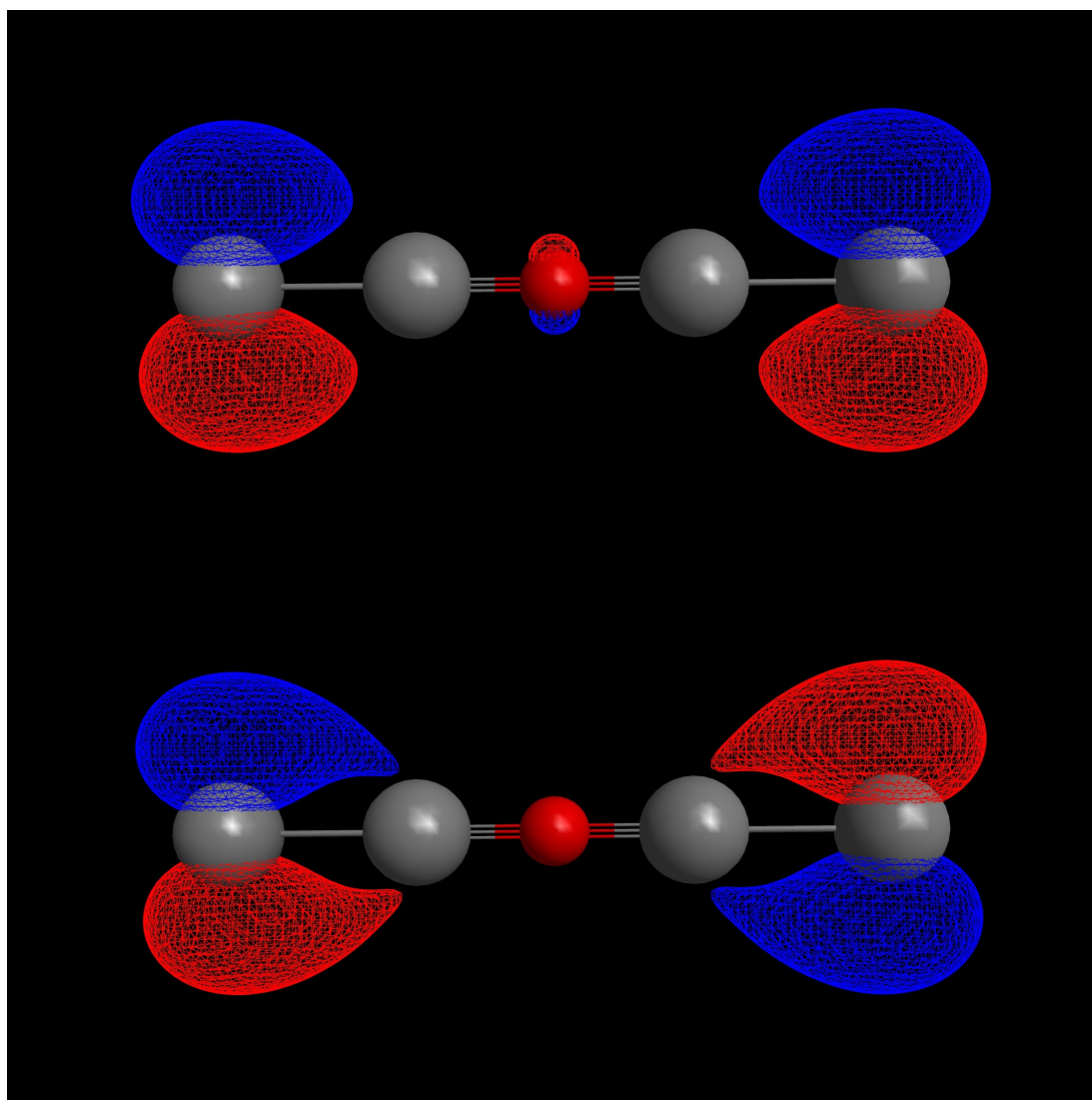


Figure 6.3: The HOMO (top) and LUMO (bottom) orbitals of  $\text{BeBeOBeBe}$ . Image produced using wxMacMolPlt[97].

Higher order clusters produced interesting results, with  $\text{Be}_5\text{O}$  taking on a structure that is either a ring or consists of a  $\text{Be}_3$  ring and a bent  $\text{Be}_2\text{O}$  unit forming an aggressively folded chair type conformation (geometries shown in Figure 6.4 with HOMO orbitals plotted), both of which are stable and within  $200\text{ cm}^{-1}$  of each other when optimized at the CCSD/aug-cc-pCVDZ level. Further computations on these larger clusters have been neglected until a proper multireference treatment of the  $\text{Be}_3\text{O}$  and  $\text{Be}_4\text{O}$  clusters can be completed, and the validity of our CCSD treatment can be verified, which has been left as a future point of study.

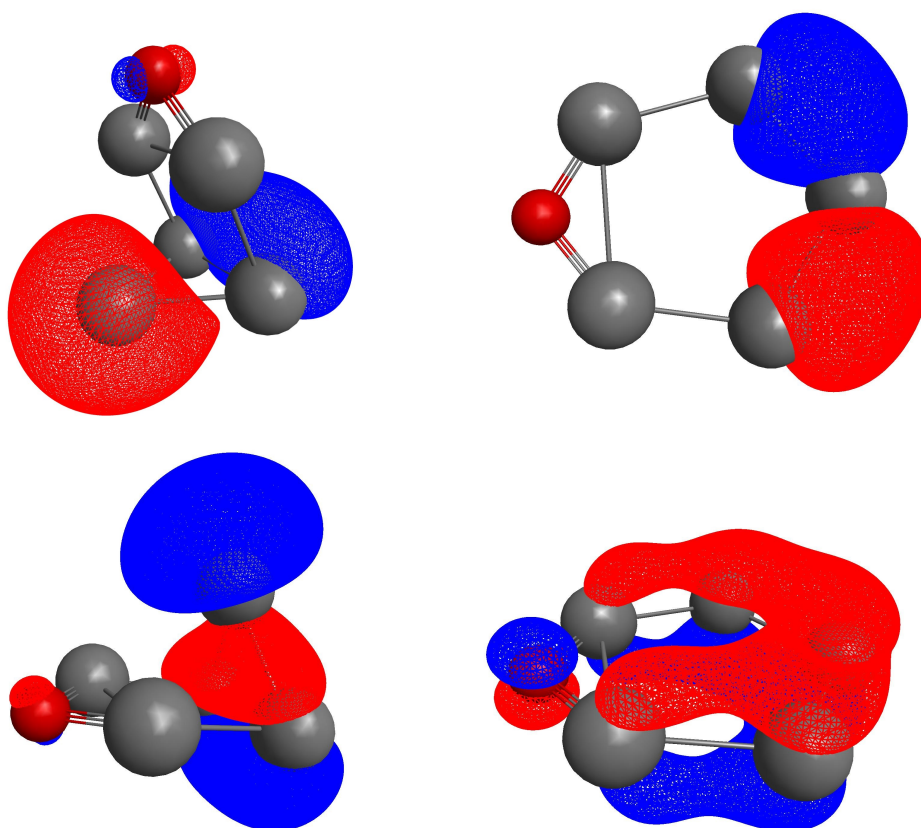


Figure 6.4: Chair type  $\text{Be}_5\text{O}$  geometry (left) and  $\text{Be}_5\text{O}$  ring geometry (right) plotted with their respective HOMO(top) and LUMO (bottom) orbitals. Image produced using wxMacMolPlt[97].

## 6.3 Experimental Procedure

An in depth description of the experimental apparatus can be found in Chapter 2. The details specific to  $\text{Be}_n\text{O}$  clusters and a brief overview are found here. Beryllium oxides were produced via pulsed laser ablation in an argon backing gas seeded with 0.75%  $\text{N}_2\text{O}$  and 0.75%  $\text{O}_2$ . Gas pulses were produced using an Even-Lavie [36] type valve with a backing pressure of approximately 1000PSI. The supersonic expansion was directed into our WM-TOFMS where all anions were directed down the TOF axis. As the anions travel, they are mass separated in time, and pass over a series of steering optics and an Einzel lens. The steering optics serve to condition the beam and ensure it is traveling as axially as possible, and the Einzel lens focuses the anions into the photodetachment region in the final chamber. As the anions leave the second chamber, they pass over a mass gate which rapidly turns off as the anion of interest passes over it, allowing it to pass into the final chamber. The final chamber contains the VMI optics, where the electrons are photodetached from the anions using a vertically polarized photodetachment laser. These experiments used a photodetachment wavelength of 532nm for the survey conditions, produced using the second harmonic of an Nd:YAG laser. Longer wavelengths were generated with a Nd:YAG 2nd harmonic pumped dye laser or OPO, and wavelengths were confirmed using a Bristol Wavemeter. These photodetached electrons are then focused onto our chevron stacked MCPs, which in turn light up a phosphor screen that is recorded by a CCD camera. The CCD camera output is fed to the lab computer, which discriminates high signal shots from low signal shots based on the voltage output of a photomultiplier tube (PMT) that also views the phosphor screen, as described in Section 2.7.1. Photodetachment efficiency for these clusters ranged from 0.5% ( $\text{Be}_4\text{O}$ ) to 30% ( $\text{Be}_5\text{O}$ ) depending on the cluster of interest. Images were pre-processed using custom written python software described in Section 2.7.2, and processed using MEVELER [45]. Image reconstructions were produced in python using the output

of the MEVELER software. Calibrations of the spectra were performed using known transitions of the  $S^-$  anion as described in Section 2.8. All uncertainties given are  $2\sigma$  values and are determined by propagating the uncertainty in pixel space to energy space, unless otherwise noted.

## 6.4 Experimental Results

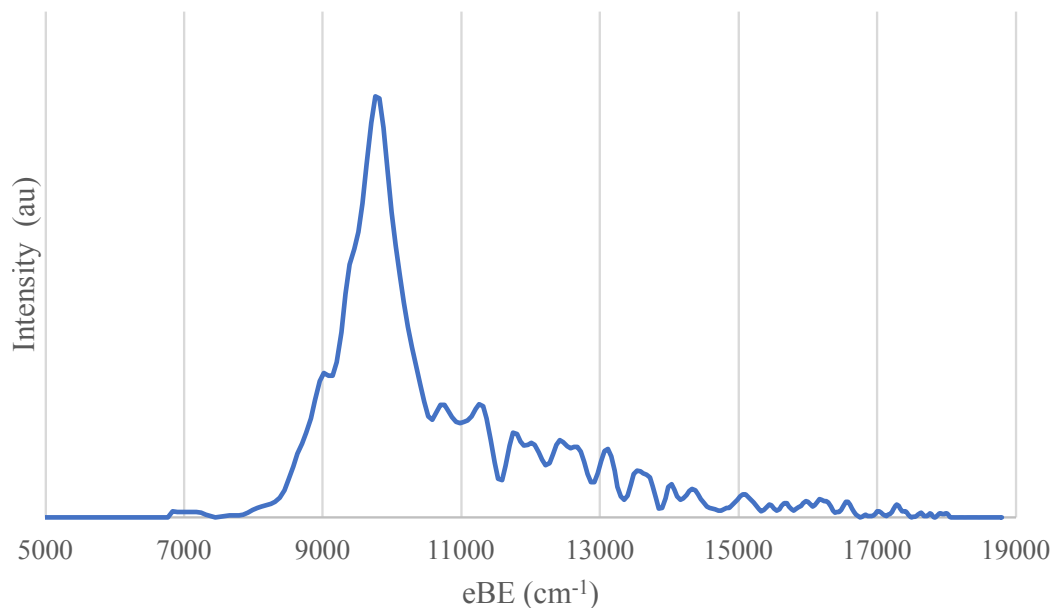


Figure 6.5:  $18797\text{ cm}^{-1}$  photodetachment spectrum of BeOBe showing a singular wide feature at approximately  $9750\text{ cm}^{-1}$ .

Our study of  $\text{Be}_n\text{O}$  clusters began with  $\text{Be}_2\text{O}$  in an attempt to experimentally determine the singlet-triplet gap, which has plagued the theoretical community for decades. Our initial  $18797\text{ cm}^{-1}$  detachment survey spectrum shown in Figure 6.5 shows only a singular wide peak at approximately  $9750\text{ cm}^{-1}$ . The electron binding energy (eBE) is given as the difference between the electron kinetic energy (eKE) of detached photoelectrons and the detachment photon energy. Using SEVI, we are able to increase the resolution by changing both the photodetachment energy and the voltage applied to our VMI plates. The high-resolution image of this wide feature



shows substantial structure, and is given in Figure 6.6. We attribute the two largest peaks at  $9583(60) \text{ cm}^{-1}$  and  $9730(57) \text{ cm}^{-1}$  to the  $\text{BeOBe}^{-1}\text{X}^2\Sigma_u^+ \rightarrow \text{BeOBe}\tilde{\text{X}}^1\Sigma_g^+$  and  $\text{BeOBe}^{-1}\text{X}^2\Sigma_u^+ \rightarrow \text{BeOBe}\tilde{\text{a}}^3\Sigma_u^+$  transitions. This yields a singlet triplet gap of  $147(12)$ . Note that because our uncertainty largely comes from the centering of the image, energy gaps like this have a lower uncertainty than raw transition values. The series of peaks labeled  $2_{2n}^0$  with  $n=1, 2, 3$  are attributed to hot bands originating in the bending mode of the anion to the  $^1\Sigma_g^+$  state and  $2'_{2n}$  are transitions into the  $^3\Sigma_u^+$  state. While the transitions have been labeled ending in the  $\nu_2 = 0$  mode, the width of these peaks means we cannot determine a difference between changes of the same quantum numbers as the listed transition (for example,  $2_{2n+1}^0$  and  $2_{2n}^0$  are likely not distinguishable at this resolution). Because of the asymmetry of the bending mode, we expect only even quanta changes. This spectrum then yields a fundamental value for the anion  $\nu_2$  bending mode of  $148(18) \text{ cm}^{-1}$ .

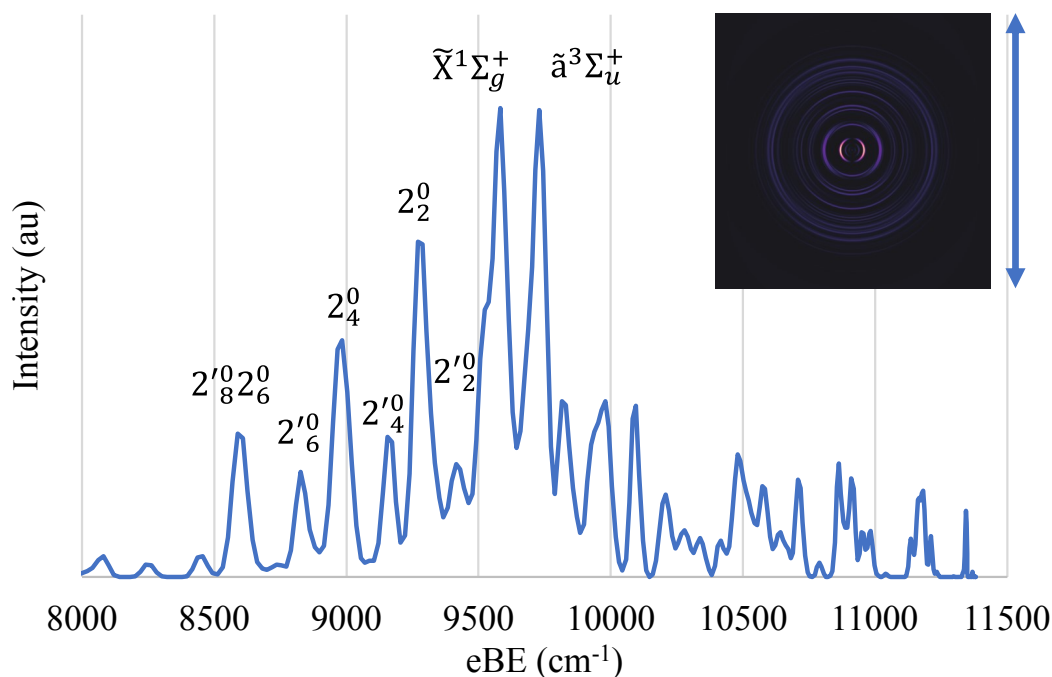


Figure 6.6:  $11380 \text{ cm}^{-1}$  photodetachment spectrum of  $\text{BeOBe}$  showing several features as well as the singlet triplet split. Bands to the left of the  $\tilde{\text{X}}^1\Sigma_g^+$  peak are attributed to hot bands of the  $\nu_2$  bending mode in the anion. Inset image shows the velocity map image produced by MEVELER [45], and laser polarization is shown by the double headed arrow.



During our study of BeOBe, the higher order clusters were also readily produced. Unfortunately, due to the difficulty inherent in theoretical prediction of these clusters, we are only able to make general statements on the structure. As such, while the data presented here is novel, our commentary and ability to analyse it at this time is minimal.

The  $18797\text{ cm}^{-1}$  detachment spectrum of  $\text{Be}_3\text{O}$  is shown in Figure 6.7. The spectra shows an onset at approximately  $8500\text{ cm}^{-1}$ , and a dramatic increase in complexity compared to the BeOBe and BeO spectra [21]. Additionally, there is a slight decrease in the onset of electrons from roughly  $9600\text{ cm}^{-1}$  in  $\text{Be}_2\text{O}$  to  $8500\text{ cm}^{-1}$  in  $\text{Be}_3\text{O}$ . The velocity map image shows reasonable vertical anisotropy consistent with detachment from a sigma state, as predicted. It is likely that the large density of transitions is due to both an assortment of vibrations and multiple electronic states, but further work needs to be done to exactly determine what these peaks represent. It seems incredibly likely based on our limited computations that the singlet-triplet splitting here is similarly small to BeOBe, rather than a large gap like BeO, and that this spectra shows features from multiple higher level excited states.

The survey spectrum of  $\text{Be}_4\text{O}$  is shown in Figure 6.8. The notable shift from parallel anisotropy in the smaller clusters to perpendicular here suggests that our electron now resides in a  $\pi$  type orbital, which is consistent with our expectation of the HOMO/LUMO orbitals in  $\text{Be}_4\text{O}$  being of  $\pi_u$  and  $\pi_g$  symmetry. The onset of electrons has also slightly moved up, with start of substantial signal now being at roughly  $10200\text{ cm}^{-1}$ . It is also worth mentioning that  $\text{Be}_4\text{O}$  was by far the most difficult cluster to produce of those listed in this section, which may suggest that it has the tendency to dissociate into the smaller clusters, but this possibility is only speculation at this time and should be investigated theoretically once a proper treatment of these clusters has been established.

$\text{Be}_5\text{O}$  was found to be an easy to produce cluster, with signal comparable to

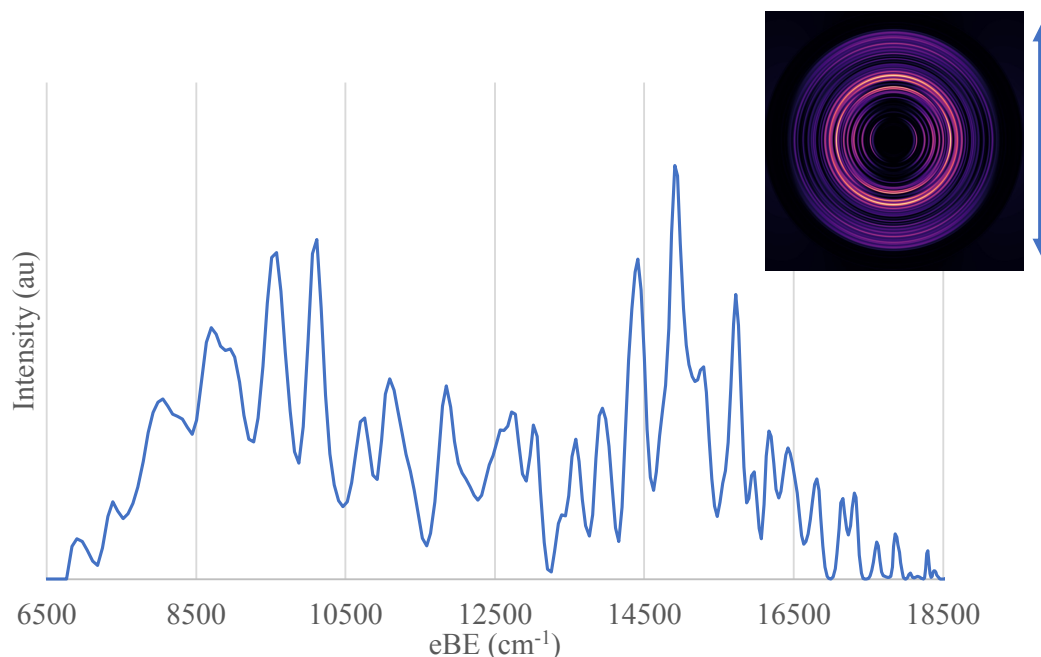


Figure 6.7:  $18797 \text{ cm}^{-1}$  photodetachment spectrum of  $\text{Be}_3\text{O}$ . Inset image shows the velocity map image produced by MEVELER [45], and laser polarization is shown by the double headed arrow.

$\text{BeO}$  under the optimal conditions. It is unclear if this is due to dissociation from a larger cluster, or if  $\text{Be}_5\text{O}$  is simply a strongly bound system by itself. The survey spectrum of  $\text{Be}_5\text{O}$  is shown in Figure 6.9. Strong photodetachment signal is present above  $13500 \text{ cm}^{-1}$ . This jump in photoelectron onset, compared with those in the previous clusters, along with the increase in signal in this cluster suggests a change in character at this point. Although there is not a clear onset of metallic character, if we as the authors were to place bets on where these clusters cross the metallic threshold, we would bet on  $\text{Be}_5\text{O}$ . Additionally there is a mix of perpendicular and parallel anisotropy, which may imply some excited anion states being present in the spectrum if our computations are to be trusted.

The  $\text{Be}_6\text{O}$ ,  $\text{Be}_7\text{O}$ , and  $\text{Be}_8\text{O}$  clusters' survey photoelectrons are shown in Figures 6.10, 6.11, and 6.12 respectively.  $\text{Be}_6\text{O}$  shows a reasonable bump in energy from  $\text{Be}_5\text{O}$  for the onset of photoelectrons, with the high intensity peak being at an eBE of approximately  $15700 \text{ cm}^{-1}$ . The photoelectron angular distribution shows both

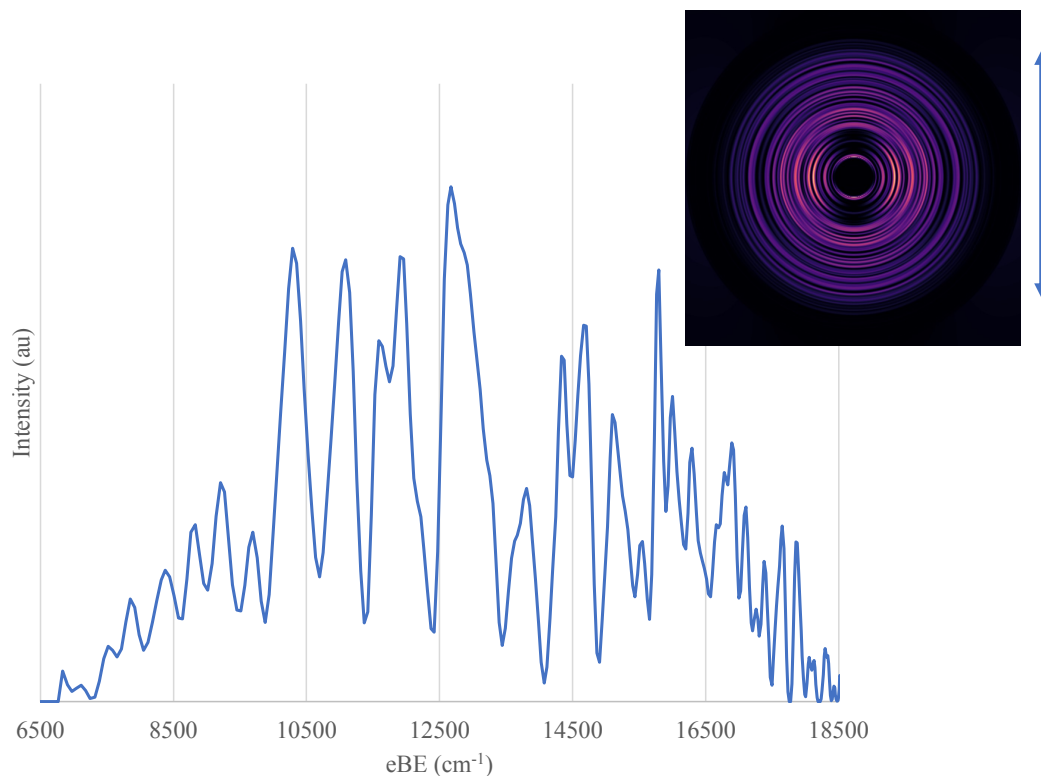


Figure 6.8:  $18797 \text{ cm}^{-1}$  photodetachment spectrum of  $\text{Be}_4\text{O}$ . Inset image shows the velocity map image produced by MEVELER [45], and laser polarization is shown by the double headed arrow.

parallel and perpendicular transitions. The small peaks below  $12000 \text{ cm}^{-1}$  are reasonably repeatable, but do not always repeat in different spectra, which implies the existence of meta stable anionic states, or potential fast dissociation into smaller anion clusters that are then photodetached.  $\text{Be}_7\text{O}$  shows a small increase in detachment onset, with the large peak being located at  $16700 \text{ cm}^{-1}$ , which begins to mark a potential tapering off of the increase in electron binding energy. The PAD change between perpendicular and parallel is much more obvious in  $\text{Be}_7\text{O}$ , with the peaks to the left of the largest peak having mostly parallel character and those to the right having mostly perpendicular character.

$\text{Be}_8\text{O}$  has perhaps the most interesting survey spectrum, as it shows a strong transition at approximately  $13000 \text{ cm}^{-1}$ , a moderate transition at  $8950 \text{ cm}^{-1}$  and then a large number of transitions centered at approximately  $16500 \text{ cm}^{-1}$ . Additionally,

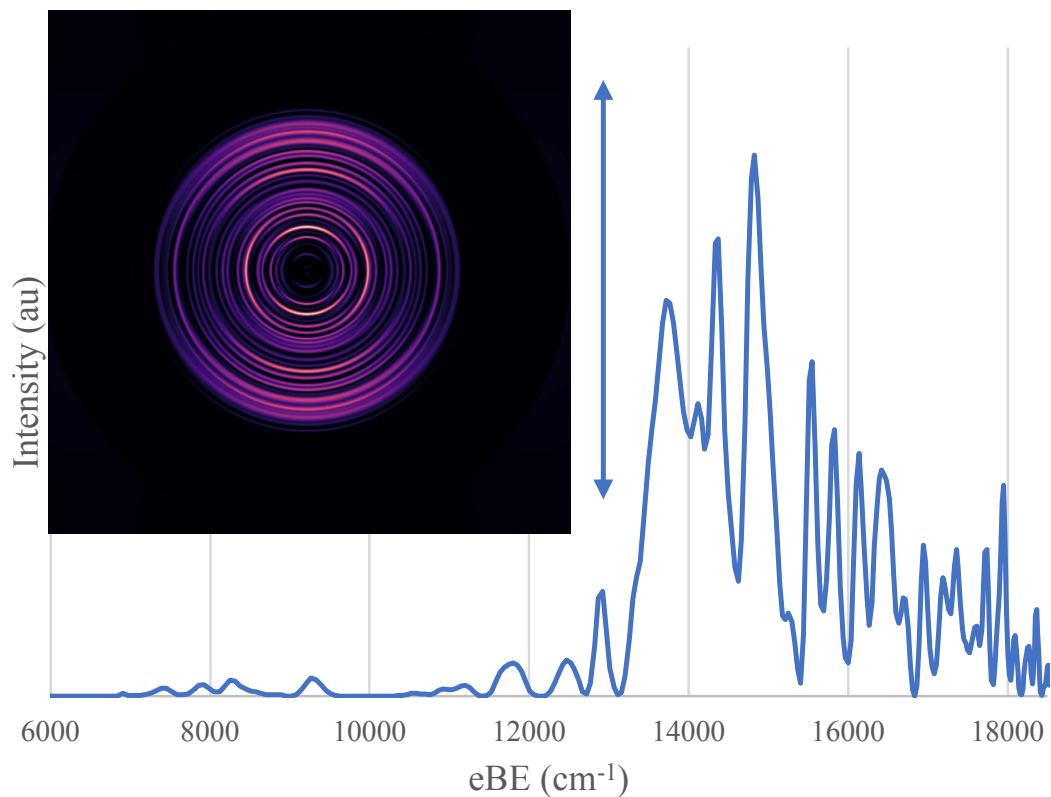


Figure 6.9:  $18797 \text{ cm}^{-1}$  photodetachment spectrum of  $\text{Be}_5\text{O}$ . Inset image shows the velocity map image produced by MEVELER [45], and laser polarization is shown by the double headed arrow.

there is little spectral congestion around the lower energy peaks and in the  $14000$  to  $16000 \text{ cm}^{-1}$  range with the exception of the peak at  $15300 \text{ cm}^{-1}$ . This may imply the existence of a few anion excited states, but the lack of congestion suggests that the spectra anions were reasonably well cooled. Alternatively, its possible that the large group of intense transitions above  $16000 \text{ cm}^{-1}$  are an excited state manifold and the  $8950 \text{ cm}^{-1}$  or  $13000 \text{ cm}^{-1}$  peak is the electron affinity, but this would be a major shift from our expectations and the trend in the prior clusters of an increasing electron affinity.

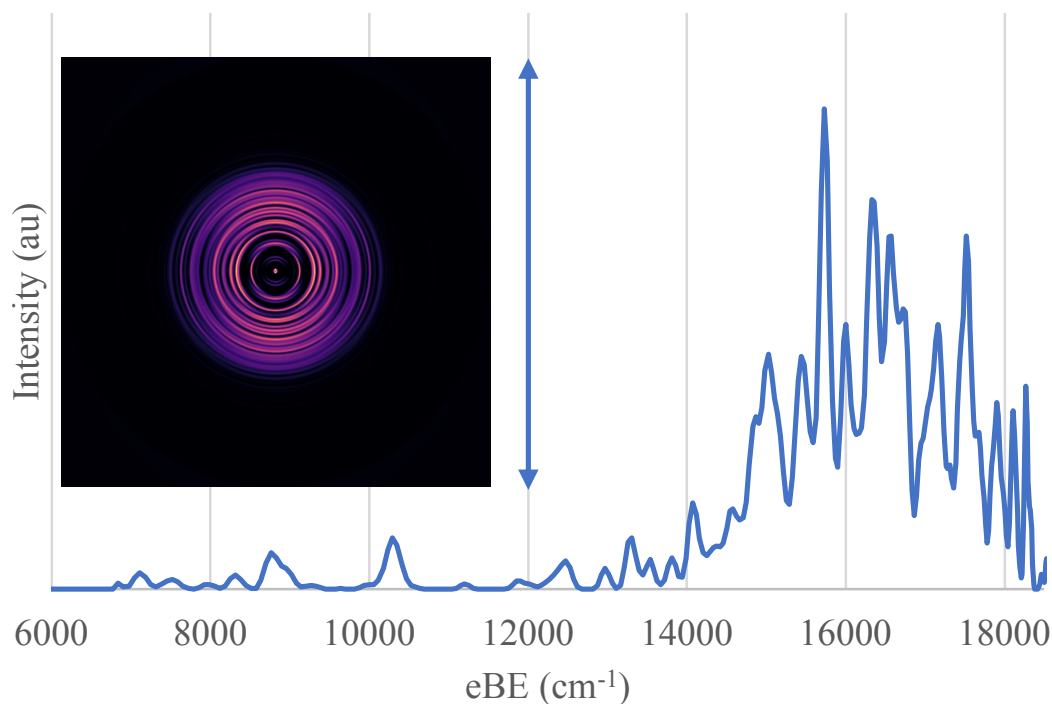


Figure 6.10:  $18797\text{ cm}^{-1}$  photodetachment spectrum of  $\text{Be}_6\text{O}$ . Inset image shows the velocity map image produced by MEVELER [45], and laser polarization is shown by the double headed arrow.

## 6.5 Conclusions and Ongoing work

Anion photoelectron spectra of the hyperberyllium  $\text{Be}_n\text{O}$  ( $n=2,3,\dots,8$ ) series have been recorded and presented for the first time. Exact understanding of even the smaller clusters is hampered by the lack of reliable computation, but these clusters show dramatically non monotonic behavior and increases in complexity with increasing size. Further study of these clusters should focus on multireference based theoretical approaches, as our single reference approaches showed hallmark signs of multireference behavior. Additionally, the singlet triplet gap in  $\text{BeOBe}$ , the value of which has long been a point of contention in the theoretical community, has been observed and given an experimentally determined value of  $147(12)\text{ cm}^{-1}$ . The EA of  $\text{BeOBe}$  was also experimentally determined and assigned a value of  $9583(60)\text{ cm}^{-1}$ .

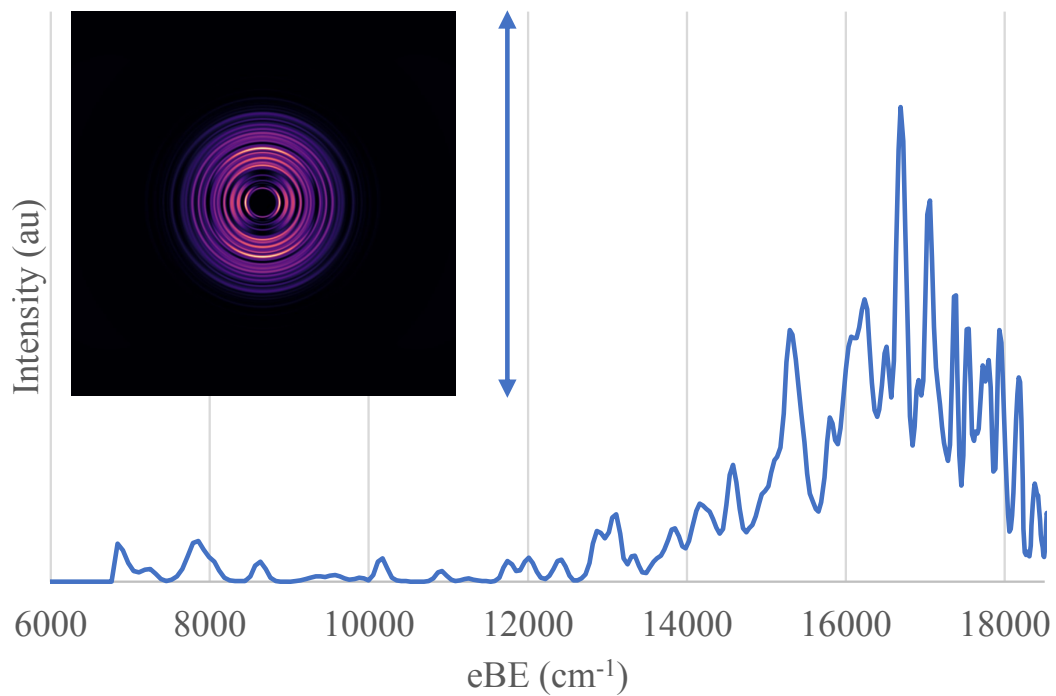


Figure 6.11: 18797 cm<sup>-1</sup> photodetachment spectrum of Be<sub>7</sub>O. Inset image shows the velocity map image produced by MEVELER [45], and laser polarization is shown by the double headed arrow.

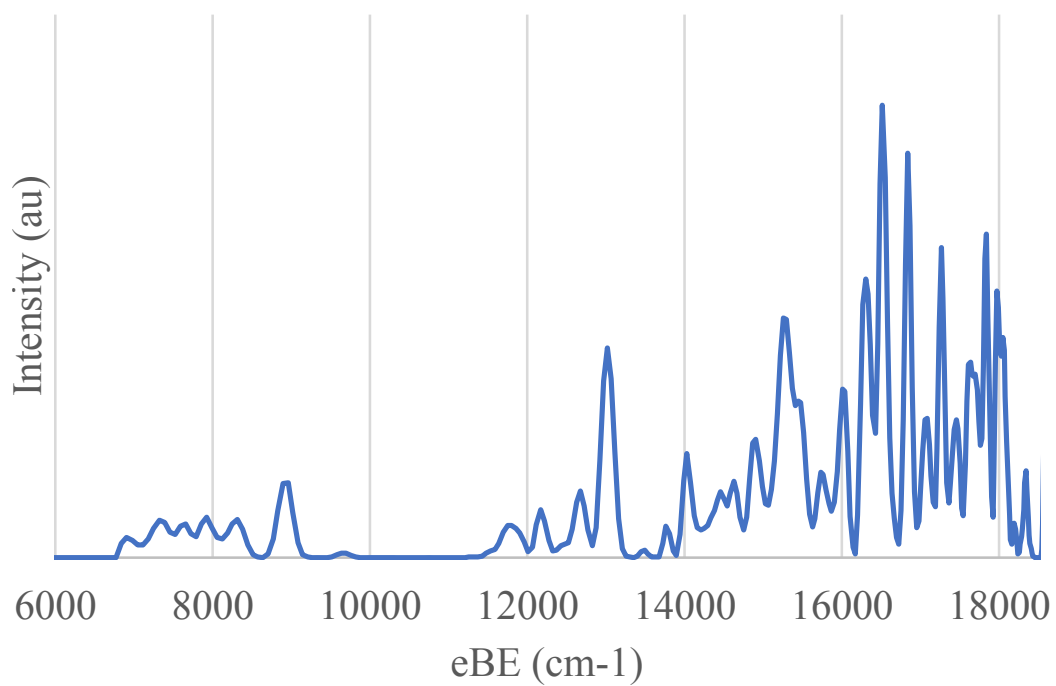


Figure 6.12: 18797 cm<sup>-1</sup> photodetachment spectrum of Be<sub>8</sub>O.

## Chapter 7

# The Broken, The Beaten, The Damned: Preliminary Works and Unsuccessful Attempts on Other Molecules

Over the years of this PhD, a number of molecules were attempted that did not yield sufficiently good results to warrant publication, but may be revisited if upgrades to the apparatus were to be made. This could be due to an inherent difficulty with the molecular system, poor generation conditions, or any other number of problems. These molecules are reviewed here, along with any information that may be useful to future students.



## 7.1 Beryllium Oxides

### 7.1.1 Be<sub>2</sub>O<sub>2</sub>

Be<sub>2</sub>O<sub>2</sub> was generated under laser ablation conditions with a mix of 0.75% N<sub>2</sub>O and 0.5% O<sub>2</sub> in argon backing gas. Signal for this species was weak and somewhat intermittent, and needs further optimization. Photodetachment spectra show activity in the range from approximately 13000 cm<sup>-1</sup> up to 17500 cm<sup>-1</sup>, but initial spectra were rather hot and dense. One of these sample spectra is given in Figure 7.1. Optimization of expansion cooling, or addition of other cooling methods should be attempted in subsequent studies, in addition to a search for better generation conditions.

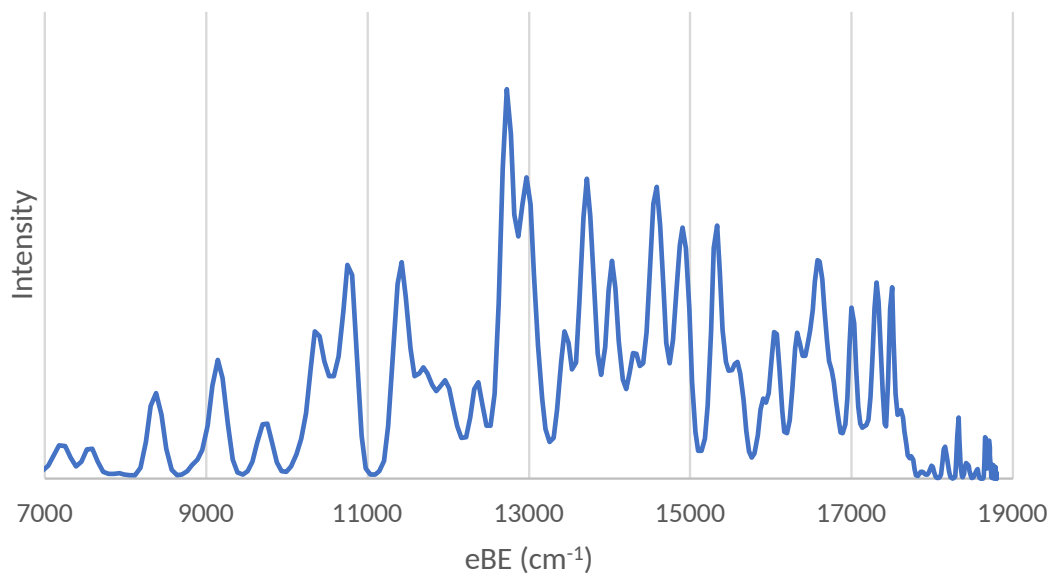


Figure 7.1: A survey spectrum of Be<sub>2</sub>O<sub>2</sub> using 18797 cm<sup>-1</sup> detachment photons.

### 7.1.2 OBeO

OBeO was generated under laser ablation conditions with a mix of 0.75% N<sub>2</sub>O and 0.5% O<sub>2</sub> in argon backing gas. Signal proved reasonably strong, but SEVI spectra showed dense structure (Figure 7.2) consistent with hot anions from 20000 cm<sup>-1</sup> up to the detachment energy of 28169 cm<sup>-1</sup> (355 nm). The spectra were also notably

dense in the range from  $26000\text{ cm}^{-1}$  to  $28000\text{ cm}^{-1}$ , with the fall off in intensity above  $28000\text{ cm}^{-1}$  likely due to threshold behavior rather than a decrease in spectral density. A slightly higher photodetachment energy and better cooling conditions may result in more interpretable spectra, but the short wavelengths needed to detach this species will readily scatter electrons from the chamber if the photodetachment laser is poorly aligned.

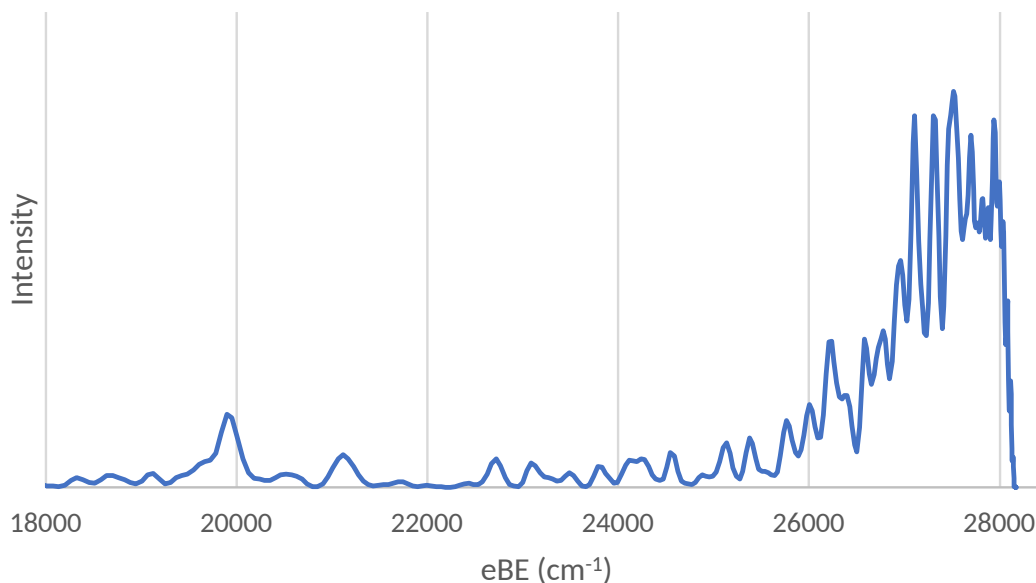


Figure 7.2: A survey spectrum of  $\text{BeO}_2$  using  $28169\text{ cm}^{-1}$  detachment photons.

## 7.2 SBeS

$\text{BeS}_2$  and  $\text{BeS}_2^-$  were attempted using SEVI spectroscopy and *ab initio* computational methods. Anions were generated by pulsed ablation of a rotating and translating beryllium rod in a vapor pressure  $\text{CS}_2$  seeded helium buffer gas using the fundamental output (1064nm) of an Nd:YAG Minilite Laser. The gas is pulsed during ablation by an Even-Lavie [36] style pulsed valve. Anions are mass selected and photodetached using the 3rd and 4th harmonics of an Nd:YAG (355nm, 266nm) or an excimer pumped dye laser (360nm-405nm). Both lasers are vertically polarized

during all experiments. Images were recorded before the development of our current shot discrimination software, and should be retaken in subsequent studies.

Calculations have been performed at varying levels of theory using the Psi4 computational package [98]. Unless otherwise specified all computations were performed on geometries optimized at the CCSD(T) level of theory using an aug-cc-pVTZ basis set. The CCSD(T) optimized geometry parameters for each geometry and the corresponding state, as well as the energy relative to the predicted ground state is given in Table 7.1. While the previously predicted  $^3\Sigma^-$  is the lowest energy linear conformation, our calculations revealed a  $C_{2v}$  conformation  $1391\text{ cm}^{-1}$  lower in energy. Of additional interest is that the  $^3\Sigma^-$  state is of  $C_{\infty v}$  rather than  $D_{\infty h}$  symmetry as may be expected, implying some sort of pseudo Renner-Teller effect. A similar symmetry breaking occurs in what would be the corresponding  $^1\Sigma^+$  state, where a very slight bend occurs to break the symmetry, rather than a change in bond lengths. This reduces what would be a  $D_{\infty h}$  symmetry to a near linear  $C_{2v}$  symmetry. The difference between the singlet slight bent  $C_{2v}$  and  $D_{\infty h}$  is very small, approximately  $100\text{ cm}^{-1}$  at the CCSD(T) level, so it is currently unclear if the bent here is truly lower in energy or if it is a computational artifact due to a flat potential, and further calculations are required to determine this more definitively.

Additionally, to better determine the stability of each geometry, angular potential energy cuts were taken at varying levels of theory between  $60^\circ$  and  $180^\circ$  for the singlet neutral and between  $50^\circ$  and  $180^\circ$  for the triplet neutral and doublet anion (Figure 7.4 and 7.5). Interestingly, the level of theory used substantially changes the apparent ordering of states. At the MP2 and CCSD levels of theory, the ordering of states in the triplet is flipped with the bent geometry being the lower energy state and linear being higher energy. The perturbative triples correction, which is much larger in the linear triplet species, flips the state ordering and moves the linear below the bent. The discontinuity was not analyzed in depth but is likely due to issues with the

SCF wavefunction being incorrectly selected in the range around  $65^\circ$ , and the state symmetry of the bent and linear changing in this region.

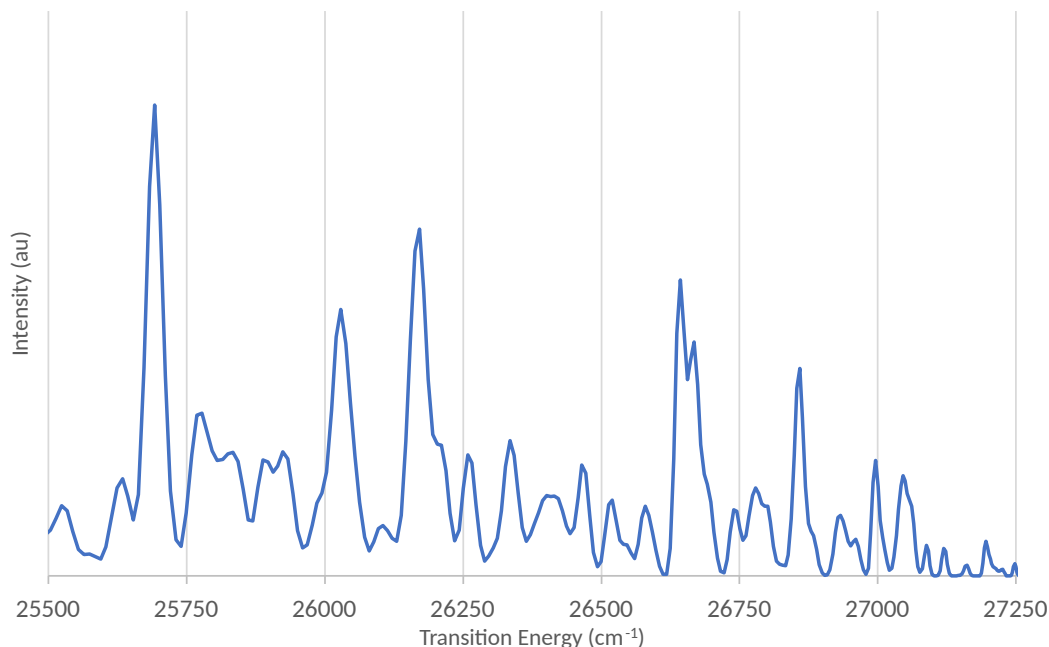


Figure 7.3: A photoelectron spectrum of  $\text{BeS}_2$  using  $27322 \text{ cm}^{-1}$  detachment photons.

In the singlet states, at the CCSD(T) level there is a barrier of approximately  $3000 \text{ cm}^{-1}$  between the near linear and bent states. The near linear conformation had a substantially smaller triples correction than the bent conformation, which is surprising as the T1 diagnostic of the linear conformation is much higher (0.030 vs 0.013 in the bent). Normally this would imply that the multireference character is high, and higher-level corrections should be large as the higher order excitations in the couple cluster scheme tend to recover some of this character. Because this T1 diagnostic was so high, additional computations were performed using the multireference Mk-MRCCSD(T) formalism. Surprisingly the Mk-MRCCSD(T) energy for the linear singlet was the same to  $10^{-8}$  Hartree as the non-multireference CCSD(T). When the bent singlet energy was computed via Mk-MRCCSD(T), the energy was lower by approximately  $1.2 \times 10^{-5}$  Hartree when compared to CCSD(T). Multi-reference computations may be useful in this system, but were not attempted beyond this.

The anion doublet acts somewhat similarly to the triplet, where the lower levels of theory predict the two geometries to be very close in energy, and higher-level corrections predicting the linear geometry to be lower in energy. The anion also has the same discontinuity as the triplet, although further analysis is needed to determine the cause of this sharp transition. While all methods qualitatively show similar potential curves for the neutral singlet species, in the neutral triplet and anion only the couple cluster methods recover a similar picture.

$\text{BeS}_2^-$  spectra were gathered but proved to be dense and not substantially repeatable with the methods in use at the time. An example spectra is given in Figure 7.3. It is possible that this species could be reattempted using signal discrimination, which had not been implemented when the original study was attempted. Additionally, EOMEA methods likely treat the anion better than open shell coupled cluster, and should be attempted.

Table 7.1: SBeS CCSD(T)/aug-cc-pVTZ Computation Results

Species	Point Group	State	$E_{rel}$ ( $\text{cm}^{-1}$ )	$r_{BeS}$ ( $\text{\AA}$ )	$\angle_{SBeS}$ ( $^\circ$ )
$\text{BeS}_2$	$C_{2v}$	$^3A_2$	6084	2.01	60.6
	$D_{\infty h}$	$^1\Sigma_g^+$	1712	1.91	180.0
	$D_{\infty h}$	$^3\Sigma_g^-$	1391	1.89	180.0
	$C_{2v}$	$^1A_1$	26187 (EA)	1.85	75.2
$\text{BeS}_2^-$	$C_{2v}$	$^2A_1$	10277	1.96	66.9
	$D_{\infty h}$	$^2\Pi_g$	0	1.87	180

## 7.3 Beryllium Nitrides

### 7.3.1 BeN

Several attempts at creating BeN in our apparatus have been attempted, without success. Previous attempts using gaseous reactant mixes and a bomb filled with

a nitrogen based reactant have yielded unsubstantial or otherwise negligible signal, which is surprising as the BeN anion is expected to be a closed shell and reasonably happy beast. To date we have attempted using  $\text{NO}_2$ ,  $\text{N}_2\text{O}$ ,  $\text{N}_2$ ,  $\text{NH}_3$ , and  $\text{CH}_3\text{CN}$  to no avail. Creating this anion by ‘standard’ laser ablation methods is a task that should only be undertaken by the most deranged or determined of graduate students. To those deranged graduate students, I wish you good luck, and the following methods are those I would attempt.

First, and safest, would be to attempt to nitride a beryllium rod. To the best of my knowledge this has not been attempted in the traditional nitriding process that has been done with steel for decades, which relies on using a heated and pressurized vessel full of  $\text{NH}_3$  with steel parts inside. The heating releases free hydrogen and nitrogen which reacts with oxygen on the steel surface, replacing it with nitrogen and water vapor in the vessel rather than ammonia. This could be attempted on a small scale using a pressure rated pipe full of  $\text{NH}_3$  and  $\text{N}_2$ , with a Be rod placed inside before being sealed and heated, but it is unclear if this would work effectively, and heating pressurized vessels full of ammonia is a decision that would be best described as bold. Be nitriding using high energy nitrogen plasma has been reported in the literature, and could be another method, albeit one with substantially more cost and equipment needed [99, 100]. Another study was able to produce Be nitride thin films with the formal molecular formula  $\text{Be}_3\text{N}_2$  via laser ablation in a nitrogen environment as well [101].

Second, and potentially more dangerously, would be to attempt using a reactant with lots of nitrogen that are tenuously bound together as your reactant for the ablation process. Fortunately, there is an entire field of research which focuses on the synthesis and analysis of tenuously bound nitrogen heavy molecules. Unfortunately, that field is explosives synthesis, and most of these compounds are high explosives [102]. The most promising molecules for our use would be some type of nitrotetrazol

in solution, but the solubility of many of these nitrotetrazols in solvents that are acceptable for our experiment is somewhat difficult to find. While many of these can be safe in solution phase, often the solutions they are held in are strong acids which may damage the pulse valve or other sensitive parts which must be avoided.

### 7.3.2 Be<sub>3</sub>N

Our attempts to create BeN instead generated signal for NBe<sub>3</sub><sup>-</sup> which we believe to be a D<sub>3h</sub> planar molecule with Be-N bond lengths of approximately 1.5Å. While the full parameter space of reactants was not investigated, a 0.75% N<sub>2</sub>O mix in argon gave consistent, if low, signal. Initial EOMEA CCSD computations give an electron affinity estimate of approximately 8100 cm<sup>-1</sup>. It seems incredibly likely that the ground state neutral is a <sup>4</sup>E' or <sup>2</sup>E' state that would be subject to Jahn-Teller distortion, but an in depth *ab initio* study was not performed. A cursory glance at the CCSD wavefunction suggests that this is a problem that is well approximated by single reference methods, and may be a good candidate for study by EOM-CC methods.

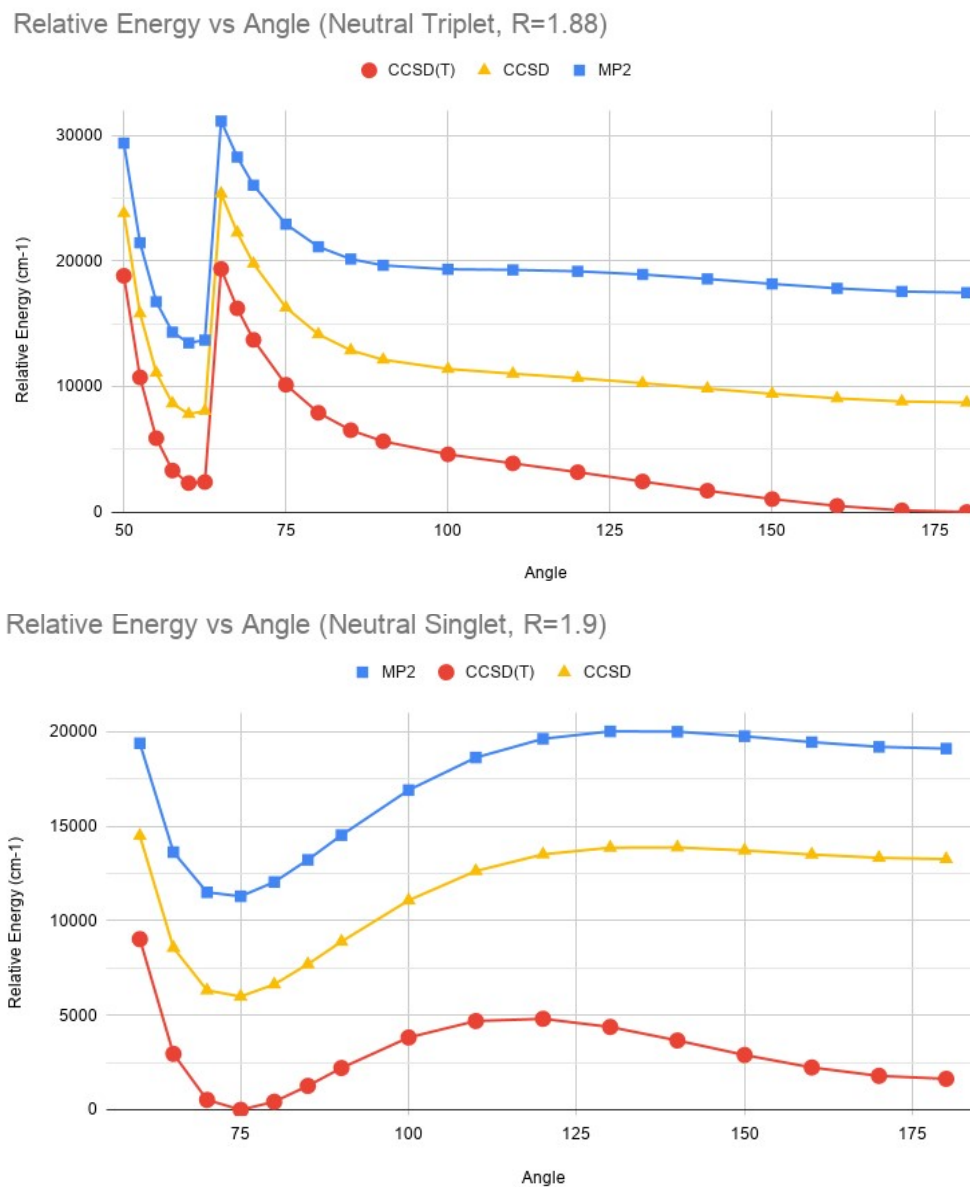


Figure 7.4: Potential energy cuts across the SBeS singlet and triplet ground states along the bending coordinate at three levels of theory with constant bond length. Discontinuities are believed to be due to the switching of state symmetries between the ground state bent and linear conformations



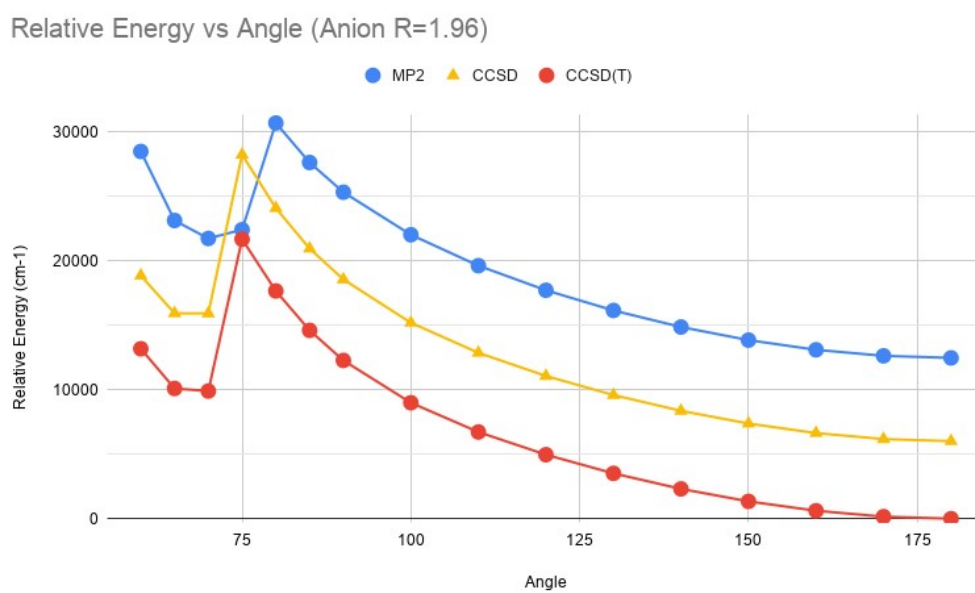


Figure 7.5: Potential energy cuts across the  $\text{SBeS}^-$  doublet ground state along the bending coordinate at three levels of theory with constant bond length. Discontinuities are believed to be due to the switching of state symmetries between the ground state bent and linear conformations

## Chapter 8

**When One Door Closes:**

**Conclusions and Future Direction**

In order to better understand chemical bonding, both in general and in the special case of beryllium containing molecules, a number of beryllium containing anions were studied by Slow Electron Velocity-Map Imaging. These studies provided a wealth of information on these poorly characterized systems, as well as new data with which to benchmark future methods of electronic structure computation. With the exception of the BeOBe molecule, none of the species presented here have previously had their electronic structure examined by experimental methods. While our own computational predictions were generally acceptable for pure Be clusters, the beryllium hyper-metallic oxides have been shown to be species with incredibly dense spectral structure that are not well characterized by single reference methods. These hyper-metallic oxides represent an understudied region even in beryllium literature, and should be investigated by higher level multireference methods.

In addition, new software designed for this experiment has expanded the size of systems we can study using this apparatus. While the previous size record prior to this software upgrade was the triatomic  $\text{BeC}_2$  anion, the new record is the  $\text{Be}_8\text{O}$  anion with nine atoms total. This jump in size is substantial, and will only be even further raised following the addition of a cryogenic ion trap. The inclusion of such a trap would be a massive boon, and may allow better understanding of the denser spectra presented here, and as such should be completed as soon as feasible.

## References

- (1) Merritt, J. M.; Bondybey, V. E.; Heaven, M. C. *Science* **2009**, *324*, 1548–51.
- (2) Kaledin, L. A.; Kaledin, A. L.; Heaven, M. C.; Bondybey, V. E. *Journal of Molecular Structure: THEOCHEM* **1999**, *461-462*, 177–186.
- (3) Evangelisti, S.; Bendazzoli, G. L.; Gagliardi, L. *Chemical Physics* **1994**, *185*, 47–56.
- (4) Zhao, Y.; Li, S.; Xu, W.-G.; Li, Q.-S. *The Journal of Physical Chemistry A* **2004**, *108*, 4887–4894.
- (5) Rao, B. K.; Khanna, S. N.; Meng, J.; Jena, P. *Zeitschrift fr Physik D Atoms, Molecules and Clusters* **1991**, *18*, 171–174.
- (6) Cai, Z. X.; Mahanti, S. D.; Antonelli, A.; Khanna, S. N.; Jena, P. *Phys Rev B Condens Matter* **1992**, *46*, 7841–7845.
- (7) Shinde, R.; Tayade, M. *The Journal of Physical Chemistry C* **2014**, *118*, 17200–17204.
- (8) Srinivas, S.; Jellinek, J. *J Chem Phys* **2004**, *121*, 7243–52.
- (9) Abyaz, B.; Mahdavifar, Z.; Schreckenbach, G.; Gao, Y. *Phys Chem Chem Phys* **2021**, *23*, 19716–19728.
- (10) Liu, Q.; Hu, Y.; Zhang, X.; Wang, F.; Cheng, L. *Chemical Physics* **2021**, *542*, DOI: 10.1016/j.chemphys.2020.111055.

- (11) Wang, J.; Wang, G.; Zhao, J. *Journal of Physics: Condensed Matter* **2001**, *13*, L753–L758.
- (12) Cerowski, V.; Rao, B. K.; Khanna, S. N.; Jena, P.; Ishii, S.; Ohno, K.; Kawazoe, Y. *J Chem Phys* **2005**, *123*, 074329.
- (13) Kawai, R.; Weare, J. H. *Phys Rev Lett* **1990**, *65*, 80–83.
- (14) Green, M. L.; Jaffe, N. B.; Heaven, M. C. *J Phys Chem Lett* **2020**, *11*, 88–92.
- (15) Green, S. *Chemical Physics Letters* **1984**, *112*, 29–32.
- (16) Heaven, M. C.; Merritt, J. M.; Bondybey, V. E. *Annual Review of Physical Chemistry* **2011**, *62*, PMID: 21219142, 375–393.
- (17) Beyer, M. K.; Kaledin, L. A.; Kaledin, A. L.; Heaven, M. C.; Bondybey, V. E. *Chemical Physics* **2000**, *262*, 15–23.
- (18) Merritt, J. M.; Bondybey, V. E.; Heaven, M. C. *J Phys Chem A* **2009**, *113*, 13300–9.
- (19) Antonov, I. O.; Barker, B. J.; Bondybey, V. E.; Heaven, M. C. *J Chem Phys* **2010**, *133*, 074309.
- (20) Antonov, I. O.; Barker, B. J.; Heaven, M. C. *The Journal of Chemical Physics* **2011**, *134*, 044306.
- (21) Mascaritolo, K. J.; Dermer, A. R.; Green, M. L.; Gardner, A. M.; Heaven, M. C. *J Chem Phys* **2017**, *146*, 054301.
- (22) Dermer, A. R.; Green, M. L.; Mascaritolo, K. J.; Heaven, M. C. *J Phys Chem A* **2017**, *121*, 5645–5650.
- (23) Green, M. L.; Jean, P.; Heaven, M. C. *J Phys Chem Lett* **2018**, *9*, 1999–2002.
- (24) Kuyatt, C. E.; Simpson, J. A. *Review of Scientific Instruments* **2004**, *38*, 103–111.
- (25) Brehm, B.; Gusinow, M. A.; Hall, J. L. *Phys. Rev. Lett.* **1967**, *19*, 737–741.

- (26) Posey, L. A.; Deluca, M. J.; Johnson, M. A. *Chemical Physics Letters* **1986**, *131*, 170–174.
- (27) Wang, L.-S.; Ding, C.-F.; Wang, X.-B.; Barlow, S. E. *Review of Scientific Instruments* **1999**, *70*, 1957–1966.
- (28) Kitsopoulos, T.; Waller, I.; Loeser, J.; Neumark, D. *Chemical Physics Letters* **1989**, *159*, 300–306.
- (29) Eppink, A. T. J. B.; Parker, D. H. *Review of Scientific Instruments* **1997**, *68*, 3477–3484.
- (30) Sanov, A. *Annual Review of Physical Chemistry* **2014**, *65*, PMID: 24423373, 341–363.
- (31) Cooper, J.; Zare, R. N. *The Journal of Chemical Physics* **1968**, *48*, 942–943.
- (32) Anstöter, C. S.; Verlet, J. R. R. *The Journal of Physical Chemistry A* **2021**, *125*, 4888–4895.
- (33) Osterwalder, A.; Nee, M. J.; Zhou, J.; Neumark, D. M. *The Journal of Chemical Physics* **2004**, *121*, 6317–6322.
- (34) Mascaritolo, K., *A Journey towards the Construction and Operation of a Photoelectron Velocity-Map Imaging Spectrometer*.
- (35) Green, M., *Understanding the chemistry of beryllium using photoelectron velocity map imaging spectroscopy*.
- (36) Even, U. *EPJ Techniques and Instrumentation* **2015**, *2*, 17.
- (37) Wiley, W. C.; McLaren, I. H. *Review of Scientific Instruments* **1955**, *26*, 1150–1157.
- (38) Lu, Y.-J.; Lehman, J. H.; Lineberger, W. C. *The Journal of Chemical Physics* **2015**, *142*, 044201.
- (39) Duncan, M. A. *Review of Scientific Instruments* **2012**, *83*, 041101.

- (40) Hayes, J. M.; Small, G. J. *Analytical Chemistry* **1983**, *55*, 565A–574A.
- (41) Merritt, J. M.; Bondybey, V. E.; Heaven, M. C. *Phys. Chem. Chem. Phys.* **2008**, *10*, 5403–5411.
- (42) Persinger, T. D.; Han, J.; Heaven, M. C. *The Journal of Physical Chemistry A* **2021**, *125*, 8274–8281.
- (43) Persinger, T. D.; Han, J.; Heaven, M. C. *The Journal of Physical Chemistry A* **2021**, *125*, 3653–3663.
- (44) Mascaritolo, K. J.; Gardner, A. M.; Heaven, M. C. *The Journal of Chemical Physics* **2015**, *143*, 114311.
- (45) Dick, B. *Phys. Chem. Chem. Phys.* **2014**, *16*, 570–580.
- (46) DeWitt, M.; Babin, M. C.; Lau, J. A.; Solomis, T.; Neumark, D. M. *The Journal of Physical Chemistry A* **2022**, *126*, PMID: 36269316, 7962–7970.
- (47) Ballard, D. *Pattern Recognition* **1981**, *13*, 111–122.
- (48) .
- (49) Hickstein, D. D.; Gibson, S. T.; Yurchak, R.; Das, D. D.; Ryazanov, M. *Review of Scientific Instruments* **2019**, *90*, 065115.
- (50) Jaffe, N. B.; Stanton, J. F.; Heaven, M. C. *The Journal of Physical Chemistry Letters* **2023**, *14*, PMID: 37699253, 8339–8344.
- (51) Kolchin, A. M.; Hall, R. W. *The Journal of Chemical Physics* **2000**, *113*, 4083–4092.
- (52) Khanna, S. N.; Reuse, F.; Buttet, J. *Phys Rev Lett* **1988**, *61*, 535–538.
- (53) Sudhakar, P. V.; Lammertsma, K. *The Journal of Chemical Physics* **1993**, *99*, 7929–7937.
- (54) Kalemos, A. *Chemical Physics Letters* **2020**, *739*, DOI: 10.1016/j.cplett.2019.136964.

- (55) Thomas, O. C.; Zheng, W.; Xu, S.; Bowen K. H., J.; Shiloh, M. *Phys Rev Lett* **2002**, *89*, 213403.
- (56) Middleton, R.; Klein, J. *Physical Review A* **1999**, *60*, 3786–3799.
- (57) Jordan, K. D.; Simons, J. *The Journal of Chemical Physics* **1977**, *67*, 4027–4037.
- (58) Matthews, D. A.; Cheng, L.; Harding, M. E.; Lipparini, F.; Stopkowicz, S.; Jagau, T.-C.; Szalay, P. G.; Gauss, J.; Stanton, J. F. *The Journal of Chemical Physics* **2020**, *152*, 214108.
- (59) Prascher, B. P.; Woon, D. E.; Peterson, K. A.; Dunning, T. H.; Wilson, A. K. *Theor. Chem. Acc.* **2011**, *128*, 69–82.
- (60) Lee, T. J.; Rendell, A. P.; Taylor, P. R. *The Journal of Physical Chemistry* **2002**, *94*, 5463–5468.
- (61) Kowalski, K.; Piecuch, P. *The Journal of Chemical Physics* **2001**, *115*, 643–651.
- (62) Nooijen, M.; Bartlett, R. J. *The Journal of Chemical Physics* **1995**, *102*, 3629–3647.
- (63) Stanton, J. F.; Bartlett, R. J. *The Journal of Chemical Physics* **1993**, *98*, 7029–7039.
- (64) Kucharski, S.; Wloch, M.; Monika, M.; Bartlett, R. J. *The Journal of Chemical Physics* **2001**, *115*, 8263–8266.
- (65) Rendell, A. P.; Lee, T. J.; Taylor, P. R. *The Journal of Chemical Physics* **1990**, *92*, 7050–7056.
- (66) Diaz, C. C.; Kaplan, I. G.; Roszak, S. *J Mol Model* **2005**, *11*, 330–4.
- (67) Ascik, P. N.; Rugango, R.; Simmonett, A. C.; Compaan, K. R.; Schaefer III, H. F. *ChemPhysChem* **2012**, *13*, 1255–1260.



- (68) Poater, J.; Solà, M. *Chem. Commun.* **2019**, *55*, 5559–5562.
- (69) Lu, T.; Chen, F. *Journal of Computational Chemistry* **2012**, *33*, 580–592.
- (70) LU Tian, C. F.-W. *Acta Physico-Chimica Sinica* **2011**, *27* 2786, 2786.
- (71) Bader, R. F. W. *Accounts of Chemical Research* **1985**, *18*, 9–15.
- (72) Becke, A. D.; Edgecombe, K. E. *The Journal of Chemical Physics* **1990**, *92*, 5397–5403.
- (73) Silvi, B.; Savin, A. *Nature* **1994**, *371*, 683–686.
- (74) Terrabuio, L. A.; Teodoro, T. Q.; Rachid, M. G.; Haiduke, R. L. A. *The Journal of Physical Chemistry A* **2013**, *117*, PMID: 24020914, 10489–10496.
- (75) Alcoba, D. R.; Lain, L.; Torre, A.; Bochicchio, R. C. *Chemical Physics Letters* **2005**, *407*, 379–383.
- (76) Gatti, C.; Fantucci, P.; Pacchioni, G. *Theoretica chimica acta* **1987**, *72*, 433–458.
- (77) Zhao, Y.; Li, S.; Xu, W.-G.; Li, Q.-S. *The Journal of Physical Chemistry A* **2004**, *108*, 4887–4894.
- (78) W., B. R. F., *Atoms in molecules: A quantum theory*; Clarendon: 2003.
- (79) Iversen, B. B.; Larsen, F. K.; Souhassou, M.; Takata, M. *Acta Crystallographica Section B* **1995**, *51*, 580–591.
- (80) Platts, J. A.; Overgaard, J.; Jones, C.; Iversen, B. B.; Stasch, A. *The Journal of Physical Chemistry A* **2011**, *115*, PMID: 21158464, 194–200.
- (81) Babin, M. C.; DeVine, J. A.; DeWitt, M.; Stanton, J. F.; Neumark, D. M. *The Journal of Physical Chemistry Letters* **2020**, *11*, PMID: 31765169, 395–400.
- (82) Kawaguchi, K.; Ishiwata, T.; Hirota, E.; Tanaka, I. *Chemical Physics* **1998**, *231*, 193–198.

- (83) Stanton, J. F.; Okumura, M. *Phys. Chem. Chem. Phys.* **2009**, *11*, 4742–4744.
- (84) Stanton, J. F.; Gauss, J.; Bartlett, R. J. *The Journal of Chemical Physics* **1991**, *94*, 4084–4087.
- (85) Chappuis, J. *Annales scientifiques de l'École Normale Supérieure* **1882**, *2e série*, *11*, 137–186.
- (86) Theard, L. P.; Hildenbrand, D. L. *The Journal of Chemical Physics* **1964**, *41*, 3416–3420.
- (87) Boldyrev, A. I.; Simons, J. *The Journal of Physical Chemistry* **1995**, *99*, 15041–15045.
- (88) Thompson, C. A.; Andrews, L. *The Journal of Chemical Physics* **1994**, *100*, 8689–8699.
- (89) Ostojić, B.; Bunker, P. R.; Schwerdtfeger, P.; Assadollahzadeh, B.; Jensen, P. *Phys. Chem. Chem. Phys.* **2011**, *13*, 7546–7553.
- (90) Ostojić, B.; Jensen, P.; Schwerdtfeger, P.; Bunker, P. *Journal of Molecular Spectroscopy* **2014**, *301*, 20–24.
- (91) Ostojić, B.; Jensen, P.; Schwerdtfeger, P.; Assadollahzadeh, B.; Bunker, P. *Journal of Molecular Spectroscopy* **2010**, *263*, 21–26.
- (92) Ostojić, B.; Bunker, P.; Schwerdtfeger, P.; Gertych, A.; Jensen, P. *Journal of Molecular Structure* **2012**, *1023*, MOLECULAR VIBRATIONS AND STRUCTURES: THEORY AND EXPERIMENT, 101–107.
- (93) Ren, L.; Cheng, L.; Feng, Y.; Wang, X. *J Chem Phys* **2012**, *137*, 014309.
- (94) Ravaei, I.; Beheshtian, J. *Journal of the Korean Chemical Society* **2017**, DOI: <https://doi.org/10.5012/jkcs.2017.61.6.311>.
- (95) Boldyrev, A.; Shamovskii, I.; Schleyer, P. v. R. *Journal of the American Chemical Society* **1992**, *114*, 6469–6475.

- (96) Jiang, W.; DeYonker, N. J.; Wilson, A. K. *Journal of Chemical Theory and Computation* **2012**, *8*, PMID: 26596596, 460–468.
- (97) Bode, B. M.; Gordon, M. S. *Journal of Molecular Graphics and Modelling* **1998**, *16*, 133–138.
- (98) Turney, J. M. et al. *WIREs Computational Molecular Science* **2012**, *2*, 556–565.
- (99) Oberkofler, M.; Linsmeier, C. *Nuclear fusion* **2010**, *50*, 125001.
- (100) Dittmar, T.; Baldwin, M.; Doerner, R.; Nishijima, D.; Oberkofler, M.; Schwarzslinger, T.; Tabarés, F. *Physica Scripta* **2011**, *2011*, 014009.
- (101) Soto, G.; Díaz, J.; Machorro, R.; Reyes-Serrato, A.; de la Cruz, W. *Materials Letters* **2002**, *52*, 29–33.
- (102) Manzoor, S.; Tariq, Q.-n.; Yin, X.; Zhang, J.-G. *Defence Technology* **2021**, *17*, 1995–2010.